Summer 2012

Geomechanical characterization of reservoir & cap rocks for CO_2 sequestration

Sudarshan Govindarajan

Department:

GEOMECHANICAL CHARACTERIZATION OF RESERVOIR & CAP ROCKS FOR CO_2 SEQUESTRATION

by

SUDARSHAN GOVINDARAJAN

A THESIS

Presented to the Faculty of the Graduate School of the

MISSOURI UNIVERSITY OF SCIENCE AND TECHNOLOGY

In Partial Fulfillment of the Requirements for the Degree

MASTER OF SCIENCE IN PETROLEUM ENGINEERING

2012

Approved by
Runar Nygaard, Advisor
Ralph Flori
Andreas Eckert

ABSTRACT

Geological sequestration of CO_2 has been identified as one method to reduce global emissions of CO_2 and achieve lower levels of CO_2 concentrations in the atmosphere. Geological formations have to be assessed in terms of their capacity, sealing capabilities and economic feasibility before CO_2 sequestration can commence. Potential leakage of injected CO_2 from the reservoir formation could occur due to natural or injection induced faults or fractures in the reservoir or sealing formations. As part of a potential leakage investigation a geomechanical characterization which refers to the assessment of the *in-situ* stress conditions, rock strength and stiffness properties of the formations of interest helps to determine the seal integrity before, during and after injection of CO_2 into the formation.

In this study a rock mechanical testing apparatus was designed and commissioned, and the geological formations of interest were analyzed by conducting rock mechanical testing including Brazilian tensile tests, uniaxial tests and single stage triaxial tests accompanied by sonic velocity tests. Mohr Coulomb and Hoek Brown criteria were used to determine failure characteristics. The study helps establish the safe injection pressure. It was found that the formations had a greater likelihood of undergoing tensile failure than shear failure. Although laboratory tests revealed that the capping rock has a higher tensile strength than the reservoir rock, the combination of in-situ stress and pore pressure conditions makes the cap rock susceptible to failure very close to the tensile failure value of the reservoir rock and hence the injection pressures have to be maintained just below that of the tensile failure value of the reservoir rock.

ACKNOWLEDGMENTS

I would like to thank my advisor Dr. Runar Nygaard for accepting me as a graduate research student and for being a supportive and encouraging mentor guiding me through the difficult terrain of graduate research. I am also thankful to him for creating a friendly, challenging and collaborative work environment in B21and the drilling lab and for paying extra attention to the work-life balance of his students and their well being. I would also like to acknowledge the help of and express my gratitude to the U.S. Department of Energy whose grant DE-FE0001132 helped make this project happen.

I would like to thank Dr. Eckert and Dr. Bai for their guidance throughout the CO_2 sequestration project and for their patience in sitting through our weekly presentations. Special thanks goes to Dr. Flori who helped me out when I first joined the department and again when I was feeling stuck during the course of the research. A very special thank you to Mr Brian Swift, research engineer with the Civil Department for troubleshooting and guidance.

I would like to thank the student members of the CO_2 sequestration project especially Aaron Blue and Imowo Akpan. I would also like to express my gratitude to the B21 Brigade especially Steve Hilgedick who was an immense support and the back up cavalry and Mr. Fix-It throughout the project. I would also like to thank Saeed Salehi and Pratik Maheshwari who got me started off on the project, Pratik also was an immense help teaching me the basics of Labview and troubleshooting at all times of the day. I would also like to thank Ishan Kumar for helping me with the hands on field work. Cutting and hauling big boulders was fun.. thanks to Ishan. I would also like to thank Max Liberman for taking time to procure the desired hardware and getting me in touch with key people. A very special thanks goes to Paula Cochran who was my first boss and the mystic repository of the rules and regulations of the university.

Special thanks also go to my roommates who have been a great support system throughout the course of my graduate studies. Kunal, Roba, Himanshu, Sagar ... Thank you!

Finally a very big Thank You to the family back home because of whom all the efforts feel worthwhile!

TABLE OF CONTENTS

LIST OF ILLUSTRATIONS

LIST OF TABLES

1. INTRODUCTION

1.1. OVERVIEW AND MOTIVATION

The dependence of the world on fossil fuels as the main source of primary energy is leading to an increase in the levels of Green House Gases (GHG's) especially CO_2. The contribution of individual sources of fuel to fuel demand in 2004 is summarized in Table 1-1. It can be seen from Table 1-1 that the percentage contribution of fossil fuels i.e. oil, natural gas and coal to satisfy the energy needs of the world in 2004 comes to around 79%. The global energy demand has been predicted to increase by over 45% by 2030 as illustrated by Figure 1.1. Due to the efficiency, performance and availability of fossil fuels, even in 2030, it is expected that around 80% of the worlds fuel demand will continue to be satisfied by fossil fuels.

Table 1-1 Percentage contributions by fuel sources to world fuel demand (Steeneveldt et al., 2008)

Fuel Source	Percentage contribution
Coal	24
Natural Gas	21
Oil	34
Nuclear	5
Large Hydropower	6
Renewable	10

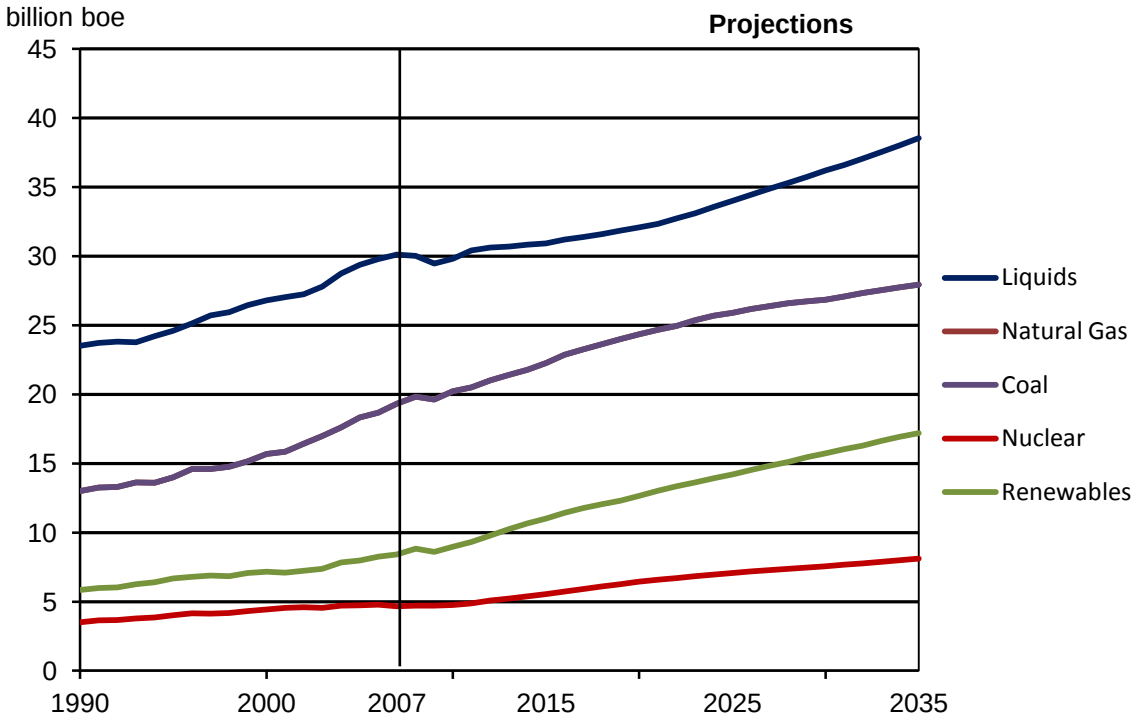

Figure 1.1Predicted Word Energy Demand by fuel type (Modified after USDOE, 2010)

CO_2 emissions are believed to cause climate change (Solomon et al., 2009), (IPCC 2007). Therefore the energy industry and the various regulatory authorities are searching for ways to reduce CO_2 emissions. The electricity generating industry and other industries which are stationary sources contribute to about 57% of the total emission of CO_2; transportation contributes to around 33% of the emissions (Folger, 2009). Given these numbers, the amount of reduction in emissions required for making a difference at a global level can be attained most likely by combining different approaches. CO_2 capture and storage (CCS) in geological formations can make a significant contribution to the reduction in emissions as shown in Table 1-2 . It can be seen from the table that 45% of

the emissions over the next 30 years can be sequestered even considering depleted oil and gas reservoirs alone, thereby reducing the overall emissions by a great amount.

According to the Interstate Oil & Gas Compact Commission (IOGCC) the geologic storage of CO_2 is among the most immediate and viable strategies for mitigating the release of CO_2 into the atmosphere (Flannery et al., 2008). This is because the concept of CO_2 injection into the subsurface is not new but has been continued to be carried out in the oil and gas industry as part of the enhanced oil recovery process (EOR) for over 30 years. After secondary recovery operations involving water flooding, supercritical CO_2 is injected to extract the remaining oil as an EOR process. This is possible because CO_2 dissolves into the oil, reducing its viscosity as well as causing it to swell. During this process some CO_2 remains behind which are about 30% of the original oil in place (Bradshaw et al., 2003). Thus the oil and gas industry already has some experience with the injection and storage of CO_2 as a process. However it has to be noted that the primary purpose of EOR had always been enhanced production and not geological storage of CO_2. There is a requirement for testing the application of the EOR technology specifically for the purpose of carbon sequestration and the United States Deparment of Energy (D.O.E.) has started a number of projects covering the whole of the country and targeting 97% of the emissions from both coal fired electricity plants as well as other industries (Litynski et al., 2009), (USDOE, 2012).

Table 1-2 Estimates of storage capacities for different geological reservoirs (Gale, 2004)

Storage Option	Global Capacity	
	Giga tonne CO_2	% of emissions to 2050
Depleted Oil & Gas fields	920	45
Deep Saline Reservoirs	400-10000	20-500
Un-mineable Coal Seams	20	<2

1.2. THESIS OBJECTIVE

The Lamotte sandstone deposited in the subsurface in Missouri is identified as one potential sequestration reservoir (Boongird et al., 2006). One of the phenomena associated with injection of fluids into reservoirs is the change induced in the pore pressure as well as changes in in-situ stresses. Injection of fluids causes an increase in pore pressure causing a decrease in in-situ stresses. The reduced stresses could lead to creation of unwanted hydraulic fractures as well as breach of the seal integrity (Terzhagi, 1943), (Khan et al., 2010). Ensuring the long term containment of injected CO_2 is one of the critical challenges to be faced for increasing the global acceptance of CCS. A geomechanical assessment can be used to determine the potential leakage paths by identifying the relevant parameters such as in-situ stress regime, rock stiffness and strength parameters. The geomechanical assessment consists of creating a model called as a mechanical Earth model which replicates the rock strength and states of stress and helps in characterizing operation risks associated with geomechanics. Rock mechanical testing is utilized as a characterizing tool to provide the rock strength and elastic properties data to the mechanical earth model.

The rock mechanical characterization is usually done on the basis of Brazilian tensile testing, uniaxial testing and single/multi stage triaxial testing. Rocks are much weaker under tension as compared to when under compression or shear and hence tensile failure is an important design criterion in rock mechanics. The Brazilian test is used to determine the tensile strength of the rock. The study of the behavior of rocks under compression can be done using uniaxial or triaxial tests, however triaxial test results are considered more accurate. Triaxial tests give the rock strength and deformation properties.

The objective of this thesis is the geomechanical characterization of a potential CO_2 sequestration site in Missouri to aid in the identification of potential fracture prone zones using Brazilian and triaxial tests. The thesis consists of 6 chapters and 5 appendices. Chapter 1 is the introduction, chapter 2 covers the literature review and basic theory, chapter 3 deals with site geology and sampling procedures, chapter 4 discusses the laboratory setup and procedures, chapter 5 gives the results, followed by analysis and

discussion, chapter 6 provides the summary and concluding remarks. There are 5 appendices; Appendix A gives the sample characteristic details for each of the test, B gives the test summaries of the Brazilian, the uniaxial and the triaxial tests, Appendix C shows the stress-strain plots obtained from the triaxial testing, Appendix D shows the calculation for pore pressure causing tensile failure in formations and Appendix E shows the photographs taken before and after testing.

2. LITERATURE REVIEW

2.1. OVERVIEW OF CO2 CAPTURE & SEQUESTRATION

The aim of CO_2 Capture and Sequestration (known as CCS) is to contribute towards global reduction in CO_2 emissions by "capturing" produced CO_2 which would otherwise be released to the atmosphere and storing it within geologic formations. CO_2 sequestration has been a subject of interest since the 1990's and became main stream after the UNFCCC (United Nations Framework Convention on Climate Change) announced its goal of achieving stabilization in anthropogenic greenhouse gas emissions (UNFCC, 2012). There has been an increased global acceptance of the need to contain emissions and the Kyoto protocol was one of the results of this increased acceptance. The Kyoto Protocol is an agreement which the major industrialized nations have signed and is linked to the United Nations Framework Convention on Climate Change (UNFCC, 2012). The agreement binds around 37 industrialized nations and the European community to reduce their emissions by an average of 5% below their 1990 emission levels over the five year period from 2008 to 2012. The required deep reductions in the emissions can be met only by simultaneously pursuing different paths to mitigate CO_2 emission such as fuel switching, energy efficiency, renewable energy and CO_2 capture and sequestration. Fuel switching and energy efficiency take care of the reduction in the production of CO_2 at the source, but there is a limit to the changes that can be accommodated by both private and public establishments without incurring some financial burden. Even with these changes there usually is some production of CO_2. This produced CO_2 is to be captured and sequestered, thus reducing emission both at the source and after production.

2.2. CO_2 CAPTURE & SEQUESTRATION PROCESS DESCRIPTION

The process involves three main steps: 1) CO_2 capture and separation 2) Compression and transportation of CO_2 to site 3) Sequestration in geological formations.

2.2.1. CO_2 Capture & Separation. The initiation of the CCS process occurs when CO_2 is captured and reproduced in a concentrated form for convenience in transportation and storage. The different approaches for capture of CO_2 under consideration are: (1) Post-Combustion Capture (2) Pre-combustion Capture (3) Oxy-fuel Combustion Capture. The technologies available at present give a theoretical efficiency of 90% i.e. remove 90% of the emissions from the effluent stream (considering the case of power plants), but have not yet been applied at the level of a full scale power plant. There are plans to have such a commercial level electricity generating plant of 300MW capacity with carbon capture facilities operational by 2014 in the UK. (ACCAT, 2009). Two examples of successful pilot plants are the Ferrybridge carbon capture pilot which utilizes post combustion capture with an efficiency of 90% and the Renfrew oxyfuel project with efficiency between 75-85% (DECC, 2012).

When the CO_2 is extracted from the flue gas emitted due to combustion of fuels, it is called as post-combustion capture. Chemical process industries use processes which could be modified towards use in the carbon capture industry for stripping the effluent stream of CO_2. At present most electricity generating plants do not make the efforts towards using this method as there is no economic incentive to do so. However this method is readily applicable even considering the technology available at present (Folger, 2009). Pre-combustion capture involves the separation of CO_2 before the combustion occurs into streams of hydrogen and CO_2, by reacting the fuel with air or steam to produce hydrogen; used for combustion and CO_2 which is sent for sequestration. Steam reforming is the most commonly used technique to achieve the separation. In the absence of a requirement or economic incentives, pre-combustion technologies have not been used for some power systems, such as natural gas combined-cycle power plants (Folger, 2009). The oxy-fuel combustion process is similar to the pre-combustion CO_2 capture in principle, except that instead of using air or steam the fuel is reacted with pure oxygen to get separate streams of CO_2 and the other produces the fuel to be eventually used. The stream containing CO_2 will essentially contain CO_2 and water which are easier to separate. This technique is still under research as the temperatures required for a pure oxygen combustion process to occur are very high (around 3500°C). Theoretically the flue gas after stripping of the additional pollutants such as SO_2 and NOx, can be recycled

back to the reaction unit to reduce the temperature of the reaction. Depending on site specific conditions, oxy-fuel could be retrofitted onto existing boilers (Folger, 2009).

2.2.2. Compression & Transportation. The CO_2 capture process would be feasible only when the volume being captured and transported is large (Folger, 2009). Examples of large volume producing sources of CO_2 would include power stations and large industrial plants and in most cases these would not be located very near to reservoirs suitable for CO_2 storage thereby creating the need for the transportation of CO_2. However pipeline and shipping are a bulk volume transportation systems already being used in industries which can be adapted towards CO_2 transportation. It is to be noted that CO_2 behaves differently when subject to different temperature and pressure conditions; hence transport of CO_2 requires careful monitoring. Pipeline transport has been used for the transportation of CO_2 in the oil and gas industry for a considerable amount of time especially in the United States. The need of CO_2 in EOR processes was satisfied by transporting the CO_2 under pressure using pipelines. In the U.S alone there is around 3000km of pipelines transporting CO_2 (Folger, 2009). The CO_2 is transported by compressing it to a supercritical/denser phase which is maintained by having recompressing stations at regular intervals along whole the length of the pipeline. Transportation pressures are usually in excess of 10 MPa. The presence of water molecules is very dangerous as together with CO_2 it forms an acidic mix which corrodes the pipeline, water and CO_2 could also form CO_2 hydrate crystals which may cause blockage of the pipeline, thus making drying a necessary process in the transportation of CO_2 (Seevam et al., 2008). To develop a proper transport mechanism using ships, the present case of transportation of Liquefied Petroleum Gas (LPG), can serve as an analog. According to Aspelund et al., (2006), economical bulk transportation of CO_2 by ship could be done in semi-pressurized vessels at pressures near the triple point in order to take advantage of the existing designs of commercial LPG transportation units. Another factor to consider is the fact that since ship transportation does not ensure a continuous supply of CO_2, there has to be a temporary storage facility in which CO_2 could be kept for supply to the sequestration system.

2.2.3. CO_2 Phase Behavior. The transported CO_2 has to be compressed to be stored in a geological reservoir. Under natural conditions i.e. at atmospheric pressure and room temperature i.e. 101.325 KPa (14.7 psi) and 25˚C (77˚F) CO_2 exists as a gas with a density of 1.833kg/m^3 (0.1144 lb/ft^3). The behavior of CO_2 in different phases under different conditions of pressure and temperature is given by the phase diagram for CO_2 shown in Figure 2.1. The phase diagram shows the conditions at which CO_2 exists in the three phases as well as the equilibrium lines showing simultaneous existence in two phases. It is preferred to inject the CO_2 in a super critical phase i.e. at a temperature and pressure beyond the critical point as it increases in density, with the density ranging between 150 kg/m^3 to over 800 kg/m^3 and takes up less volume than if it were in a gaseous phase. Once injected underground the density and phase behavior of CO_2 depends on the temperature and pressure to which it is subjected. Kaldi and Gibson Poole (2008) studied the variation of the density of CO_2 density with depth and how it affects storage capacity. The study was done considering a thermal gradient of 30˚C/km. The results of that study have been summarized in Figure 2.2. As can be seen from the diagram, when stored as a supercritical fluid, CO_2 has a density approaching 800 Kg/m^3. The density increases rapidly with increase in depth and remains stable after a certain depth. The numbers next to the curve represent the volume occupied by 100 m^3 of CO_2 at surface conditions at the reference depth.

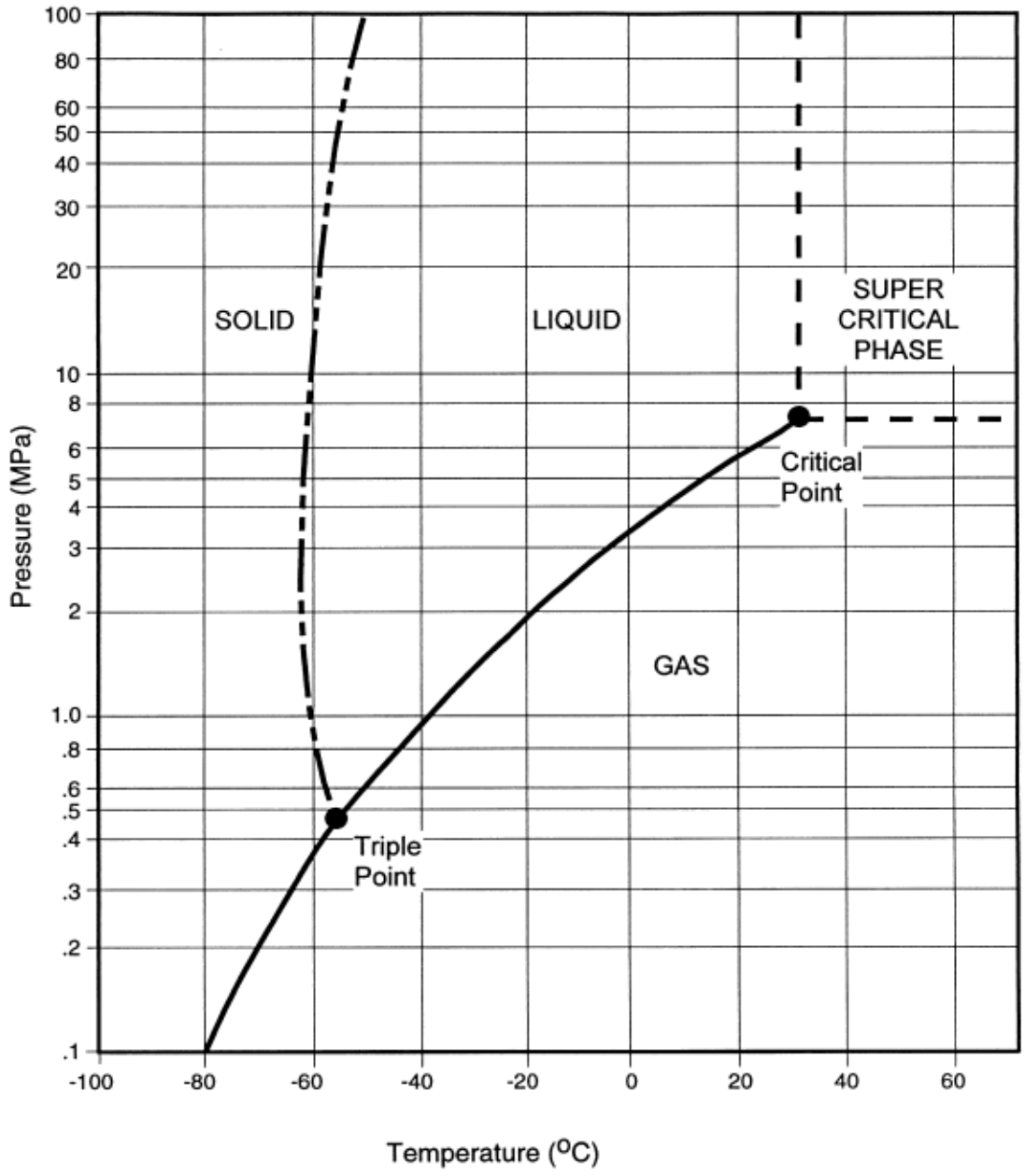

Figure 2.1 Phase diagram of CO_2 (Bachu, 2000)

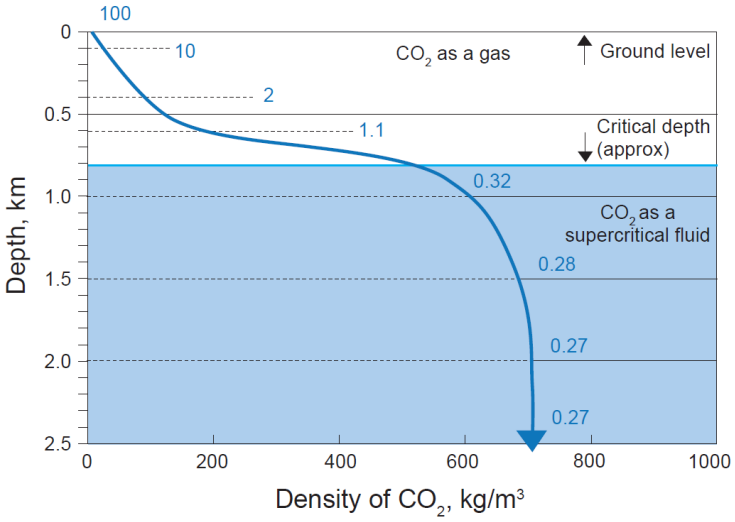

Figure 2.2 Increasing storage effectiveness for CO_2 with depth. Volumetric relationship shown next to curve. (Kaldi and Gibson-Poole, 2008)

2.2.4. Sequestration In Geological Formations. Three main sequestration techniques have been considered; sequestration in (1) depleted oil & gas reservoirs (2) deep saline reservoirs (3) un-mineable coal seams. The aim is to inject CO_2 at a supercritical state – a relatively dense fluid – into subsurface formations which hold or previously held fluids. The CO_2 is injected at depths greater than 800 m, as the pressure keeps the CO_2 in a denser state. Table 2-1 presents the overview of the different geological sequestration options, comparison has been done based on trapping mechanisms, pioneer projects, advantages and disadvantages and potential economic offset to undertaking CO_2 sequestration.

Table 2-1Geological sequestration overview

Type of Reservoir	Trap Mechanisms	Pioneer Project	Advantages	Dis-advantages	Economic Offset
Oil	Solubility: Oil	Weyburn	(i)Demonstrated Structural Integrity	(i) Existing wells could become conduits	EOR
	Physical Trapping		(ii)Geological characterization study already carried out	(ii) Danger of over pressurizing Cap Rock	
	Mineralization		(iii) Simulation Models applicable to individual reservoirs readily available	(iii) Shallow fields may not have enough pressure	
			(iv)Infrastructure and wells in place	(iv) Fields could be far away from sources	
Gas	Residual Gas Trapping	In Salah	*Same as oil*	*Same as oil*	Repressurize/ maintain pressure
	Physical Trapping				
	Mineralization				
Deep Saline	Solubility: water	Sleipner	More widespread	(i) lower and upper capacity estimates vary greatly	-
	Physical Trapping		Potentially larger capacity	(ii)increase in permeability due to acidifying	
	Mineralization				
Un mineable Coal Seam	Adsorption	-	Potential Permanent entrapment	(i)not all coal beds suitable for CBM	Coal Bed Methane

2.2.4.1. Depleted oil & gas reservoirs: The oil and gas industry already has experience in injection of CO_2 through its usage in the EOR operations wherein CO_2 mutually dissolves with the remaining recoverable oil. Dissolution of CO_2 into oil causes a reduction in the oil's viscosity as also causes an increase in oil volume called swelling of oil, increasing saturation and relative permeability. The CO_2 used to recover the oil is then captured and recycled for further recovery operations. Water Alternating Gas (WAG) process is used to sustain the recovery operation wherein the recovery using CO_2 is alternated with water flooding operations to maintain the reservoir pressure. This cycle may continue till required oil recovery is reached after which the CO_2 could be left in the reservoir under pressure. Many oil and gas fields offer the opportunity for integrated CO_2 enhanced oil recovery and CO_2 sequestration (Petrusak et al., 2009). CO_2 has the potential to act as the cushion gas for maintaining pressure, helping in hydrocarbon production or storage. The CO_2 could be then stored in the formation once all the hydrocarbon has been produced. Since the formation has managed to contain commercially exploitable levels of hydrocarbon, it is a proven resource for storage of CO_2 (Petrusak et al., 2009). In volumetric natural gas reservoirs only physical storage will take place, whereas if the reservoir pressure is being maintained by water influx dissolution into the water would be an additional storage mechanism (Gale, 2004).

2.2.4.2. Deep saline reservoirs: In deep saline reservoirs there are different trapping mechanisms at work with the major one being solubility trapping. Initial injection of the CO_2 causes it to enter the aquifer and rise up to the cap rock because of its buoyancy and form a thin layer under the cap rock. Over time, taking about thousands of years to reach process completion, the CO_2 gets dissolved into water and is permanently retained in the reservoir. Some mineralization trapping as well as physical trapping does occur in aquifers, but in limited amounts. Deep saline reservoirs seem to be the most promising depositories for CO_2 as they occur both offshore and onshore and in potentially large volumes available for CO_2 storage (Derakhshanfar et al., 2011).

2.2.4.3. Unmineable coal seams: With respect to coal seams CO_2 is injected either for enhancing coal bed methane production or simple CO_2 storage. In the case of Coal Bed Methane, lab experiments have shown that for every volume of CO_2 injected two volumes of CH_4 are produced. There are two trapping mechanisms at work in coal seams; adsorption onto the coal with displacement of CH_4 and actual physical trapping in the cleats within the coal. Once trapped, the CO_2 can be expected to remain in place for a long period of time unless the mine is used for production (Gale, 2004).

2.3. PIONEER DEMONSTRATION PROJECTS

Some of the notable pioneering projects include 1) Weyburn -EOR 2) In Salah – CO_2 storage in Natural Gas Reservoir 3) Sleipner-Deep Saline Aquifer. These have been discussed further below:

2.3.1. The Weyburn Project: It is a pioneering enhanced oil recovery project in South Central Canada with some emphasis on the geological storage of the CO_2 used in the EOR process. The CO_2 itself is captured from a coal gasification plant located in North Dakota. Around 5000 tons of CO_2 is injected everyday and approximately 20 million tonnes CO_2 is expected to remain in the formation over the lifetime of the project (Folger, 2009). There were reports of CO_2 leaking from the site which were refuted in the official report by the Petroleum Technology Research Centre (PTRC). The initial report of leakage occurrence was made by Petro-Find Geochem ltd which claimed that the injected CO_2 was leaking through the formation. The report by PTRC refuted the findings stating that the observed phenomena could be explained by near surface processes including microbial generation of soil CO_2 and methane (PTRC, 2011).

2.3.2.The In Salah Project: It is a pioneering work in Algeria towards storing CO_2 in a natural gas reservoir and is the world's largest effort towards this end at present. The CO_2 is separated from the natural gas which is produced from the formation and then re-injected into the reservoir. The amount of CO_2 which will be deposited in the

formation over the lifetime of the project is expected to be over 17 million tonnes (Folger, 2009).

A paper by Mathieson et al., (2010) summarizes the lessons learned from the project and the innovative techniques use to solve CO_2 monitoring issues. One of the more innovative techniques involves using satellite technology to detect tiny ground movements at the mm scale to monitor the CO_2 plume movement. A very important lesson learnt was to completely decommission legacy wells as around 1 tonne of CO_2 was leaked through such a well before detection and subsequent decommissioning of the well. It was also observed that the cost effective technologies such as well head monitoring and annulus monitoring were very useful. The final observation of the paper was that rock mechanical data and fractured rock characterization was more important than what was initially anticipated and that the current efforts were being focused on the acquisition of geomechanical data from cores of the overburden and through the logs. An overall storage of 3 million tonnes of CO_2 has been successfully achieved until 2010.

2.3.3. The Sleipner Project: This was the first geological sequestration operation carried out and it has been very successful. The required CO_2 is captured from the natural gas produced at the nearby Sleipner West Gas Field, is compressed and stored in the Utsira formation. The Utsira formation is a sandstone reservoir at a depth of 800 ms below the sea bed of the North sea containing saline fluids. It is one of the oldest sequestration operations, being started in 1996 and storing about 1 Mt CO_2 per year. Continuous monitoring of the project has not revealed any discrepancies such as leakages and simulation results have predicted that the CO_2 might dissolve in the water gradually (Folger, 2009). The monitoring has involved 3-D and 4-D seismic, sonar and videos using ROV (remotely operated vehicle). Calculations show that CO_2 is being absorbed into formation water at a rate of 1.8% per year. Also since the injection capacity and reservoir storage capacity are plentiful there has not been a need for reservoir management (Eiken et al., 2011).

2.4. CO_2 TRAPPING MECHANISMS IN GEOLOGICAL SEQUESTRATION

The geologically sequestered CO_2 can be subject to a number of trapping mechanisms depending on the nature of the formation in which it has been stored. The commonly active mechanisms in both depleted oil and gas reservoirs as well as aquifers are physical trapping, mineralization, phase trapping. Other mechanisms include dissolution into formation water or oil and adsorption onto the surface of coal seams.

2.4.1. Physical Trapping: This refers to trapping of CO_2 or containment within structural and stratigraphic traps. This is mainly applicable to immiscible or free phase CO_2 which rises up due to buoyancy. The effectiveness of these traps as containment units has been proved by their ability to contain oil and gas over thousands of years. Structural traps are traps created due to folding or faulting whereas stratigraphic traps are created due to variation in the lithology of the reservoir rock, termination of reservoir or other interruption of continuity. Figure 2.3 shows the examples of structural and stratigraphic traps. The parameters of interest are the minimum capillary pressure to be exceeded and the critical height of gas/oil over which the fluid will start to migrate (Berg, 1975). Equations 1 and 2 show the expressions for the minimum capillary pressure and the critical height of fluid column at hydrostatic conditions:

$$P_c = \frac{16.3 \cdot T}{\mathrm{D}} \tag{1}$$

Where P_C is capillary pressure (dynes/cm$^{2)}$, T is interfacial tension (dynes/cm), D is mean rock grain diameter (mm). Equation 2 represents the critical height calculation to be used when hydrostatic conditions are applicable, under hydrodynamic conditions Equation 3 is to be utilized.

$$Z_c = \frac{\left[2 \cdot T \cdot \left(\frac{1}{r_t} - \frac{1}{r_p}\right)\right]}{\left[g \cdot (\rho_w - \rho_o)\right]} \tag{2}$$

Where Z_C is critical fluid height over which migration occurs (mm), T is interfacial tension (dynes/cm), r_t is pore throat radius (mm), r_p is pore radius (mm), g is acceleration due to gravity(cm/s^2), ρ_w/ρ_o is density of water/ oil respectively (g/cc).

$$Z_c = \frac{\left[2 \cdot T \cdot \left(\frac{1}{r_t} - \frac{1}{r_p}\right)\right]}{\left[g \cdot (\rho_w - \rho_o)\right]} \pm \left[\frac{\rho_w}{\rho_w - \rho_o}\right] \frac{dh}{dx} x_o \qquad (3)$$

Where x_o is horizontal width of hydrocarbon stringer and h is hydrostatic head. The sign of the term accounting for the hydrodynamic regime is decided by the direction of flow of water.

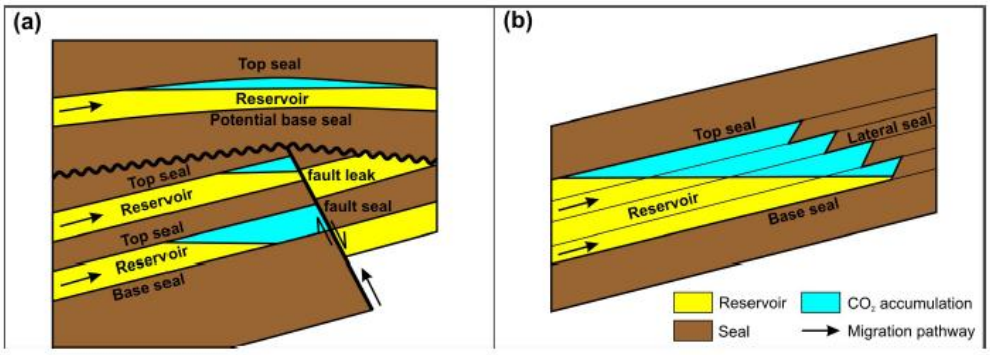

Figure 2.3 Examples of (a) structural and (b) stratigraphic physical traps for CO_2 (Kaldi and Gibson-Poole, 2008)

2.4.2. Mineralization: This depends completely on the mineral content of the formation. In this trapping mechanism the CO_2 reacts with the minerals to form compounds such as carbonates and alumino silicates. The reaction rates wary from a few days to thousands of years depending on the combination of active species involved in

the reaction. This mechanism is considered the most permanent of the trapping mechanisms due to the CO_2 being rendered immobile.

2.4.3. Hydrodynamic Trapping: When CO_2 is injected into the formation it splits into two phases: free CO_2 and CO_2 rich brine. CO_2 rich brine refers to the trapping of CO_2 by dissolution into the slow moving formation waters rendering the CO_2 trapped for millions of years. If the free phase CO_2 is stored in horizontal or gently dipping reservoirs it gets trapped for a duration ranging from thousands to millions of years since flow of free phase CO_2 is a function of dip of sealing horizon, flow velocity and direction of in-situ formation water flow. "Hydrodynamic trapping can be considered a "rate seal" as opposed to a traditional "rock seal" associated with structural and stratigraphic traps" (Kaldi and Gibson-Poole, 2008). The rate at which CO_2 is injected has an effect on the displacement of saline formation water and hence on CO_2 storage in the formation (Holt et al., 1995).When the injection rate is high, viscous forces play the dominant role and the CO_2 plume moves rapidly through the most permeable path. When injection rate is low, then the effect of gravity is more pronounced and the CO_2 rises upwards because of buoyancy. The greater the length of the migratory pathway, more is the chance of the free phase CO_2 getting trapped residually or in solution.

2.4.4. Dissolution: CO_2 has been found to dissolve in water as well as oil. This is the main storage mechanism in aquifers in which physical trapping is not possible and one of the storage mechanisms in storage of CO_2 in abandoned oil reservoirs. Solubility of CO_2 is a function of temperature and pressure and water salinity. An increase in pressure increases solubility of CO_2 in water, increase in temperature causes a decrease in solubility. At room temperature solubility of CO_2 in water is 90 cm^3 per 100 ml of water. As per Carroll and Mather (1992), up to a temperature of 100˚C or 212˚F, the solubility of CO_2 in water can be reasonably calculated using the correlation given below:

$$e^{\left[\frac{A(x^2{}_1-1)}{RT}\right]} \cdot H_{21} \cdot x_2 \cdot e^{\left[\frac{v_2(P-P_1{}^0)}{RT}\right]} = \mathrm{y}_2 \cdot P \cdot \phi_2 \qquad (4)$$

Where *A* is Margules constant, *x* mole fraction in liquid, *y* mole fraction in vapor, *T* is absolute temperature, *R* gas constant, *P* is total pressure, P^0 is vapor pressure, *v* is partial molar volume at infinite dilution, H_{21} is Henry's constant for solute 2 in solvent 1.The reactions involved in the dissolution of CO_2 into water are complex and multilayered (Vorholz, 2000). First CO_2 changes from gaseous phase to aqueous phase.

$$CO_2\,(g) \Longleftrightarrow CO_2\,(l)$$

Next the liquid phase CO_2 reacts with water to establish equilibrium with carbonic acid (H_2CO_3).

$$CO_2\,(l) + H_2O\,(l) \Longleftrightarrow H_2CO_3\,(l)$$

The above reaction is kinetically slow and only a small fraction of the dissolved CO_2 is converted into carbonic acid. Carbonic acid is a weak acid and dissociates further.

$$H_2CO_3 + H_20 \Longleftrightarrow H_30^+ + HCO_3^-$$

$$HCO_3^- + H_2O \Longleftrightarrow H_30^+ + CO_3^{2-}$$

The carbonate anions thus formed have the potential to react with the cations present in water to form insoluble carbonates with calcium ($CaCO_3$) and magnesium ($MgCO_3$) carbonates being the most prominent examples. The formation of these precipitates pulls the equilibrium more towards the right facilitating greater dissolution and resulting in the acidification of the water (Lide, 1991).

2.4.5.Residual Trapping: The CO_2 from the tail end of the migrating CO_2 plume gets trapped by capillary forces and ceases to flow when the CO_2 concentration falls below a certain level. Thus a trail of residual and immobile CO_2 is left behind over the course of the migration of the CO_2 plume (Juanes et al., 2006). Overtime the residual CO_2 dissolves into the formation water (Ennis-King and Patterson 2000). Figure 2.4 shows the residual trapping process.

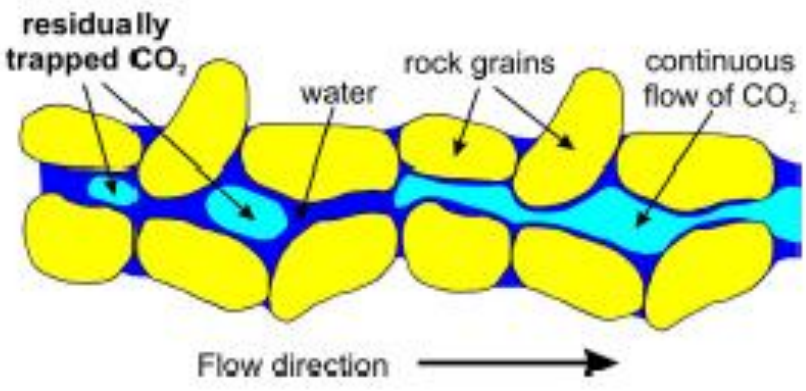

Figure 2.4 Residual Trapping of CO_2 (Kaldi and Gibson-Poole, 2008)

2.4.6. Adsorption: This mechanism is mainly applicable only to storage of CO_2 in coal seams. Adsorption is a surface phenomenon in which the particles of a material (adsorbate: CO_2) gets adhered onto the surface of another (adsorbent: coal). The process could be purely physical or have chemical reaction aspects also (Ripepi, 2009)

2.5. GEOLOGICAL FAILURE MECHANISMS & RISK ANALYSIS FOR SITE SELECTION

The main risk to geological storage of CO_2 is leakage through the containing formation. The geological entities which could lead to release or leakage of CO_2 from storage site to surface are faulty seals and reactivation of faults & fractures. Other factors which could be responsible for potential leakage scenarios are improperly abandoned wells and cement degradation. The emphasis has to be on the factors which induce changes causing an introduction or enhancement of leakage pathways in existing reservoirs. All these factors are to be accounted for along with any other possibilities to formulate a risk analysis for potential sequestration sites as the factors could contribute together to create a complex leakage scenario.

1) Faulty Seals: It has been found from experience in the natural gas industry that inadequate characterization of the seal has been an important parameter in any

containment failure scenario (Espie, 2005). Evaluating the sealing cap rock is even more important in the case of aquifers as usually they are studied in lesser detail. When CO_2 is injected, because of its buoyancy, it will rise up against the cap rock and exert an up thrust. The accumulation of CO_2 and the increase in the up thrust can allow the CO_2 to exceed the critical capillary pressure and leak across the seal. There is also the possibility of chemical reactions strengthening or weakening the cap rock. Thus the study of the nature of the cap rock plays an important role in the assessment of the suitability of a formation for geological sequestration.

2) Faults & Fractures: Injection of fluid into formations causes a change in the state of stress and faults which are close to a critical stress state have a higher tendency to move in response to those changes. They may pose a risk to the integrity of the seal and hence should be monitored.

2.5.1. Fault Reactivation. This is one of the important scenarios which could result in CO_2 leakage. When the maximum shear stress exceeds the shear strength of the fault zone it induces slip on the fault creating a potential leakage path. As such it would be useful to be able to determine the risk of slip on a fault. Hawkes et al have defined a parameter called as modified slip tendency given by Equation 5 (Hawkes et al., 2004):

$$\tau_{sm} = \frac{\tau}{\tau_{slip}} \tag{5}$$

Where τ is the maximum shear strength (MPa), τ_{slip} is slip strength (MPa), τ_{sm} is the modified slip tendency which is unit less. Based on the above definition, fault reactivation is predicted when $\tau_{sm} \geq 1$. For cohesion- less fault it is defined as:

$$\tau_{sm} = \frac{(\sigma_1 - \sigma_2)\cdot \sin 2\delta}{\left[(\sigma_1 + \sigma_2) + (\sigma_1 - \sigma_2)\cos 2\delta - 2p\right]\cdot \tan \phi_{fault}} \tag{6}$$

In the above Equation σ_1, σ_3 are the maximum and minimum principal stresses, p is pore pressure in the fault plane, δ is the angle between the fault plane and σ_3, and $\emptyset_{fault}$ is the fault friction angle. Thus factors which influence the fault slip risk are the in-situ

stress magnitudes, pore pressures in fault planes, orientation of fault plane and fault friction angle. The above Equation is based on 2d stress transformations and uses the Mohr Coulomb shear failure criterion. It is a well known fact that the fault striking almost parallel to the intermediate in-situ stress is the one which has the highest tendency to slip. There are a number of mechanisms which have the potential to cause reactivation of the fault, some of the scenarios were discussed by Hawk et al. (2004), and mitigation measures were suggested. The mechanisms which were suggested include:

- Faults within or bounding the reservoir
- Pressure change in the fault plane.
- Faults within or bounding the reservoir – pervasive pressure change
- Faults in the overburden
- Induced shear failure
- Hydraulic fracturing
- Borehole instability
- Casing deformation and failure

In order to tackle pressure changes in the fault plane it was suggested to conduct geomechanical analysis to decide maximum injection pressures and placing injection wells as far as possible from the faults helps mitigate this scenario. For pervasive pressure change scenario the interpretation of Equation (5) shows that the parameters important for the analysis of this scenario are the present day in-situ stress regime, orientation and strength properties of the faults that cut or bound the reservoir, reservoir depletion response, minimum pressure experienced during depletion and maximum pressure expected during injection.

The analysis of faults in the overburden mainly deals with reactivation of faults due to the downward displacement of overburden with change in pore pressure of reservoir. This risk mechanism is more associated with depletion scenarios rather than injection yet it could result in casing deformation, well failures, loss of secondary seal capability and leakage in near reservoir areas. Mitigation measures include choosing greater reservoir depths and monitoring minimum reservoir pressure to keep it above critical levels.

In induced shear failure scenario the cap rock over any reservoir experiences significant shear stresses due to the expansion and contraction of the reservoir caused by the temperature and pressure changes accompanying production/injection of fluid. This scenario could result in creation of new fractures in the cap rock. The parameters important in this risk mechanism are

- High reservoir compressibility
- Stiff caprock
- Large pressure changes
- Low strength caprocks
- Shallow depths
- Domed or anticlinal reservoirs

The increase or decrease in pore pressure increases the tendency of this scenario. Mitigation measures should include accounting for the effects of the minimum and maximum pore pressure which the reservoir might experience during production/injection.

Hydraulic fractures are induced by injecting low temperature fluids at high injection pressures. The undesired growth of the fractures from the reservoir into the caprock could lead to leakage scenarios. Mitigation measures include injection below critical pressures, preferential selection of high permeability reservoirs, and usage of horizontal injection wells.

The stability of the borehole is dependent on the ability of the formation rock to withstand the concentrated stress induced around it due to the operations of drilling, completion and finally production. If the induced stresses are greater than the rock strength it could result in breakouts or fracturing of the borehole wall. The danger of CO_2 leakage becomes greater when there is poor cement emplacement leading to potential leakage pathways. The parameters important to borehole instability include:

- In-situ stresses
- Rock strength
- Formation pressure
- Near well pore pressure change

The failure of the casing could be the result of any of the above discussed scenarios such as reservoir compaction and induced shear failure. If mitigation measures are in place against the above mentioned parameters then it will reduce the chances of casing deformation due to these parameters.

Wiprut and Zoback (2002) also showed that stress, pore pressure and fault orientation together influence hydrocarbon leakage and migration. It was shown by them that critically stressed faults on the verge of slipping tend to leak. Faults which are more stable act as seals. They concluded that fault reactivation and hydrocarbon leakage are caused by three factors:

- Locally elevated pore pressure due to buoyant hydrocarbons abutting faults
- Faults oriented optimally for frictional slip under existing in-situ conditions
- Recent perturbation of compressional stress associated with post glacial rebound

The combination of the above three factors could result in a previously sealing fault to start leaking.

2.6. ROCK MECHANICS: INTRODUCTION AND RELEVANCE

The injection of CO_2 into the subsurface formation will cause changes in the state of stress of the formation. Existing fractures as well as newly created ones can form leakage pathways for the stored CO_2. In order to be able to predict and anticipate the response of the formations to the injection activity it is necessary to test the formation rock under laboratory conditions. If the deformation of rock assumed to be linear elastic it can be described by the Poisson's ratio (ν), Youngs modulus (E) and Bulk modulus (K). The elastic and bulk moduli are measured in Pascals where as Poisson's ratio dosen't have any units. The Poisson's ratio (ν) is defined as the ratio of the radial or transverse strain to the longitudinal or axial strain experienced by the rock. It is expressed as

$$\nu = \varepsilon_{transverse} \Big/ \varepsilon_{longitudinal} \tag{7}$$

Young's modulus (E) is defined as the stiffness of the rock i.e. the resistance to axial deformation.

$$\sigma = \varepsilon \mathrm{E} \tag{8}$$

where σ is the axial stress, ε is axial strain and E is the Young's modulus. Bulk modulus (K) is the resistance to change in volume due to loading. It is also called as modulus of compression and is measure of the incompressibility of the rock. It is expressed as:

$$K = \sigma / \Delta v / v \tag{9}$$

Where K is the bulk modulus, σ is the stress, v is volume and Δv is the change in volume. Shear Modulus (μ) is a measure of the resistance to shear deformation, also called as modulus of rigidity. It is defined as the ratio of the shear stress (σ_{shear}) to the shear strain (ε_{shear}) when a shear force is applied to the object.

$$\mu = \frac{\sigma_{shear}}{\varepsilon_{shear}} \tag{10}$$

2.7. STRESS

The traction vector acting on an area is defined as the ratio of the force acting on the area over the area being acted upon. In order to define the traction over a point the area is allowed to reduce to zero and thus the mathematical expression for a traction vector is given by (Jaeger et al., 2008):

$$\lim_{(dA \to 0)} \frac{dF}{dA} \tag{11}$$

The state of stress at a point is defined by all the traction vectors associated with all the planes that pass through the point. The traction generally varies with the orientation of the surface on which it acts and is most conveniently represented with the aid of an entity known as the stress tensor. The stress tensor is found by using coordinate transformation on the traction vectors corresponding to three mutually perpendicular planes. This relation is known as Cauchy's second law.

$$T_i = \sigma_{ij} \cdot n_j \tag{12}$$

Where σ_{ij} is the stress tensor which is expressed as follows:

$$\sigma_{ij} = \begin{bmatrix} \sigma_{xx} & \sigma_{xy} & \sigma_{xz} \\ \sigma_{yx} & \sigma_{yy} & \sigma_{yz} \\ \sigma_{zx} & \sigma_{zy} & \sigma_{zz} \end{bmatrix} \tag{13}$$

If the stress tensor at a particular point is known the traction for all surfaces passing through that point can be found out. Stress at a point can be resolved into a normal stress and a shear stress. The shear stresses for a stress field could vanish for a particular coordinate system, and the stress field would be defined completely by only the three normal stresses. These normal stresses which alone completely describe the stress field are called as principal stresses and are always mutually perpendicular though different in magnitude. For a stress field having just the principal stresses the stress tensor would be expressed as follows:

$$\sigma_{ij} = \begin{bmatrix} \sigma_{xx} & 0 & 0 \\ 0 & \sigma_{yy} & 0 \\ 0 & 0 & \sigma_{zz} \end{bmatrix} \tag{14}$$

Some conventions express the principal stresses as σ_1, σ_2, and σ_3 or S_1, S_2, S_3 wherein 1 is the maximum stress and 3 is the minimum stress. Some of the stress derivatives are given below:

Differential Stress:

$$\sigma_d = \sigma_1 - \sigma_3 \tag{15}$$

Mean Stress:

$$\sigma_m = (\sigma_1 + \sigma_2 + \sigma_3)/3 \tag{16}$$

Deviatoric Stress:

$$\sigma_{ij} = \begin{bmatrix} \sigma_{xx} - \sigma_m & \tau_{xy} & \tau_{xz} \\ \tau_{xy} & \sigma_{yy} - \sigma_m & \tau_{yz} \\ \tau_{xz} & \tau_{yz} & \sigma_{zz} - \sigma_m \end{bmatrix} \tag{17}$$

In order to simplify stress calculations, the calculations are usually done in 2D. Stress can be resolved into normal and shear stresses as well as expressed as the tensor multiple of stress and directional components through Cauchy's law (Equation 12). In order to make stress calculations easier a graphical representative method called as Mohr's circle is used. The Mohr circle is a convenient way of representing the normal and shear forces acting on all the planes in all possible orientations. The Mohr circle was conceived as a way of visualizing stress transformations and the relationship between normal and shear stresses. The Equations for the Mohr circle can be derived from the transformation Equations for plane stress. Considering geological convention and taking compressive stress as positive the Equations for normal and shear stress can be written in terms of the principal stresses as:

$$\sigma_n = \frac{1}{2}(\sigma_1 + \sigma_2) + \frac{1}{2}(\sigma_1 - \sigma_2)\cos 2\theta \tag{18}$$

$$\tau = -\frac{1}{2}(\sigma_1 - \sigma_2)\sin 2\theta \tag{19}$$

Where σ_n is the normal stress, τ is the shear stress, σ_1 is the maximum principal stress and σ_2 is the minimum principal stress. The Equations can be rearranged to get the Equation:

$$\{\sigma_n - \frac{1}{2}(\sigma_1 + \sigma_2)\}^2 + \tau^2 = \{\frac{1}{2}(\sigma_1 - \sigma_2)\}^2 \tag{20}$$

Equation 20 is similar to the Equation of a circle having

$$r = \{\frac{1}{2}(\sigma_1 - \sigma_2)\} \tag{21}$$

$$a = \{\frac{1}{2}(\sigma_1 + \sigma_2)\} \tag{22}$$

where *r* is the radius, and *a* is the distance of the center of the circle from the origin. The differential stress as given in Equation 15 would be the diameter of the circle and the mean stress assuming 2D stress would give the center of the circle. This circle which helps understand 2D stress better is called as the Mohr Circle. Figure 2.5 gives an illustration of a Mohr circle diagram.

The existence of different stress regimes within the subsurface causes the creation of faults. Faults are geologically created shear fractures in which the opposing faces of the rock move relative to each other. The fracture is characterized by its surface called as the fault plane and its strike and dip. The strike refers to the direction of any horizontal line in the fault plane and the dip is the angle between the horizontal plane and the fault plane with respect to the plane which is normal to the fault plane. The relative motion of the opposing faces of the fault is dependent upon the nature and orientation of the principal stresses acting on the fault. Assuming that the vertical stress is one of the principal stresses then three cases arise:

- Normal Faulting Regime. When the vertical stress is the greatest principal stress then this type of faulting occurs, [$\sigma_V > \sigma_H > \sigma_h$].
- Strike–slip Fault Regime: When the maximum horizontal stress is also the maximum principal stress and the vertical stress is the intermediate principal stress it results in this type of faulting regime, [$\sigma_H > \sigma_V > \sigma_h$].
- Thrust Fault Regime: When the maximum horizontal stress is the maximum principal stress and the vertical stress is the minimum principal stress it results in this fault regime, [$\sigma_H > \sigma_h > \sigma_V$].

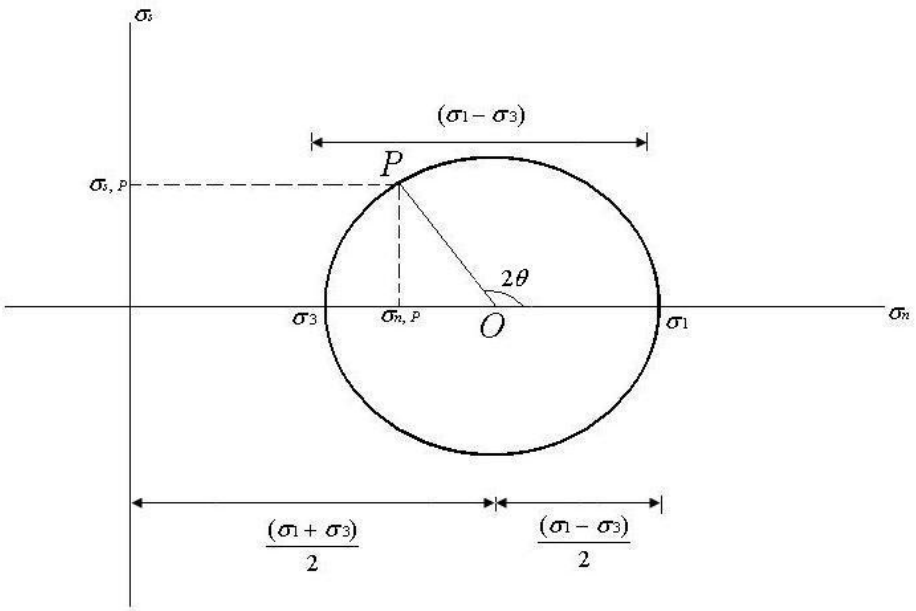

Figure 2.5 Mohr diagram for stress. Point *P* represents plane of stress and corresponding shear and normal stresses are marked on the *Y* and *X* axes respectively. The angle made on the Mohr circle is twice the actual physical angle of failure measured between the plane of failure and minimum principal stress.

Stresses in the sub surface are influenced by the presence of pore pressure phenomenon. Pore pressure is the pressure acting on the fluids in the pore space of a formation and is given by Equation 24.

$$P_p = \rho_w g z \tag{23}$$

Where P_p is pore pressure, ρ_w is density of water, g is acceleration due to gravity, and z is depth from surface. The increase or decrease of pore pressure has a direct effect on the state of stress in the region which is called as the Terzaghi effective stress principle shown in Appendix D. The principle states that the total stress is the sum of the effective stress and the pore pressure. An increase in pore pressure causes a decrease in the mean stress, no change in the differential stress, there by pushing the Mohr circle towards either shear or tensile failure.

2.8. ROCK FAILURE

Rock failure is a complex phenomenon which is sought to be understood by mathematical descriptions of observed physical phenomena rather than derivation using the laws of physics. (Fjaer et al., 2008). Usually the critical stress at which a rock fails is called as the strength of the rock. However the nature of failure is a function of a number of other parameters such as anisotropy, in-situ stress regime and geometry. Thus the rock strength is defined based on the type of test which the rock is subjected to in a laboratory setting. The laboratory tests used to determine the different critical stress bearing capacities of the rock are:

- Uni-Axial Test – Zero Confining stress
- Tri-Axial Test – Non Zero Confining Stress
- Brazilian Tensile Stress

The first two i.e. the uniaxial and the triaxial are used to determine the shear strength of the rock while the third is used to determine the tensile strength of the rock.

2.8.1. Tensile Failure. The critical tensile stress at which a rock fails is called as the tensile strength of the rock. It is usually denoted as T_0 and is expressed in the same units as stress. Figure 2.6 shows the schematic for loading a rock to tensile failure. The rock sample is subjected to a Brazilian Tensile test in which the load is applied normally. Usually the conditions for tensile failure are fulfilled first so that the stress corresponding to tensile failure represents the lowest principal stress (Fjaer et al., 2008).

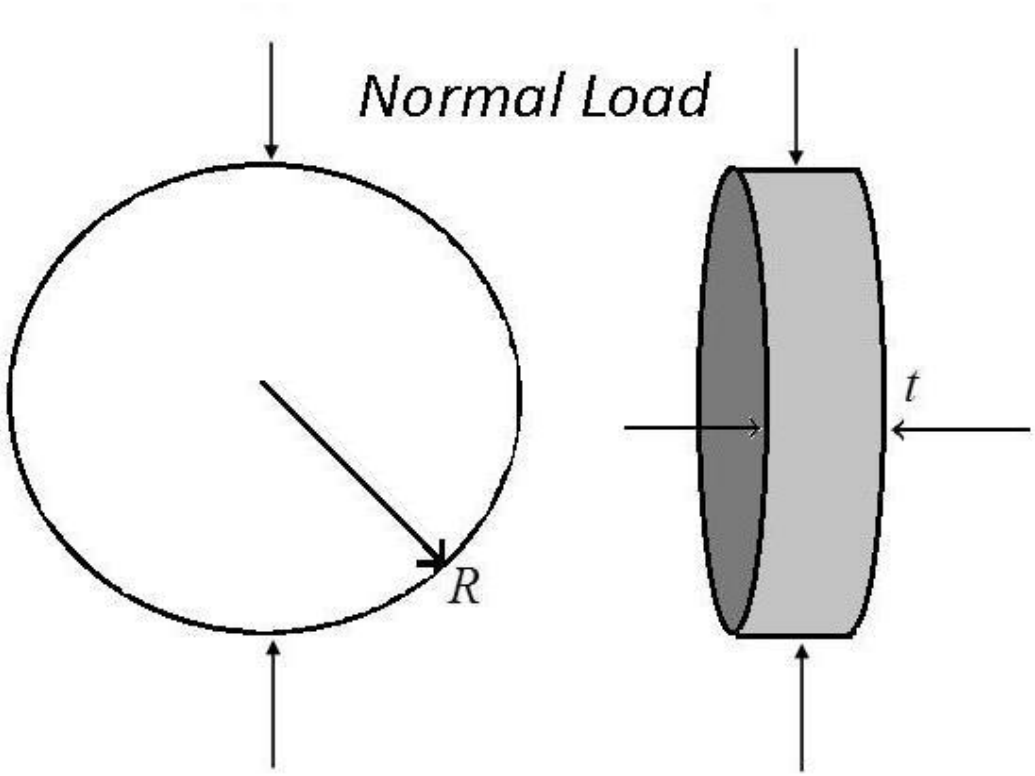

Figure 2.6 Loading to cause tensile failure .The rock sample is subjected to a normal load until it fails.

2.8.2. Shear Failure. The critical shear stress which causes failure of the rock is the shear strength of the rock. It initiates in the form of a fault zone which then results in the movement of the two faces of the fault moving relative to each other. Figure 2.7 shows a specimen having undergone shear failure.

2.8.3.Mohr – Coulomb Failure Criterion. This is one of the most commonly used failure criterions. It establishes a linear relation which shows that the shear stress causing failure is resisted by the cohesion of the material and the multiple of the coefficient of friction and the normal stress. Equation (24) represents this criterion.

$$\tau = S_0 + \mu\sigma \tag{24}$$

Where τ is the shear stress, σ is the normal stress, μ is the coefficient of friction and S_0 is the cohesion.

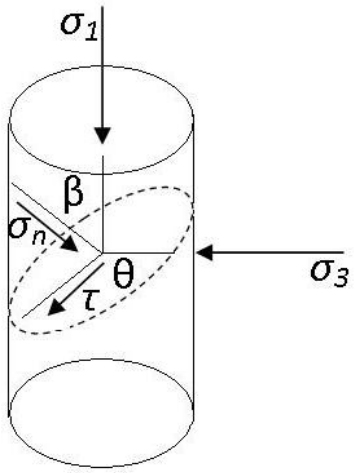

Figure 2.7 Cylindrical Sample undergoing shear failure. In triaxial tests, under the effect of confining pressure, the sample fails by developing a through going fault.

The Mohr failure envelope is obtained as the curve joining the points of failure of the rock, by loading rock samples to failure under different minimum horizontal stress conditions and then plotting Mohr circles of each case. If the potential stress conditions cause the drawn Mohr circle to cross the Mohr envelope it results in failure of the rock. Figure 2.8 shows the development of the Mohr failure envelope.

The data obtained from the triaxial test which is relevant for determining the Mohr Coulomb failure envelope are the minimum horizontal and maximum vertical stress at the point of failure of the rock. Multiple such experiments are carried out to generate a σ_1-σ_3 plot. The coefficient of this plot gives the Mohr Coulomb unconfined compressive strength while the slope serves as the input to calculate the angle of friction, cohesion and angle of failure. Figure 2.9 shows such a σ_1-σ_3 plot. Equation 25 shows the

relations for calculating the angle of friction and Equation 26 shows the expression for calculating cohesion from the slope of the trend line for the σ_1-σ_3 plot. Equation 27 shows the relation between angle of friction (φ) and coefficient of friction (μ).

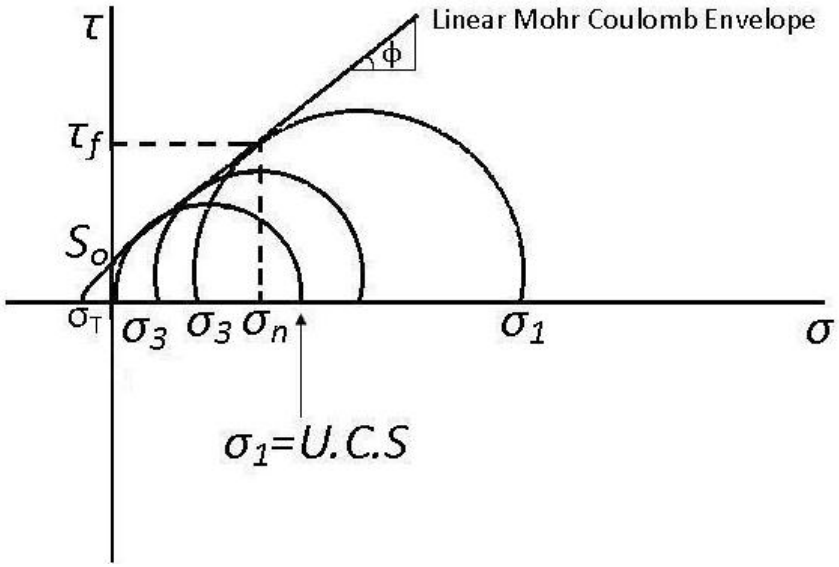

Figure 2.8 Mohr Failure Envelope based on multiple tests with principal stress values at failure

$$\phi = \sin^{-1}\left[\frac{m-1}{m+1}\right] \tag{25}$$

Where φ is the angle of friction and m is slope of trendline of σ_1-σ_3 plot.

$$S_o = \left[\frac{\sigma_c}{2}\right]\left[\frac{1-\sin\phi}{\cos\phi}\right] \tag{26}$$

Where S_o is cohesion, σ_c is unconfined compressive strength, φ is angle of friction.

$$\mu = \tan(\phi) \tag{27}$$

Once the cohesion (S_o) and coefficient of friction are known they can be entered into Equation 25 to get the Equation for the Mohr Coulomb envelope.

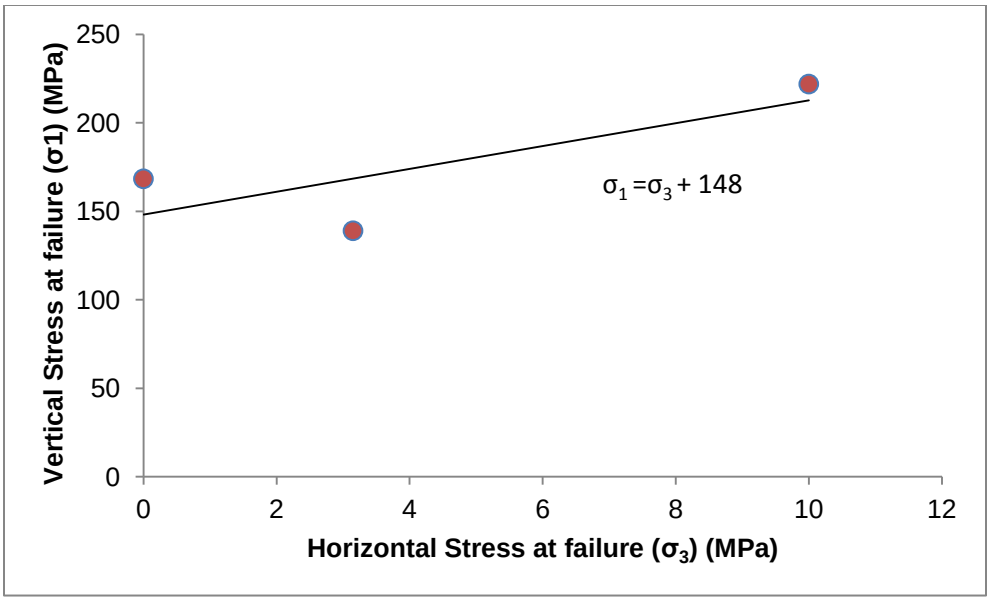

Figure 2.9 Illustration of $\sigma_1 - \sigma_3$ plot

2.8.4. Mohr Coulomb In s-t Space. This is a modification of the Mohr Coulomb criteria in which instead of the envelope being tangent to the Mohr circle it is drawn through the points of maximum shear stresses (Bardet, 1997). This modification yields a more conservative failure envelope as compared to the linear Mohr Coulomb which is based off of actual failure points with no margin of safety. The s-t space is a notation adopted by the Massachusets institute of technology, and it refers to the apex of the Mohr circles corresponding to the maximum shear stress on the Mohr circle (Nott, 2009). Figure 2.10 shows the s-t space version of the Mohr Coulomb envelope in comparison with the linear version.

2.8.5. Hoek Brown Criterion. The Hoek Brown criterion was first conceived of in 1980 to understand brittle failure observed in hard rocks. It sought to prove that the rock mass behaves as a continuum and that failure was controlled by jointing and with no preferred failure directions. Revisions have been made to the original criterion with the most up to date version being the 2002 version (Hoek et al., 2002). The Hoek Brown

curve is a non linear empirical formulation differing from the linear Mohr Coulomb criterion. Equation 28 shows the general expression for the Hoek Brown criterion.

$$\sigma_1 = \sigma_3 + \left[\sigma_{ci}\right]\left[m_b \frac{\sigma_3}{\sigma_{ci}} + s \right]^a \tag{28}$$

Where m_b is a reduced value of a material constant given by Equation 29.

$$m_b = m_i \exp\left[\frac{GSI - 100}{28 - 14D}\right] \tag{29}$$

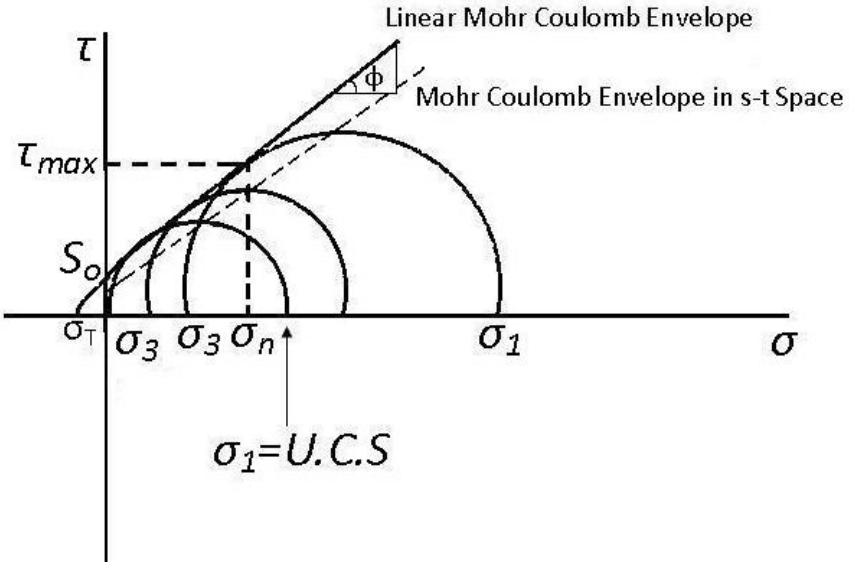

Figure 2.10 Mohr Coulomb envelope in s-t Space. The envelope diverges from the linear version which denotes actual failure points whereas the s-t Space criterion passes through maximum shear points.

S and *a* are constants for the rock mass given by Equations 30 and 31. *GSI* stands for geological strength index which is a characterization system based heavily on

fundamental geological observations. *D* is a disturbance factor that can account for blast damage and stress relaxation with values ranging from 0 for undisturbed conditions to 1 for very disturbed rock masses.

$$S = \exp\left[\frac{GSI - 100}{9 - 3D}\right] \tag{30}$$

$$a = \frac{1}{2} + \frac{1}{6}\left[e^{(-GSI/15)} - e^{(-20/3)}\right] \tag{31}$$

The uniaxial compressive strength is obtained by using the relation shown in Equation 32 and the tensile strength is shown in Equation 33.

$$\sigma_c = \sigma_{ci}(s^a) \tag{32}$$

$$\sigma_t = \frac{\sigma_{ci}(s)}{m_b} \tag{33}$$

Normal and shear stresses are related to the principal stresses according to Equations 34 and 35.

$$\sigma_n = \frac{\sigma_1 + \sigma_3}{2} + \frac{\sigma 1 - \sigma 3}{2} * \left[\frac{d\sigma_1/d\sigma_3 - 1}{d\sigma_1/d\sigma_3 + 1}\right] \tag{34}$$

$$\tau = (\sigma_1 - \sigma_3)\frac{\sqrt{d\sigma_1/d\sigma_3}}{d\sigma_1/d\sigma_3 + 1} \tag{35}$$

Where

$$d\sigma_1/d\sigma_3 = 1 + am_b(m_b(\sigma_3/\sigma_{ci}) + s)^{a-1} \tag{36}$$

The Mohr Coulomb criterion parameters can be obtained from the Hoek Brown plot by fitting a curve which yields the following relations for φ and S_o.

$$\phi = \sin^{-1}\left[\frac{6am_b(s+m_b\sigma_{3n})^{a-1}}{2(1+a)(2+a)+6am_b(s+m_b\sigma_{3n})^{a-1}}\right] \tag{37}$$

$$c = \left[\frac{\sigma_{ci}\left[(1+2a)s+(1-a)m_b\sigma_{3n}\right](s+m_b\sigma_{3n})^{a-1}}{(1+a)(2+a)+\sqrt{(1+[(6am_b(s+m_b\sigma_{3n})^{a-1})/(1+a)(2+a))]}}\right] \tag{38}$$

Where

$$\sigma_{3n} = \frac{\sigma_{3\max}}{\sigma_{ci}} \tag{39}$$

2.9. DYNAMIC MEASUREMENTS

One of the methods of acquiring rock properties through non-destructive testing is the laboratory pulse test. In this the velocity of stress waves through the rock samples is measured between parallel ends containing piezoelectric crystals in between which the core sample is placed. A high frequency electrical pulse is emitted by one end which passes through the core sample as a stress wave and is received by the second end. The received wave form is aligned with the sent wave form on an oscilloscope and the required delay to achieve this is measured as the travel time through the specimen. The parallel ends contain crystals capable of measuring both the primary as well as the secondary wave which are measured as the P-velocity (V_p) and S-velocity (V_s) Once the measurements are made the deformation properties are calculated using the following relations:

$$\nu = \frac{\left[V_p{}^2 - 2V_s{}^2\right]}{2\left[V_p{}^2 - V_s{}^2\right]} \tag{40}$$

$$E = \frac{\rho V_s^{\,2}\left[3V_p^{\,2} - 4V_s^{\,2}\right]}{\left[V_p^{\,2} - V_s^{\,2}\right]} \tag{41}$$

$$K = \frac{\rho\left[3V_p^{\,2} - 4V_s^{\,2}\right]}{[3]} \tag{42}$$

$$G = \rho V_s^{\,2} \tag{43}$$

Where V_p is compressional P wave velocity (m/s), V_s is shear S wave velocity (m/s), P is density (kg/m^3), v is Poisson's ratio, E is Young's modulus (Pa), K is bulk modulus (Pa), G is shear (rigidity) modulus (Pa).

3. GEOLOGY, SELECTION AND PREPARATION OF CORE SAMPLES

3.1. GENERAL GEOLOGIC BACKGROUND

The rock used for testing in this research was cored from outcrops of formations encountered in the region under consideration for CO_2 sequestration. The region under consideration for the CO_2 sequestration is the South West Missouri. The formation selected as a possible reservoir for CO_2 storage was the Lamotte sandstone. The upper cambrian lamotte sandstone rests on the Precambrian basement and is overlaid successively by the upper cambrian Bonne Terre Dolomite, Davis and Derby Doe Run formations. All of these formations form part of the Ozark uplift. The Ozark Dome is an asymmetrical uplift with the apex located in South eastern Missouri with formations exposed in an area called as the St.Francois Mountains. Figure 3.1 shows the detailed stratigraphy of the Cambrian Lamotte and the overlying formations.

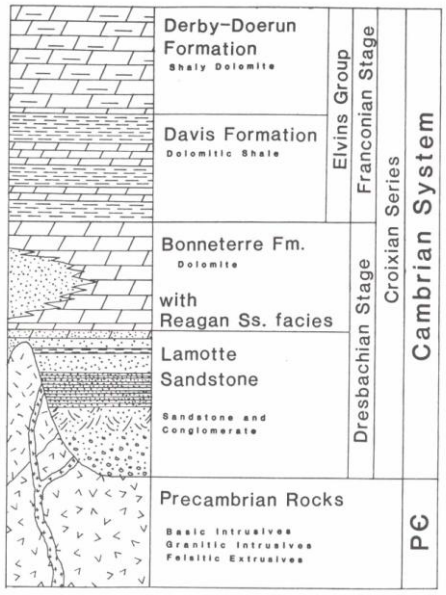

Figure 3.1 Stratigraphy of Site of Interest (Boongird et al., 2006)

3.1.1. Lamotte Sandstone. The Lamotte sandstone is an Upper Cambrian and is the lowermost Paleozoic sedimentary formation observed in the state of Missouri. It lies on unstratified Precambrian lithologies which are mostly igneous or metamorphic in nature and is over laid by the Bonne Terre dolomite. The Cambrian age was between 544 to 505 million years ago and was characterized by a shallow continental sea overlying Missouri which existed nearer to the equator. The rocks which date back to the Cambrian age are mostly sedimentary formed by the compaction of chemicals which originated from the weathering, transport, deposition and lithification of other rocks (Boongird et al., 2006).

3.1.2. Bonne Terre Dolomite. The Bonne Terre Dolomite is also an upper Cambrian rock formation. It lies above the Lamotte sandstone and under the Elvins. The Bonne Terre formation has a complex lithography and thickens gradually with the minimum thickness being in the south western part of Missouri and the maximum in the south eastern part. Lyle (1973) had conducted a detailed facies and petrography report and named four facies, fore reef, reef complex, back reef and offshore facies.

3.1.3. Elvin's Group. The Elvins' group refers to the dual formations of Davis and Derby Doe Run dolomitic formations. The Davis is characterized by high shale content and is believed to have an unconformable contact with the underlying Bonne Terre dolomite and having a conformable contact, wherever identifiable, with the overlying Derby Doe Run formation. The limited porosity and permeability of the Davis and Derby Doe run formations helps the Elvin's group to function as the seal / cap rock restricting the carbon dioxide in place.

3.2. SAMPLE GEOLOGY & SELECTION

The samples had to be representative of the actual site geology and hence the source rocks were outcrops of the relevant formations. Sourcing refers to the breaking of the rock from the rock outcropping to be used as a source for rock samples. The source rocks for each rock type were obtained from the sites as shown in Table 3-1. The points

which were considered during the selection of a particular rock as a source rock for the samples are as shown below:

- Orientation with respect to magnetic north of the rock before sourcing
- Weathering – rocks which were subject to least weathering were to be selected as source rocks
- Bedding, bedding faults
- Consistency in composition of the rock based on visual inspection

Table 3-1 Sampling details

Formation	Lithology	Depth	GPS Co-ordinates
Bonne Terre	Shaly Dolomite	Outcrop	N37°49'735" W90°40'48"
Davis	Shaly Dolomite	Outcrop	N37°51'8251" W90°33'7614"
Derby Doe run	Shaly Dolomite	Outcrop	N37°49'8881" W90°31'6696"
Lamotte	Sandstone	Outcrop	N37°49'735" W90°34'789"

3.3. SAMPLE PREPARATION

The samples were prepared by coring from the collected rocks. The core sizes and sample dimensions were dependent upon the experiment to be performed. The experiments included the Brazilian test, the uniaxial and the triaxial test. The sample dimension requirements were the same for the uniaxial and the triaxial. The sampling process involved coring from the source rock, cutting with a diamond bit rock saw and grinding of ends where required. Individual sample characteristics have been summarized in Appendix A.

3.3.1. Sample Preparation For Brazilian Test. Test specimens were about 2” in diameter and about 1” in length as shown in Figure 3.2., the guideline being that the L/D ratio should lie between 0.2-0.5 according to ISRM standards (1977). Grounding of

cylindrical ends was not required. Samples were cored using a 2” coring bit and longer cored samples were cut using a rock saw. Grinding of ends is not required for the Brazilian test.

3.3.2. Sample Preparation For Uniaxial/Triaxial Test. Test specimens were 1.5” in diameter and 3” in length as shown in Figure 3.3, the guideline being that the L/D ratio should lie between 2-2.5 according to ISRM standards (1972). Samples were cored using a 1.5” coring bit. Longer cored samples were cut using a rock saw and grounding of cylindrical ends was required. The ends are grounded to ensure that ends are parallel to each other and perpendicular to the sides of the core.

Figure 3.2 Brazilian Test Sample Dimensions

Figure 3.3 Uniaxial/Triaxial Testing Sample Dimensions

4. LABORATORY EXPERIMENTAL SETUP & PROCEDURE

This chapter describes the details of the developed laboratory setup to conduct the rock mechanical testing and the procedures required to operate the equipment. The unified testing system was developed to perform Brazilian, uniaxial and the triaxial tests with only slight modifications for each test type. The procedures used to conduct each of the tests follow the description of the setup and equipment operation procedure.

4.1. UNIFIED TESTING SYSTEM SETUP

A unified testing system having modifiable hardware and software components was developed to carry out the different rock mechanical tests. The strength properties of the rock can be derived from the rock deformation properties which are obtained from the rock mechanical experimental data. At the end of the experiment, a graph of stress v/s strain is generated from which the Young's modulus and Poisson's ratio are obtained. The cohesion and angle of friction are obtained from the graph of axial stress against confining stress. Axial Stress in MPa is obtained by monitoring the axial load using a load sensor and strain is monitored using a strain gauge system. Pumps are used to produce the axial loading and confining stresses. A workstation algorithm written in laboratory software (Labview^{TM}) is used to acquire and log the data in the form of voltage and produces a graphical output in the form of the stress strain graph.

4.2. UNIFIED TESTING SYSTEM COMPONENTS

The system was composed of the following components:

- Pump system
- Rock sample mounting rigs: Hoek Cell, Brazilian test rig.
- Data acquisition & measurement systems.

4.2.1. Pump System. The system consists of two syringe pumps; high pressure low volume pumps capable of pressures up to 10,000 psi. One of the pumps is used to create fluid based confining pressure which acts as two of the lower principal stresses which are equal in magnitude. The other pump is used to generate the fluid based normal load delivered through the loading piston mounted on a steel frame. The syringe pumps can be run from a control station and monitored remotely using a host computer.

4.2.2.Rock Sample Mounting Rigs. The mounting rigs have been devised for the Brazilian testing system and the Triaxial testing system. The uniaxial test does not require a mounting rig.

4.2.2.1. Brazilian test rig. Test specimens for Brazilian test were about 2 inches in diameter and about 1 inch in length. The samples are placed in a special rig constructed at the department workshop usable for sample sizes up to 3 inches in diameter. This rig is then subjected to normal loading while being monitored by the load sensor. Figure 4.1 illustrates the rig set up for Brazilian testing.

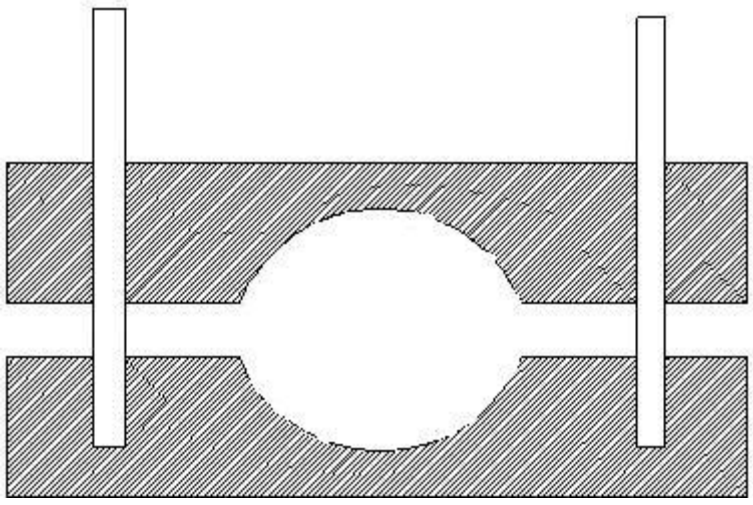

Figure 4.1Brazilian Test Rig

4.2.2.2.Uniaxial sample mounting. The rock sample is placed between the two steel platens as shown in Figure 4.2.

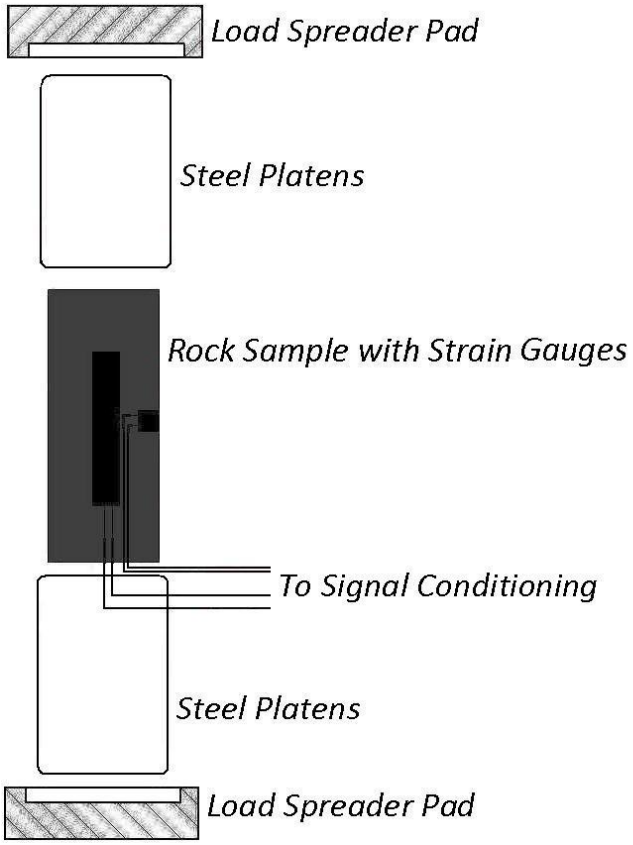

Figure 4.2 Uniaxial Sample Mounting

4.2.2.3. Triaxial test rig. For the Triaxial test the rock sample is loaded into a Hoek cell, which is a specially designed cell to subject the rock sample to triaxial forces. it consists of a rubber sleeve enclosure into which the rock sample is placed, surrounded by a steel cell. Fluid is pumped in the annulus between the rubber sleeve and the steel cell to create the confining pressure. The Hoek cell is placed between steel

platens over which the normal load is applied through the loading piston thus completing the triaxial testing conditions. Figure 4.3 illustrates the Hoek cell setup.

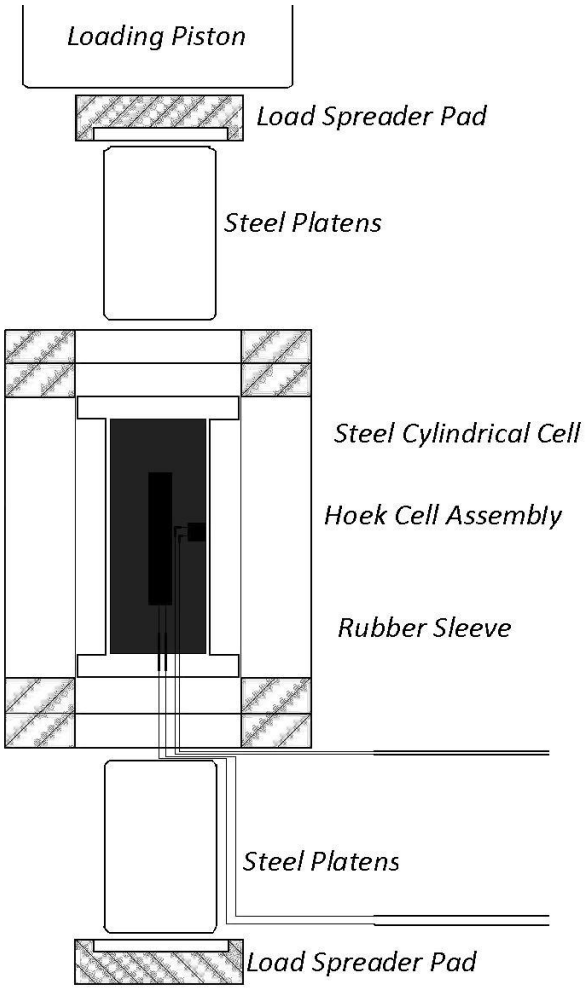

Figure 4.3 Hoek Cell with rock sample

4.2.3. Data Acquisition & Measurement System Components. It consists of the laboratory software package which accompanied the pumps and the control and data acquisition program developed in Labview to facilitate the mechanical testing of rocks. Three sub modules form the main program and can be used separately corresponding to

the rock test requirement. Analog measurements are converted to digital format with the data being written into a spreadsheet for further analysis. Finally graphical output is produced for calculation of rock deformation parameters.

4.2.3.1. Load sensor: The load sensor is used to monitor the normal load in all three tests with the reading being fed to the data acquisition device (DAQ1) which converts the analog data into digital data. The load sensor measures load in pounds (lbs). The data acquisition device (DAQ1) connects to the computer through an RS232 serial port and provides data to the Workstation algorithm written in Labview.

4.2.3.2.Strain measurement: The strain due to the loading is monitored using strain gauges which are attached to the rock sample. The strain is monitored in two directions axial and radial. The differential signal from the axial and radial strain gauge is fed to two identical signal conditioning systems to be amplified and fed to the data acquisition system (DAQ2). The signal conditioning system is an embedded board which completes a single wheatstone bridge in quarter, half or full bridge mode as well as amplifies the signal giving a ground referenced single ended output. The gain and the offset of the signal conditioning board can be configured using software. The voltage output from the two conditioning boards is fed to two different channels of the data acquisition device (DAQ2) which is run in differential mode to cancel out common mode noise. The strain gauge system is run in quarter bridge mode with the strain gauge serving as one of the arms. The DAQ2 is connected to the computer through a USB port and can be controlled using the Workstation algorithm written in Labview.

Figure 4.4 shows the unified testing system as modified for carrying out a triaxial test, while Figure 4.5 shows the same for a uniaxial test and Figure 4.6 shows the modification carried out for the Brazilian test.

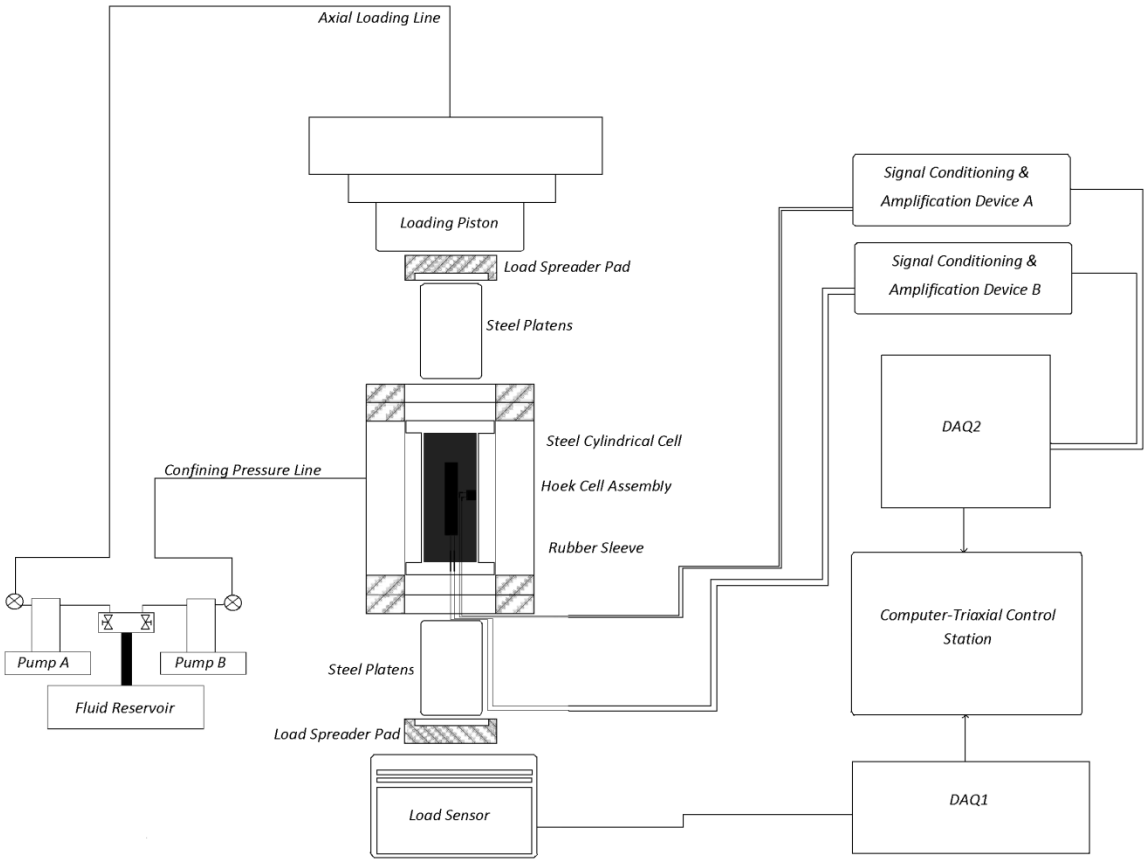

Figure 4.4 Unified testing system for triaxial testing

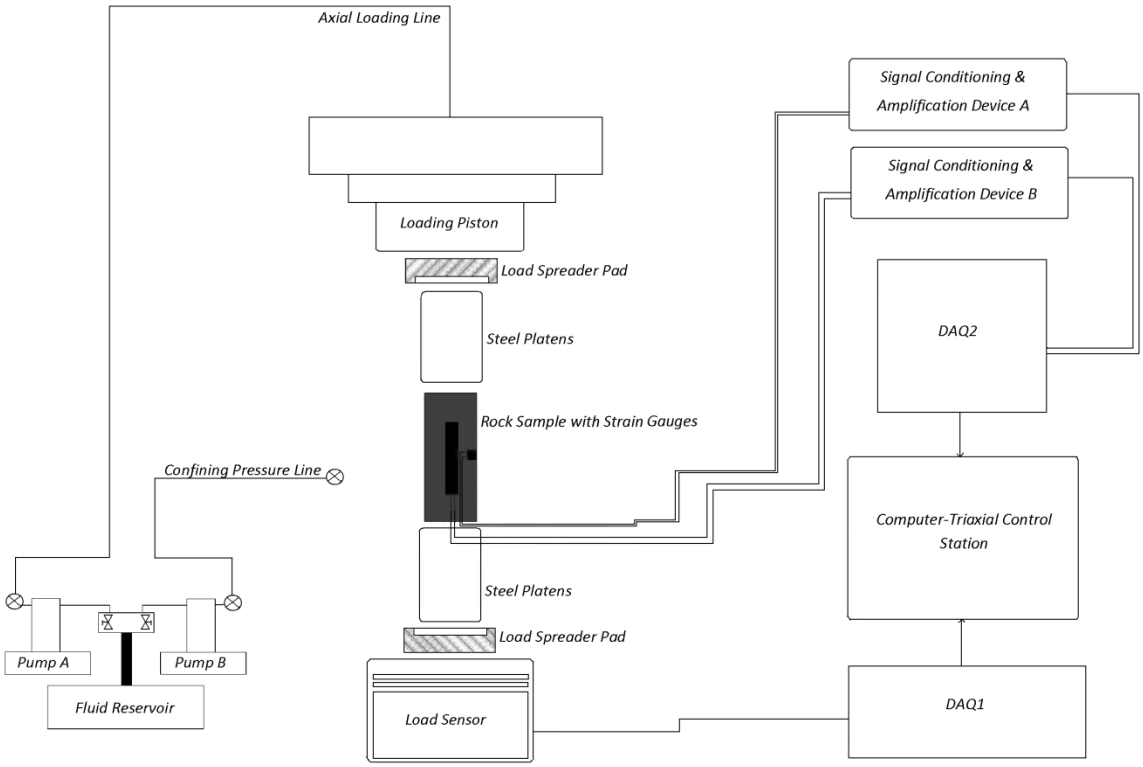

Figure 4.5 Unified testing system for uniaxial testing

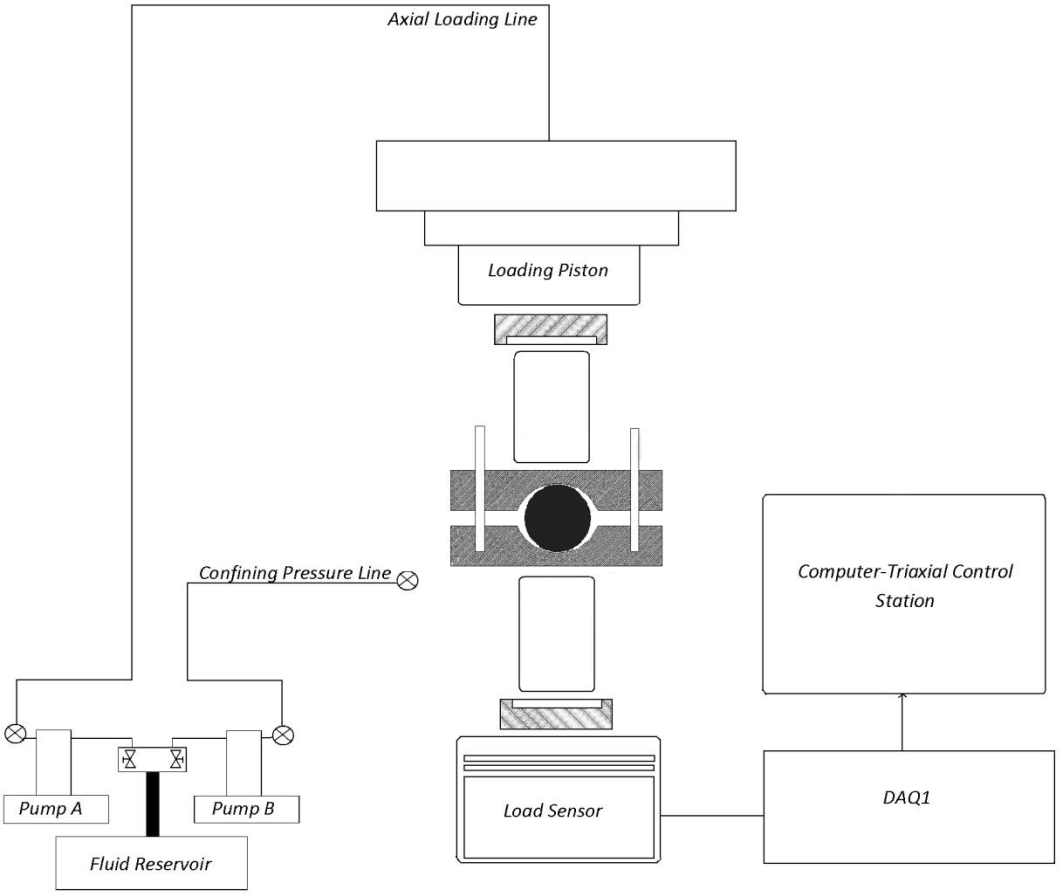

Figure 4.6 Unified testing system for brazilian testing

4.2.3.3. Workstation algorithm: The Workstation algorithm is written such that at the command of the user it acquires data from both the load sensor through the DAQ1 and the strain gauges through the DAQ2 producing a graphical result of the stress-strain plot. Three sub-modules together comprise the main program, two for acquisition from the strain gauges and one for data from the load sensor. The rate of data acquisition has to be set the same across the Labview VI monitoring the pumps, the DAQ1, the sub VI's acquiring strain data through the DAQ2 and the VI acquiring data from load sensor through the DAQ1.

- **Pseudo code for Data Acquisition from Strain Gauge:**

  - Wait for Start from user

- If (!Start) Then

  Keep Waiting

  Else

  - Collect Voltage data through Axial Strain Gauges through DAQ2 at 1/10 samples per second sampling rate.
  - Write Data to Measurement File
  - Initialize Constants:

    Gauge Factor (G.F) = 2.13

    V_{EXC} = 1.5 V
  - Perform Formula for Axial Strain:

$$\varepsilon_{Axial} = \left[\frac{-4V_O}{G.F \times (V_{EXC}) + 2 \times G.F \times V_O} \right]$$

  - Plot Axial Strain on positive X-Axis.

- Repeat same procedure as above for acquiring Radial Strain.
  - Plot Radial Strain on negative X-Axis.

- **<u>Pseudo code for Axial Stress (Load) Data Acquisition:</u>**

- Wait for Start from user

- If (!Start) Then
  Keep Waiting
  Else

  - Read Load Data from Serial Port at 9600 Baud Rate in pounds.
  - Write to Measurement File
  - Initialize Constants: Conversion Factor (C.F):
    C.F = $4.448*10^{-6}$
    Multiplying Factor (M.F):
    M.F = $0.5067*10^{-3}$
    Sample Diameter (D):
    D= 1.5 inches
  - Perform Formula

$$\sigma_{Axial} = \left[\frac{Load(lbs) \times C.F}{M.F \times D^2} \right]$$

- Plot Axial Stress on Y-Axis

4.3. LAB EXPERIMENTAL PROCEDURES:

The unified testing system makes it possible to carry out three rock mechanical tests within the same experimental framework. The system consists of three separate operational components: 1) the Pump system 2) Rock sample mounting rigs 3) Data acquisition and measurement systems; with slight modifications resulting in the setup adapting for different experiments. The operation of the pump system and the data acquisition and measurement system varies very little for all the experiments with the main changes being introduction of confining pressure in the triaxial test and the monitoring of strain. The most important change with respect to the three tests is the difference in the mounting of the rock sample with the additional attachment of the strain gauges when necessary.

4.3.1. Pump System Operation. The pump system consists of two pumps controlling the axial loading and the confining pressure. Each of the pumps has a separate controller used to program the operation of the pump. The axial loading system is used in all experiments whereas the confining pressure generation is required only in the triaxial test. The pumps are run in a programmed gradient mode. In the programmed gradient mode, the initial pressure from which the pressurizing of the sample is to begin and the final pressure to be attained can be programmed into the controller of the pumps. Programmed gradient mode has a step facility such that the pump will operate at a specific rate, for a specific time period and at a different rate over the next time period.

4.3.1.1. Axial loading pump operating procedure: The axial loading pump is always run in programmed gradient mode which increases pressure at a constant rate thus maintaining the strain rate constant. for the uniaxial and the Brazilian tests the axial pump is run independently and the rate can be kept constant as required. For the triaxial test the axial loading pump has to run in coordination with the confining pressure

pump, initially, so as to maintain a constant loading and confining rate till the desired confining pressure is reached. The pump is run in programmed gradient mode such that till the desired confining pressure is reached the pump can be set to operate at a set rate which would be the same as used for the confining pump. Once the confining pressure is reached the next rate can be set to achieve the final pressure in the desired duration.

4.3.1.2.Confining pressure pump operating procedure: The confining pressure pump is utilized only in the triaxial test and is also run in programmed gradient mode. The pump is set to increase pressure in coordination with the axial loading pump till the desired confining pressure is reached and then hold that pressure constant.

4.3.2.Rock Sample Mounting Rigs Operational Procedures. The method of mounting the sample is different for each of the rock mechanical tests.

4.3.2.1.Brazilian test: In this the rock sample is mounted in the Brazilian rig,shown in Figure 4.1. The rig with the mounted sample is then mounted in between the steel platen through which loading is done as shown in Figure 4.6.

4.3.2.2.Uniaxial test: A cylindrical rock sample with attached strain gauges is mounted in between the steel platens and the strain gauges are wired to the signal conditioning device as shown in Figure 4.2.

4.3.2.3.Triaxial test: This involves mounting a rock sample within the Hoek cell. Care should be taken to ensure that the strain gauge wires do not break during insertion of the rock sample into the Hoek cell. The Hoek cell is then mounted in between the steel platen through which axial load is applied. Fluid is pumped into the annulus between the rubber sleeve and steel casing of the Hoek cell to create confining pressure.

4.3.3.Data Acquisition & Measurement System Operational Procedures. The data acquisition procedure involves initializing the programs monitoring the processes of pressurization, loading and strain variation.

4.3.3.1.Pump pressurization: The program monitoring the pumps is a labview package supplied along with the pump called Iscopump. The pump program should be started after the pumps have reached initialization pressures and at the same time as the loading step. The pump program has been loaded in two different remote host devices (a laptop and a desktop) to monitor both the confining and the axial pump operations.

4.3.3.2. Loading and strain variation. A program monitoring the loading and the strain variation has been developed indigenously and is called as the triaxial control station (TCS). The TCS has to be initialized to log the load variation data and to monitor the voltage change signifying the strain variation.

4.4. TEST RUNNING PROCEDURES

4.4.1. Run Procedure Of A Brazilian Test. The Brazilian test is administered to find the tensile strength of the rock. Tensile failure has been covered in section 2.8.1. The Sample preparation for the Brazilian test has been covered in section 3.3.1. The system components for the Brazilian test are shown in Figure 4.6. The operation of the system components has been explained in section 4.3. The step by step procedure for running a Brazilian test on the lab set up is given below:

- Samples are to be assigned identification numbers and their dimensions and mass noted down in the Brazilian test log of the rock mechanical test excel with the geological data. Take photographs to keep a record of the test progress.
- To start the test, the sample is set up in the Brazilian Rig as shown in Figure 4.1 and Figure 4.6.
- Check to ascertain that the pump and the load sensor components are switched on.
- Start the software(s) monitoring the load sensor and the pumps setting the sampling time to be around 25 ms i.e. four samples in a second.
- The pump is run in a gradient mode with a constant rate of loading till tensile failure of the sample occurs.

- Take photographs of the broken samples for the record.
- The load at failure is entered into the Brazilian test log of the rock mechanical excel sheet to get the Brazilian strength of the sample.

4.4.2. Run Procedure Of A Uniaxial Test. The uniaxial test is administered to determine the unconfined compressive strength of the rock sample. The rock sample subjected to this test could undergo a shear failure as explained in Section 2.8.2., or it could undergo any of the different types of failure as shown in Figure 4.7 . The sample preparation has been described in Section 3.3.2. Figure 4.5 shows the system components for running a uniaxial test and system operation has been explained in Section 4.3. The step by step procedure for running a uniaxial test is as given below:

- The samples are assigned numbers and their dimensions and their mass is noted down in the uniaxial test log of the rock mechanical test excel sheet along with the geological details of the rock samples. Photographs are taken for keeping a record of the test progress.
- Axial and radial strain gauges are attached to the sample and the sample to be tested is loaded onto the mount as shown in Figure 4.2.
- All the system components are checked once to ascertain the settings.
- The software controlling the pump and the data acquisition software are initialized and sampling rate set to 10000 ms i.e. one sample every ten seconds.
- The axial loading pump is run in gradient mode to ensure a constant rate of loading and strain is monitored using the strain gauge system. The sample is loaded till the point of failure.
- The load value at point of failure is input into a rock mechanical test excel sheet to get the unconfined compressive strength.

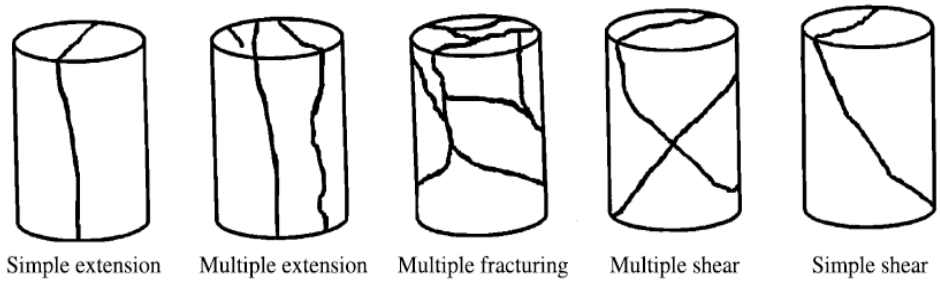

Figure 4.7 Modes of sample failure (Szwedzicki, 2007)

4.4.3. Run Procedure Of A Triaxial Test: The triaxial test is administered to determine the confined compressive strength of the rock sample. The triaxial test recreates the insitu conditions in the lab and gives a more accurate assessment of rock strength than the uniaxial test. In the triaxial test the rock sample is subjected to both, a confining pressure and axial loading. The strength estimate of the rock increases due to the application of a confining pressure which replicates an actual field scenario i.e. values of effective stresses are used in the experiment. The sample preparation has been described in Section 3.3.2. Figure 4.4 shows the system components for running a triaxial test and system operation has been explained in Section 4.3. The step by step procedure for running a triaxial test is as given below:

- The samples are assigned numbers and the dimensions and their mass is noted down in the triaxial test log of the rock mechanical test excel sheet along with the geological details of the rock samples. Photographs are taken for keeping a record of the test progress.
- Axial and radial strain gauges are attached to the rock sample and the sample to be tested is loaded onto the mount as shown in Figure 4.3. The mounting has to be done very carefully to ensure that the strain gauge connections do not break.
- All the system components are checked once to ascertain the settings.

- The software controlling the pump and the data acquisition software are initialized and sampling rate set to 10000 ms i.e. one sample every ten seconds.
- The axial loading pump is run in gradient mode to ensure a constant rate of loading and strain is monitored using the strain gauge system. The sample is loaded till the point of failure.
- The data from the test is collected and analyzed to get the stress-strain plot from which the elastic modulus and the Poisson's ratio can be obtained.

5. RESULTS & DISCUSSION

Geomechanical characterization of the formations of interest was done by analyzing the results of the rock mechanical testing. The rock mechanical tests included 18 Brazilian tensile tests, 6 uniaxial tests and 6 single stage triaxial tests accompanied by sonic velocity tests. Failure envelopes were generated based on the results of the tests and the data was compared to the in-situ data to predict the sustainable fluid pressures for underground storage of CO_2. The important assumptions included an Andersonian state of stress, negligible anisotropy and linear elastic rock properties.

5.1. TEST RESULTS

5.1.1. Brazilian Test Results. Eighteen Brazilian tests were conducted, six each on Bonne Terre Dolomite, Lamotte Sandstone and Davis shaly dolomite. The loading was done at the rate of 100 psi/min. The samples were loaded until failure and the maximum load in pounds (lbs) noted down as input towards the Brazilian tensile strength calculation as shown in Equation 44.

$$\sigma_t = \left[\frac{2 * 4.448 * lb}{\pi * d * l} \right] \tag{44}$$

Where σ_t is Brazilian Tensile Strength (MPa), *lb* is failure load (lbs), *l* is length (mm) *d* is diameter (mm).The details of sample characteristics are shown in Table A-1 of Appendix A. The lab worksheet summarizing all 18 tests is shown in Table B-1 of Appendix B. The tensile strengths were averaged and plotted in a graph as shown in Figure 5.1. It was found that the Bonne Terre dolomite had the highest tensile strength followed by the Davis and then the Lamotte.

5.1.2. Uniaxial Compression Test Results. Six uniaxial compressive tests were carried out, two each of the three formation rocks. The samples were loaded at a constant rate till failure and the maximum load in pounds (lbs) noted down as input towards the Ultimate Compressive Strength (U.C.S) calculation as shown in Equation 45.

$$U.C.S = \frac{\left[0.001*\left(\frac{lb}{224.808}\right)\right]}{\left[\pi*(0.0254)^2*\frac{D^2}{4}\right]} \tag{45}$$

Where *U.C.S* is Ultimate Compressive Strength in MPa, *lb* is load at failure in lbs, *D* is diameter of sample (inches). The sample characteristics are shown in Table A-2 in Appendix A. The lab worksheet showing the test summary is shown in table B-2 in Appendix B. The unconfined compressive strengths are averaged and plotted in Figure 5.2. In the uniaxial tests the Bonne Terre Dolomite was again found to have the highest strength value followed by the Davis shaly dolomite and then the Lamotte sandstone.

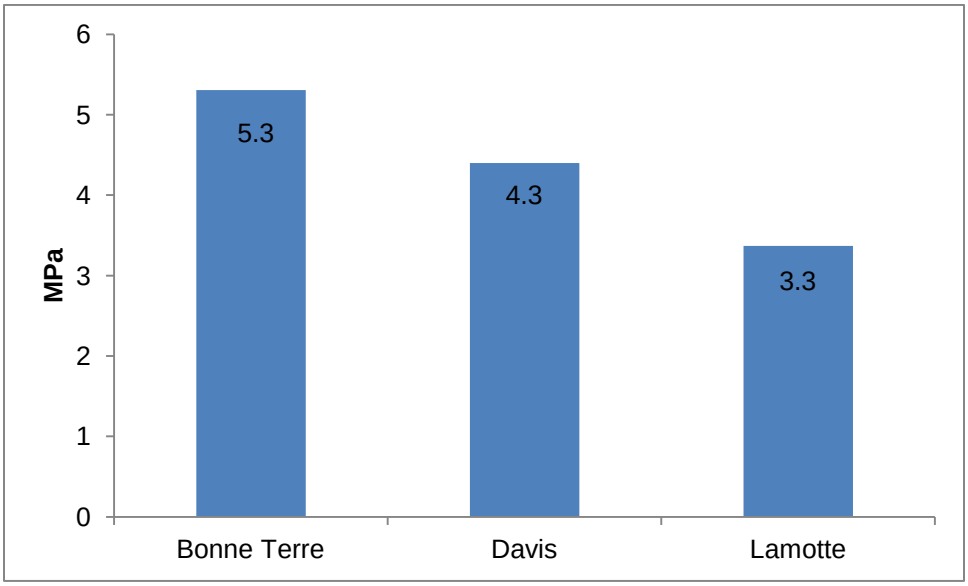

Figure 5.1Averaged Brazilian tensile strength

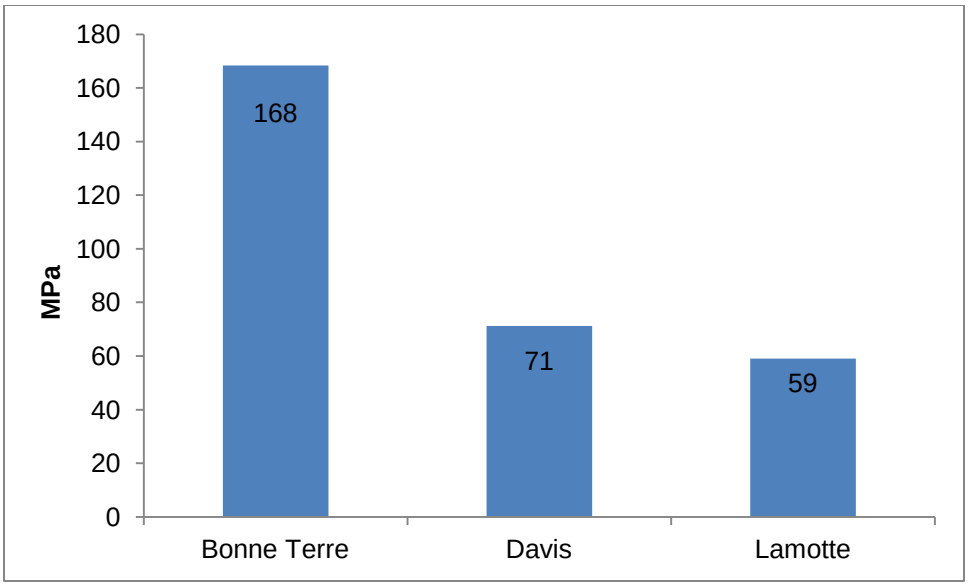

Figure 5.2 Averaged U.C.S data for the three rock formations

5.1.3. Triaxial Test Results. Six triaxial tests were carried out, two each of each rock formation type. The sample characteristics are shown in table A-3 in Appendix A. The tests were carried out at in-situ stress conditions and at 10 MPa. The in-situ stress values were initially estimated assuming a Poisson's ratio of 0.2 and an Andersonian state of stress ($\sigma_v > \sigma_H > \sigma_h$). The summary of the triaxial tests is given in table B-3 in Appendix B. Figure 5.3, Figure 5.4 and Figure 5.5 show the $\sigma_1 - \sigma_3$ graphs for the three rock types. Stress – strain curves are obtained at the end of the experiment providing the deformation properties. The stress strain curves of all the triaxial tests are shown in Appendix C. Table 5-1 shows the summary of the deformation properties obtained from the triaxial tests.

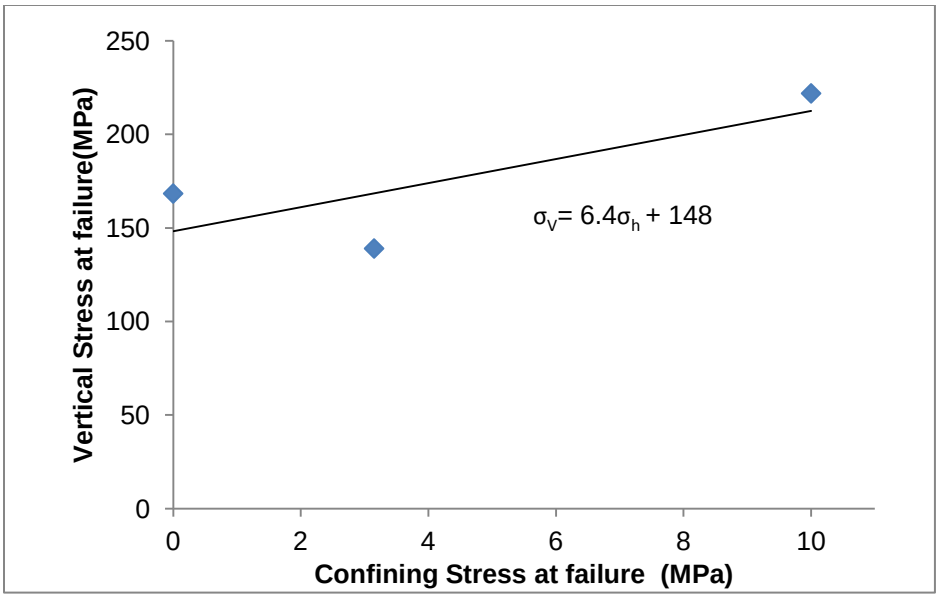

Figure 5.3 Maximum and minimum principal stress regime at points of failure of Bonne Terre dolomite samples

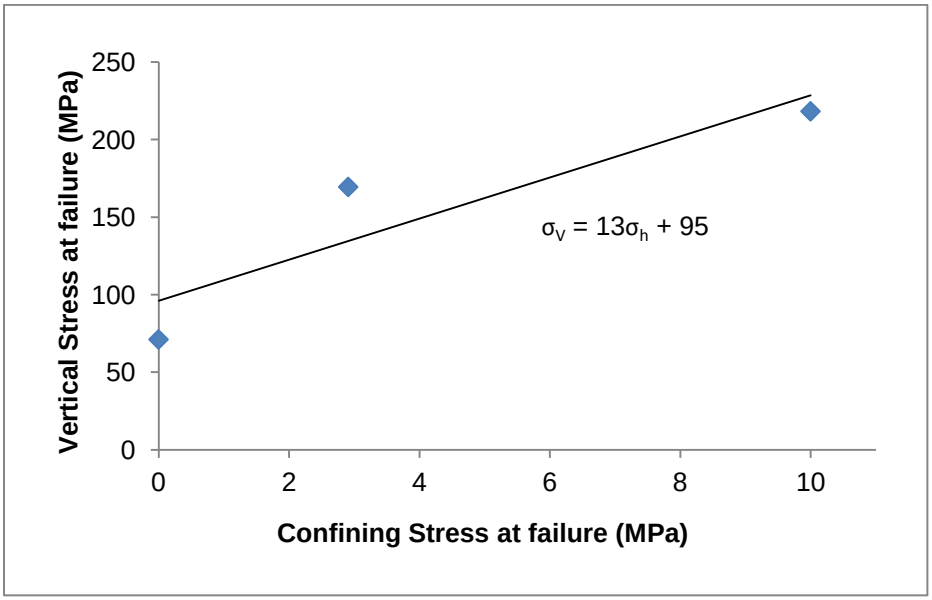

Figure 5.4 Maximum and minimum principal stress regime at points of failure of Davis shaly dolomite samples

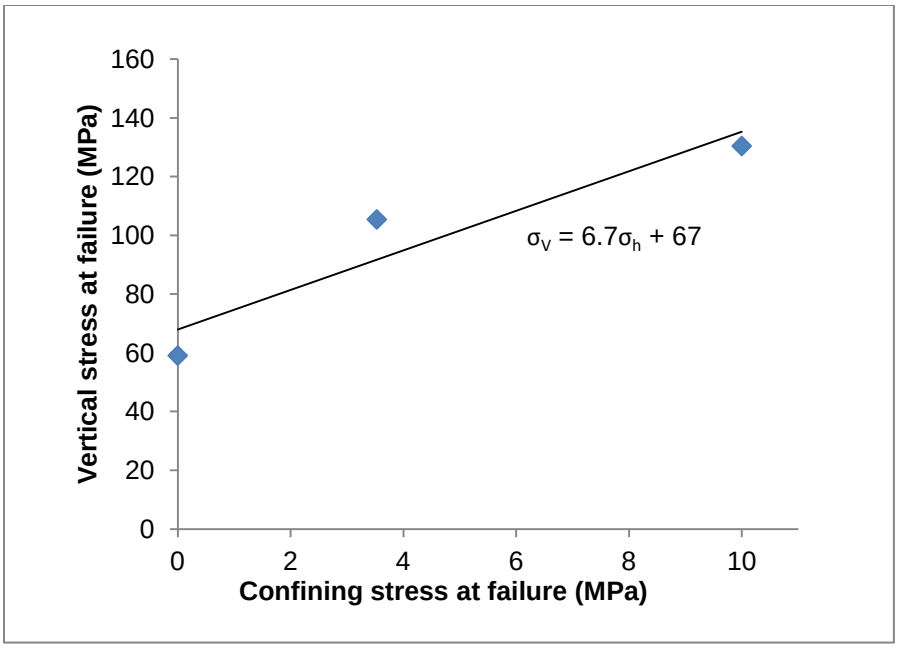

Figure 5.5 Maximum and minimum principal stress regime at points of failure of Lamotte Sandstone samples

Table 5-1 Rock deformation properties summary

Rock Type	Date of Test	Sample Name	E	ν	G	K
			GPa		GPa	GPa
Bonne Terre dolomite	2nd April	Batch I Sample B	60	0.40	21	100
	26th April	Batch II Sample A	52	0.19	22	28
	Avg		56	0.29	21	64
Davis shaly dolomite	21st March	Batch I Sample A	55	0.15	24	27
	19th April	Batch I Sample B	46	0.41	16	85
	Avg		51	0.28	20	56
Lamotte Sandstone	30th April	Batch I Sample B	23	0.35	8	27
	30th April	Batch I Sample A	37	0.27	14	28
	Avg		30	0.31	11	27

5.1.4. Sonic Velocity Tests. The sonic velocity test was carried out on the six samples which were used for the triaxial test as a means of predicting the range of values to be expected for the deformation properties of the rock samples. The tests were carried out using two methods which only differed in the selection of the point of reference. The difference in the reference point gave completely different results which are shown in tables Table 5-2 and Table 5-3. In the first interpretation the reference point used was the first valley whereas in the second the trigger i.e. the point just before the occurrence of any event (valley or peak) is used as the reference.

Table 5-2 Deformation properties based on first valley reference point

Rock Type	Sample Name	Sonic Test No	P - Velocity	S- Velocity	E	ν	G	K
			m/s	m/s	GPa		GPa	GPa
Bonne Terre dolomite	Batch I Sample B	1	3890	2854	39	-0.08	21	11
		2	3895	2857	39	-0.08	21	11
	Batch II Sample A	1	3723	2963	30	-0.36	23	5
		2	3828	2956	36	-0.24	23	8
Lamotte sandstone	Batch I Sample A	1	3035	2253	19	-0.11	11	5
	Batch I Sample B	1	3050	2199	201	-0.04	10	6
Davis shaly dolomite	Batch I Sample B	1	3786	2614	37	0.04	17	13
		2	3822	2675	38	0.02	18	13

Table 5-3 Deformation properties based on trigger reference point

Rock Type	Sample Name	Sonic Test No	P - Velocity m/s	S- Velocity m/s	E GPa	ν	G GPa	K GPa
Bonne Terre dolomite	Batch I Sample B	1	6479	3523	84	0.29	32	67
		2	6326	3492	82	0.28	32	62
	Batch II Sample A	1	6622	3465	85	0.31	32	75
		2	6677	3511	87	0.31	33	76
Lamotte sandstone	Batch I Sample A	1	4280	2531	34	0.23	14	21
	Batch I Sample B	1	4508	2487	34	0.28	13	26
Davis shaly dolomite	Batch I Sample B	1	5579	3030	62	0.29	24	49
		2	6070	3162	68	0.31	26	61

5.2. DATA INTERPRETATION & ANALYSIS

5.2.1. Failure Envelopes. The results of the Brazilian, uniaxial tests were combined with those of the triaxial tests to get the failure envelope characterizing the rocks. The Mohr-Coulomb, Mohr-Coulomb in s-t space and Hoek Brown criteria were used to generate the failure envelopes. Table 5-4 and Table 5-5 show the calculated Mohr Coulomb and Hoek Brown parameters. Figure 5.6, Figure 5.7 and Figure 5.8 show the failure envelopes generated for each of the rock types. The Mohr Coulomb parameters were calculated using both, the Mohr Coulomb Equations and interpolated from the values returned by the Hoek Brown Equations.

Table 5-4 Mohr Coulomb parameters

Formation	Lithology	Criteria	U.C.S MPa	φ°	S_o MPa
Davis	Shaly Dolomite	M-C	96.00	59.26	13.19
		H-B	83.24	41.52	31.40
Lamotte	Sandstone	M-C	67.93	47.84	13.09
		H-B	64.11	30.59	17.32
Bonne Terre	Dolomite	M-C	148.17	49.99	29.19
		H-B	149.03	31.08	28.45

Table 5-5 Hoek Brown parameters

Rock Type	Classification Parameters					Criterion Parameters		
	sigci	GSI	mi	D	Ei	mb	s	a
	MPa				MPa			
Davis	83.24	86.00	50.00	0.00	33950	30.33	0.21	0.5
Lamotte	64.11	80.00	18.28	0.00	30700	8.95	0.11	0.5
Bonne Terre	149.03	82.00	11.99	0.00	56300	6.30	0.14	0.5

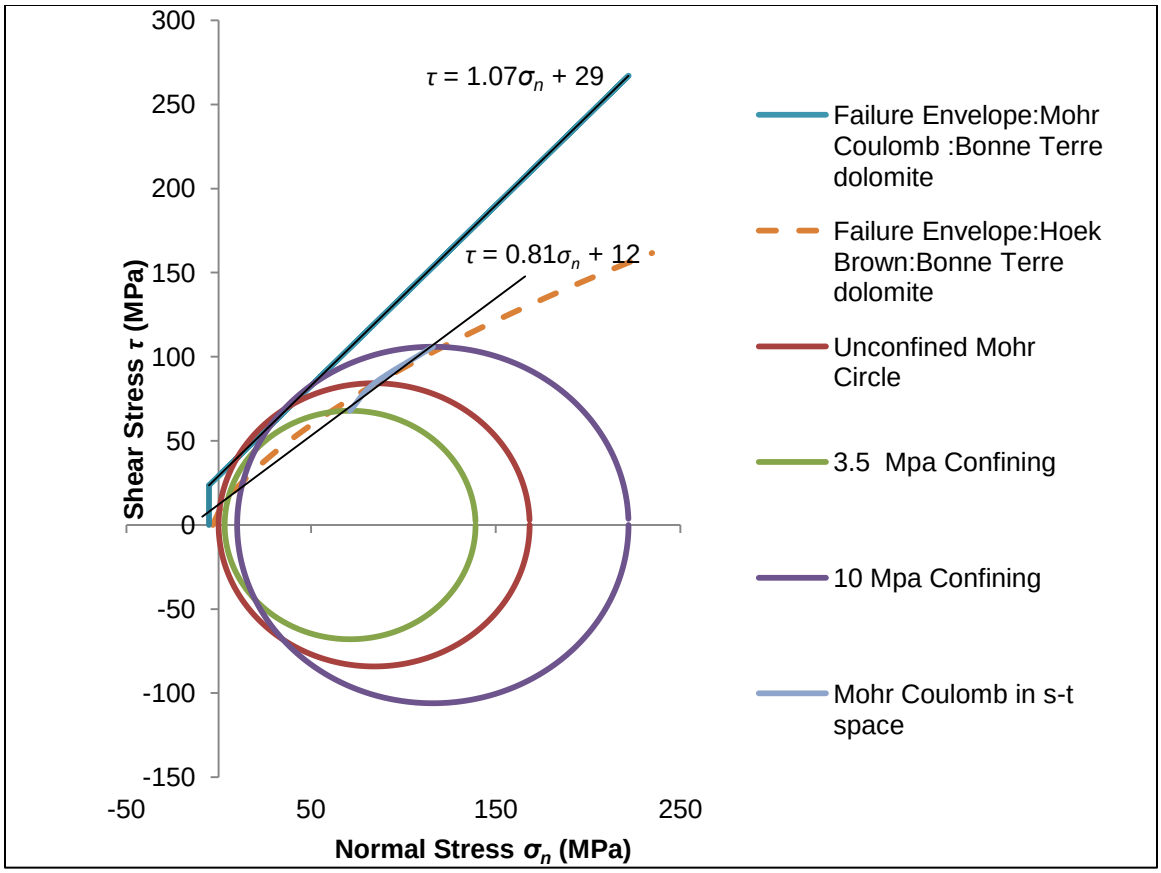

Figure 5.6 Failure envelopes for Bonne Terre dolomite, linear Mohr Coulomb, non-linear Hoek Brown and linear Mohr Coulomb in s-t space. Mohr circles have been plotted for unconfined, in-situ and 10 MPa confining stress values. Equations for the linear Mohr Coulomb and Mohr Coulomb in s-t space has been shown

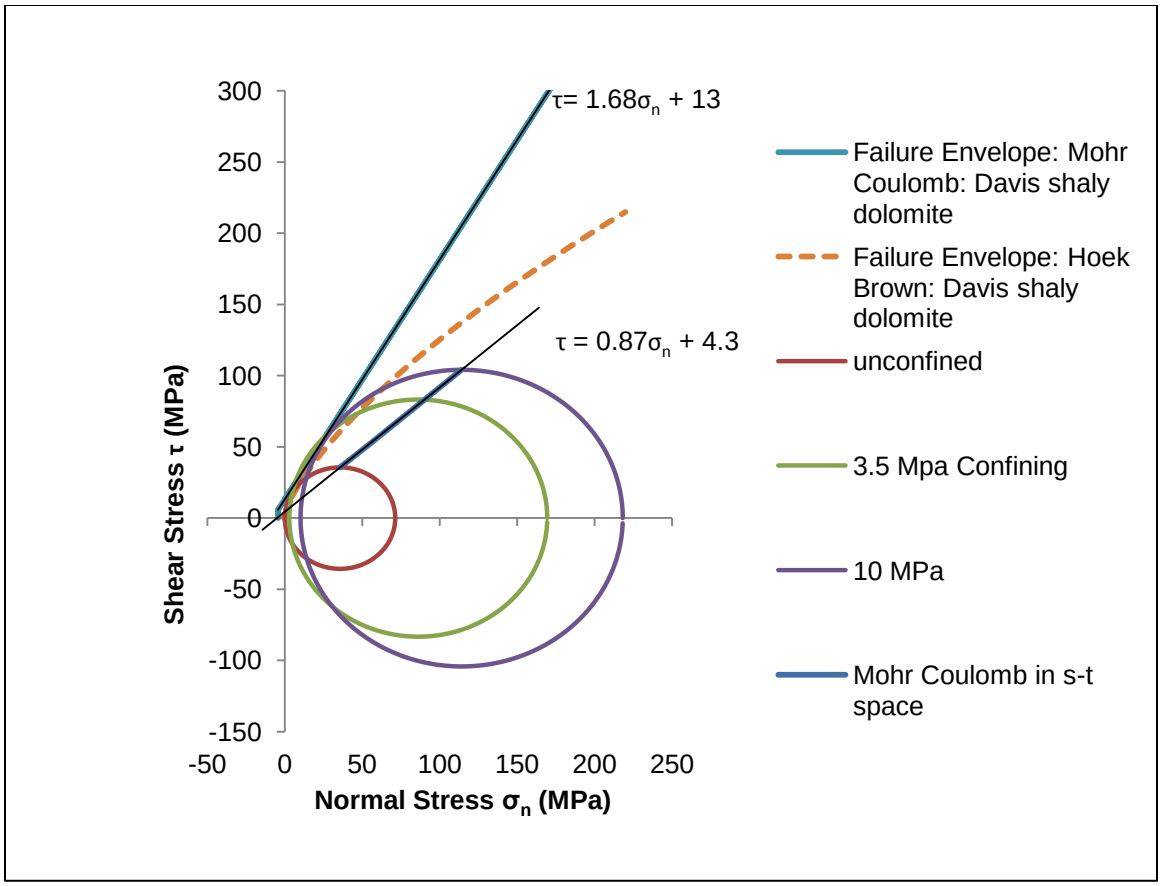

Figure 5.7 Failure envelopes for Davis shaly dolomite, linear Mohr Coulomb, non-linear Hoek Brown and linear Mohr Coulomb in s-t space. Mohr circles have been plotted for unconfined, in-situ and 10 MPa confining stress values. Equations for the linear Mohr Coulomb and Mohr Coulomb in s-t space has been shown

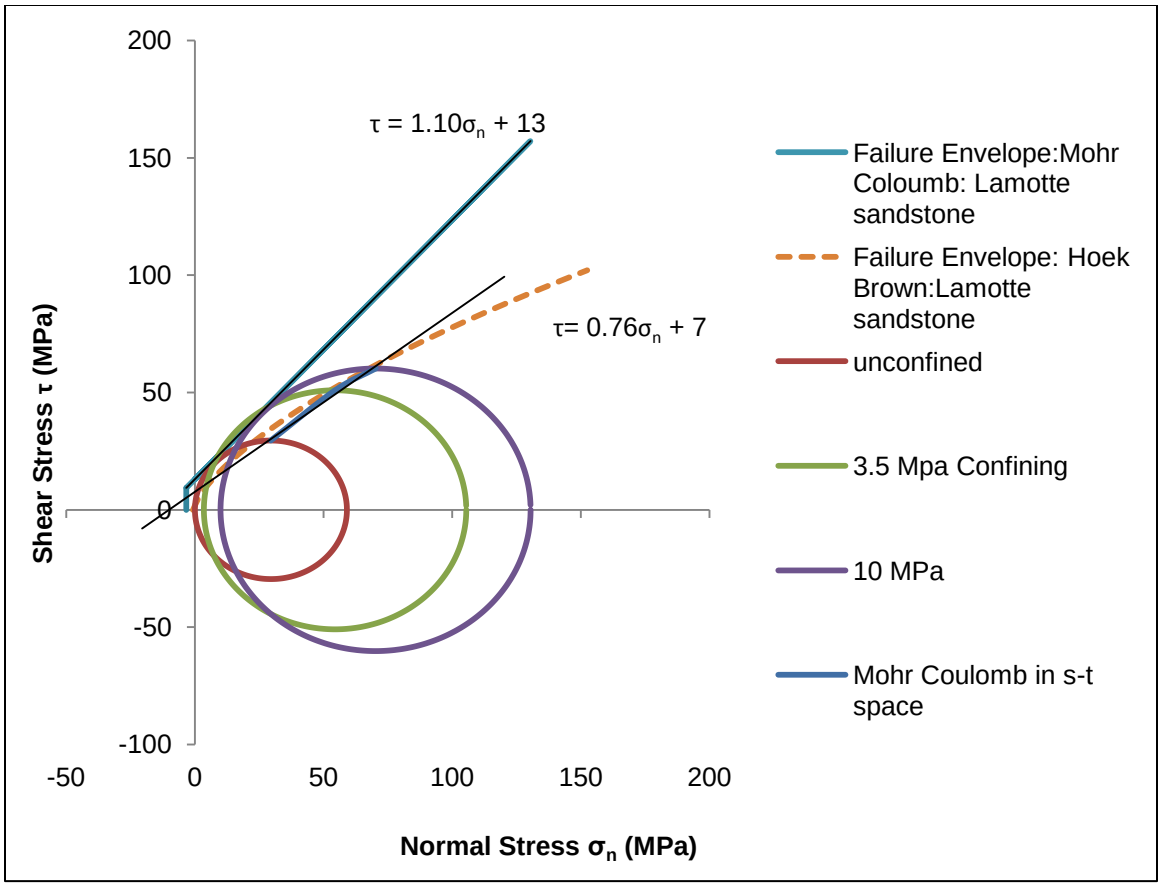

Figure 5.8 Failure envelopes for Lamotte sandstone, linear Mohr Coulomb, non-linear Hoek Brown and linear Mohr Coulomb in s-t space. Mohr circles have been plotted for unconfined, in-situ and 10 MPa confining stress values. Equations for the linear Mohr Coulomb and Mohr Coulomb in s-t space has been shown

5.2.2. Rock Strength And Sonic Properties Correlations. There is a need to calibrate the dynamic properties obtained from sonic tests against static datasets. This is because the actual rock deformation or failure is a relatively slow process but the sonic test is a high frequency wave propagation phenomenon. In the static triaxial tests the sample will experience permanent deformation which is not the case with the sonic tests. The U.C.S obtained from the triaxial lab tests were plotted against the sonic travel time of each rock type obtained from the lab sonic tests and are shown in Figure 5.9. The U.C.S against dynamic and static elastic moduli are shown in Figure 5.10 and Figure 5.11. A co-relation between dynamic and static elastic moduli has been obtained for two of the rock

formations i.e. Bonne Terre dolomite and Lamotte sandstone. These are shown in Figure 5.12 along with comparison with data found in literature (Mockovciakova et al., 2003), (Mohammed et al., 2009), (Nygaard, 2010).

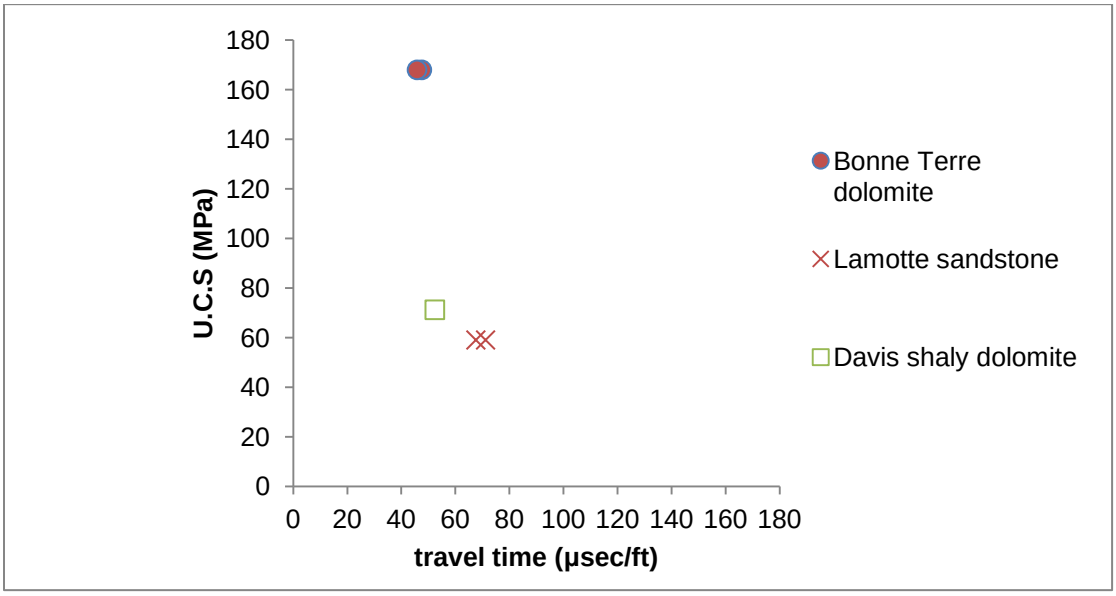

Figure 5.9 U.C.S v/s travel time for Bonne Terre dolomite and Davis shaly dolomite and Lamotte Sandstone

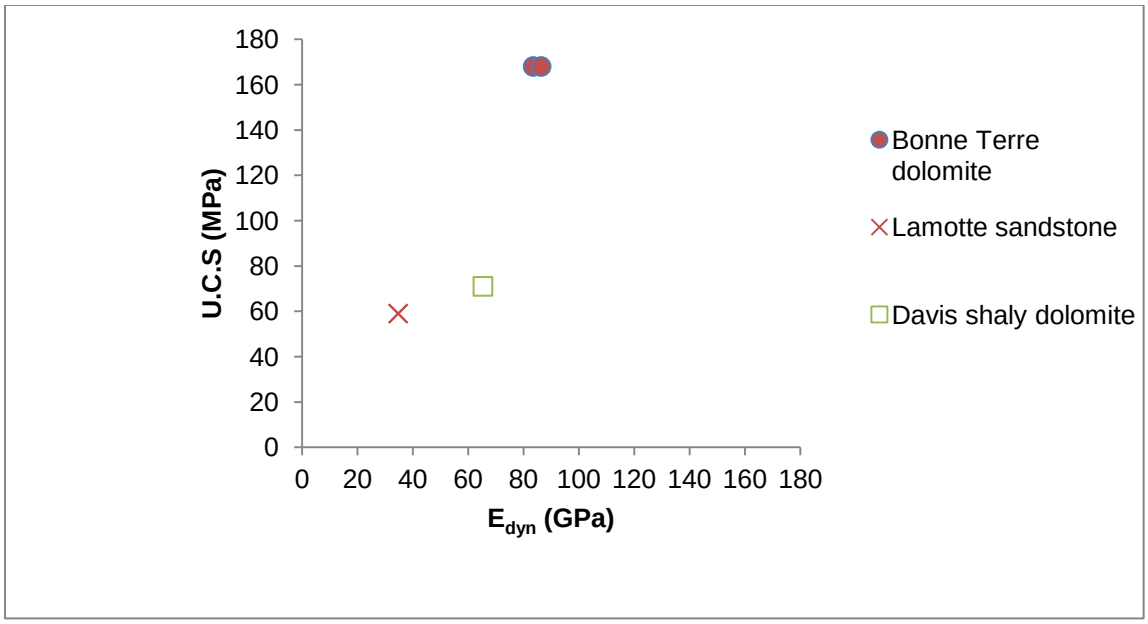

Figure 5.10 U.C.S v/s dynamic elastic modulus

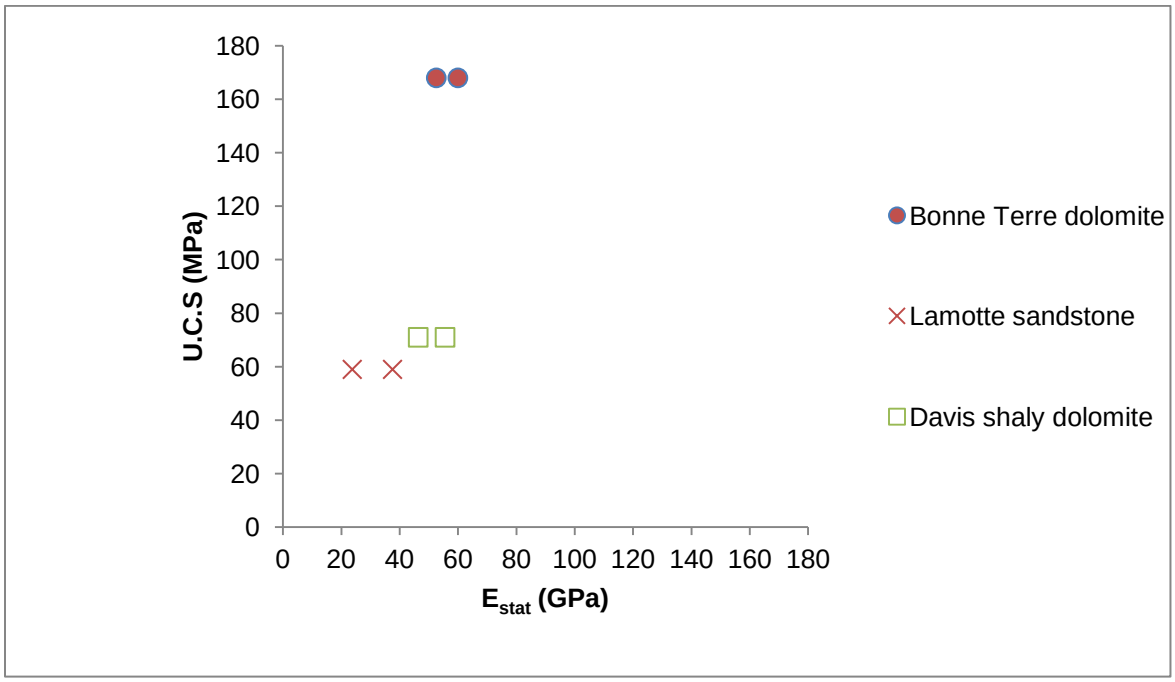

Figure 5.11 U.C.S v/s static elastic modulus

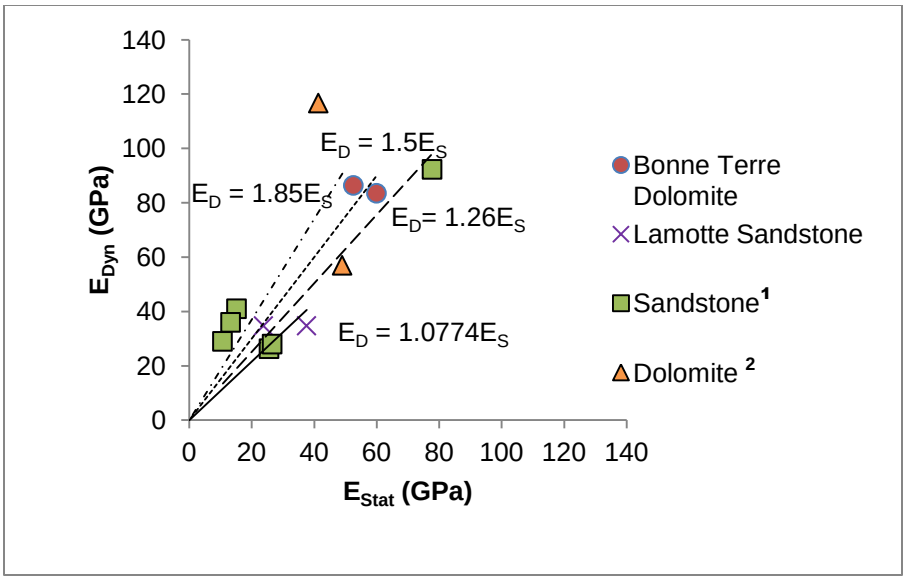

Figure 5.12 Comparison of dynamic Young's moduli based on lab sonic tests on core v/s static moduli from lab triaxial tests of project samples with data found in literature. Sandstone[1] comprises information about the Vitaz, Tvarozec, Pribram, Glauc, Manville and Ellerslie sandstones. Dolomite[2] comprises information about the Arab and Mutnik dolomites.

5.2.3. In-situ State Of Stress. The in-situ state of stress was plotted onto the failure envelopes to provide guidelines for determining the maximum injection pressures and sustainable pressure windows as seen in Figure 5.13, Figure 5.14 and Figure 5.15. The stress states were effective stress regimes calculated for the formation tops and bottoms. The pore pressures at which the formations might undergo tensile failure are shown in Table 5-6. The calculation method used is shown in Appendix D.

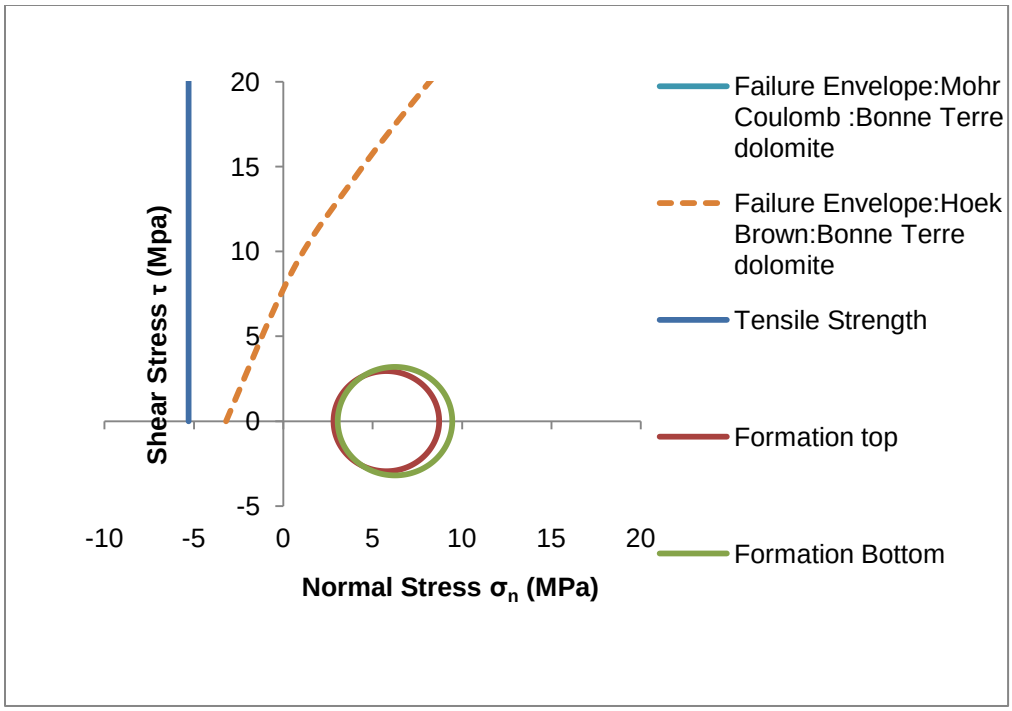

Figure 5.13 Failure scenario evaluation Bonne Terre dolomite

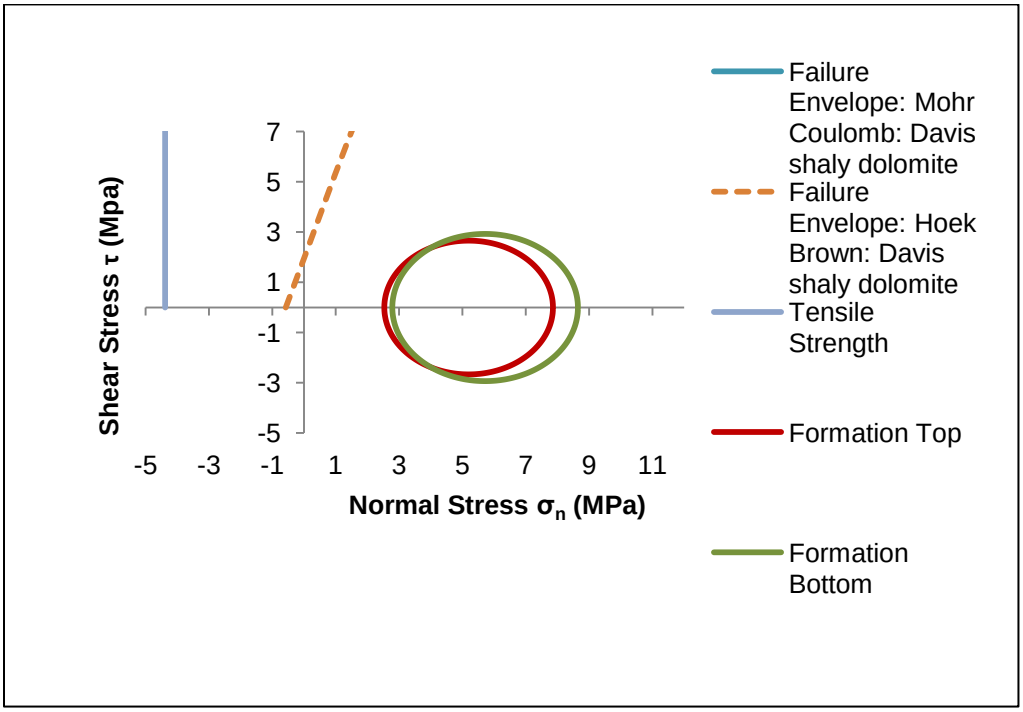

Figure 5.14 Failure scenario evaluation Davis shaly dolomite

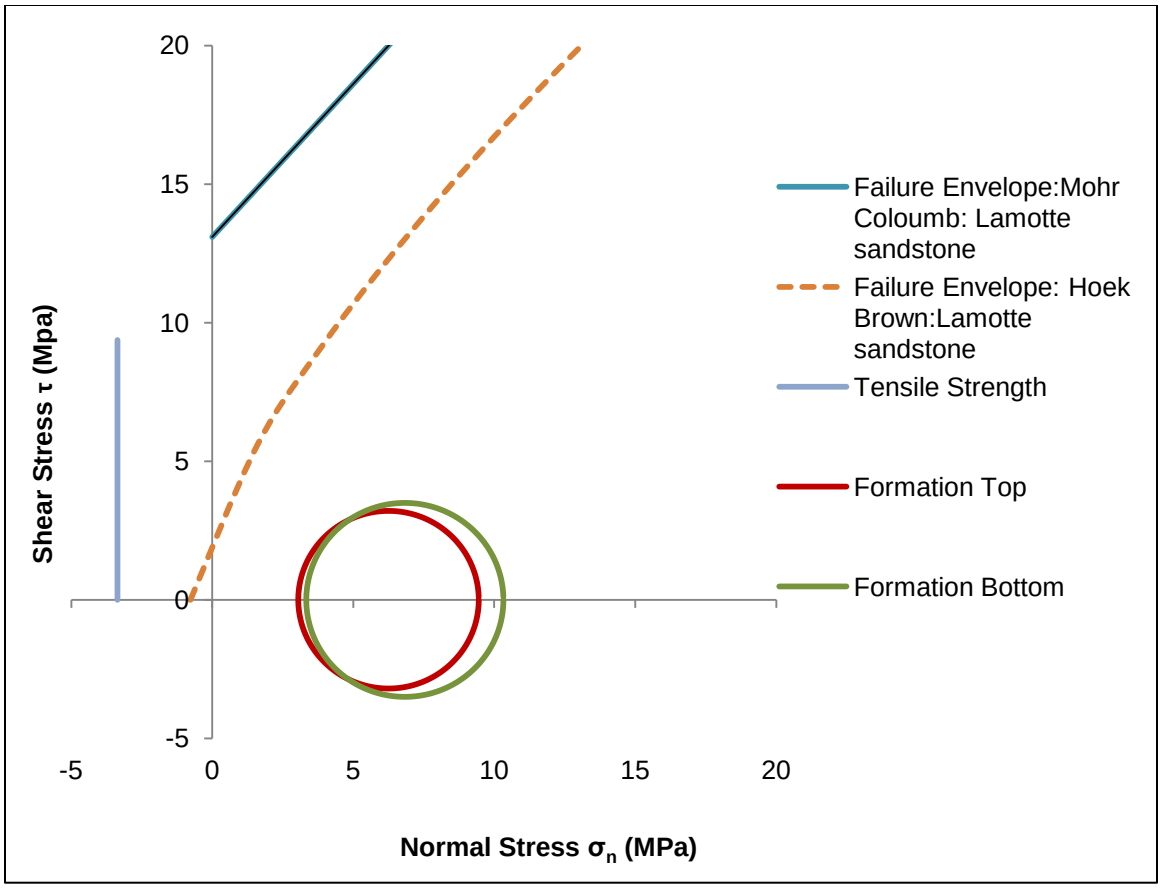

Figure 5.15 Failure scenario evaluation Lamotte sandstone

Table 5-6 Sustainable pore pressure (Pp) window

Formation	Lithology	In-situ Max Pp (MPa)	Pp at tensile failure (MPa)	Pp window (MPa)
Lamotte	Sandstone	5.84	11.69	5.84
Bonne Terre	Dolomite	5.24	12.83	7.59
Davis	Shaly Dolomite	4.66	11.04	6.38

5.3. DISCUSSION

5.3.1. Comparison Of Deformation Properties. The deformation properties include the elastic modulus, shear modulus, bulk modulus and the Poisson's ratio. The values plotted are the averaged values from the datasets shown in Table 5-1 and Table 5-3 as well as from the results of in-situ sonic logs from Akpan (2012). In most cases the lab test values are just near or lower than the sonic test values. The lab sonic tests were interpreted in two ways resulting in very different results. Table 5-2 and Table 5-3 show the deformation properties calculated using the first valley reference point and the trigger reference point. It is seen that using the first valley reference points gives a more accurate representation as the dynamic values thus calculated are higher than the static values. When the first valley reference point is used it results in the dynamic and static values being almost equal or in higher static values which is not an accurate representation. Figure 5.16 to Figure 5.19 show the comparison of the deformation property values obtained from different methods. It can be seen from Figure 5.16 that the values of elastic modulus are similar between the lab triaxial and in-situ sonic but the lab sonic returns higher values for the Bonne Terre and the Davis. The in-situ returns the highest value for the Lamotte. The averaged triaxial test bulk modulus of the Bonne Terre exceeds that of the average obtained in-situ but is less than the lab sonic values as seen in Figure 5.17. In the case of the bulk modulus of the Davis, it is just above the lab sonic value but much higher than the in-situ average while in the case of the Lamotte the in-situ is the highest followed by the lab triaxial and then the lab sonic generated bulk modulus. The shear modulus values obtained from the triaxial test are lower than that obtained from both the sonic tests as shown in Figure 5.18. The averaged Poisson's ratio values from the triaxial test are just above or near the values obtained from the sonic tests except in the case of Lamotte wherein the value is much higher. Poisson's ratio values are plotted in Figure 5.19.

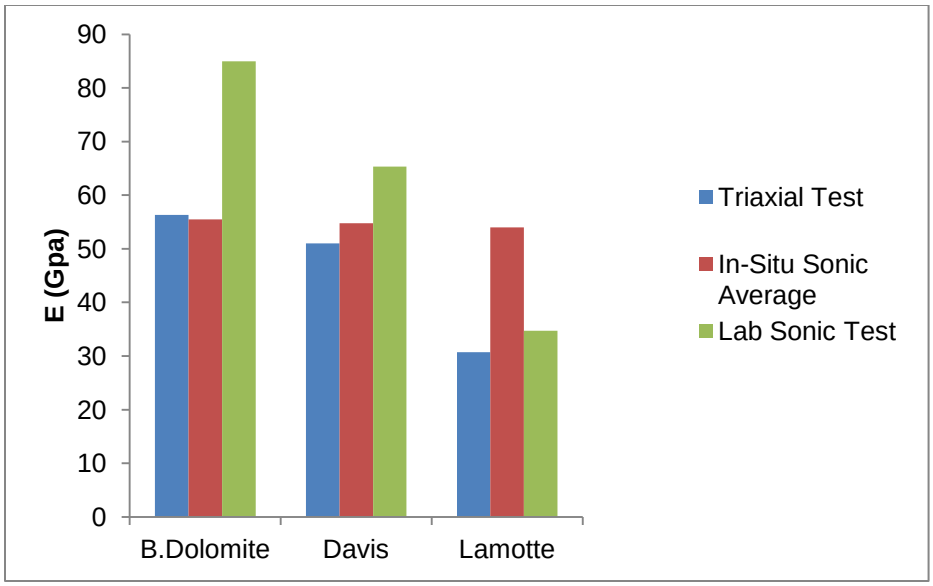

Figure 5.16 Comparison of averaged elastic moduli values for different rocks obtained from the three methods – lab triaxial, in-situ sonic and lab sonic

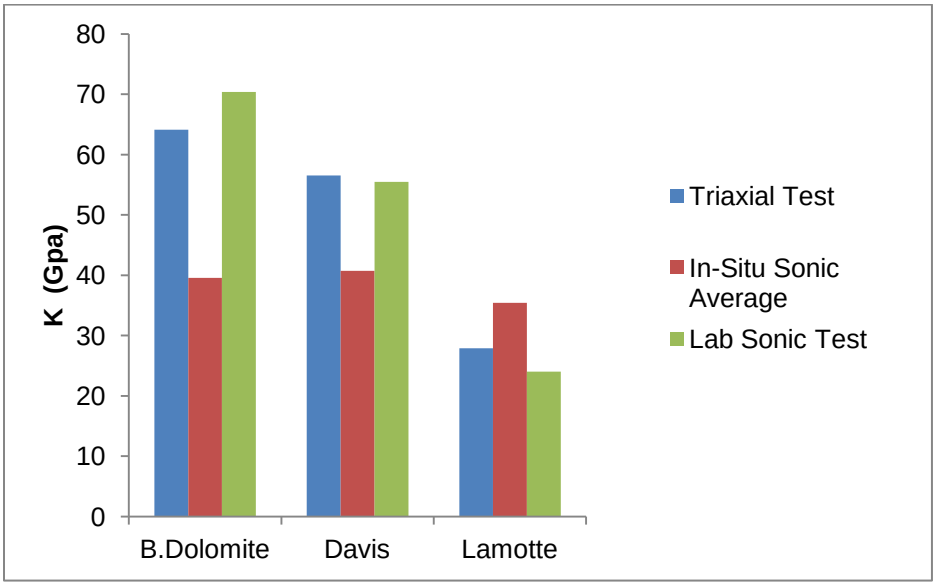

Figure 5.17 Comparison of averaged bulk moduli values for different rocks obtained from the three methods – lab triaxial, in-situ sonic and lab sonic

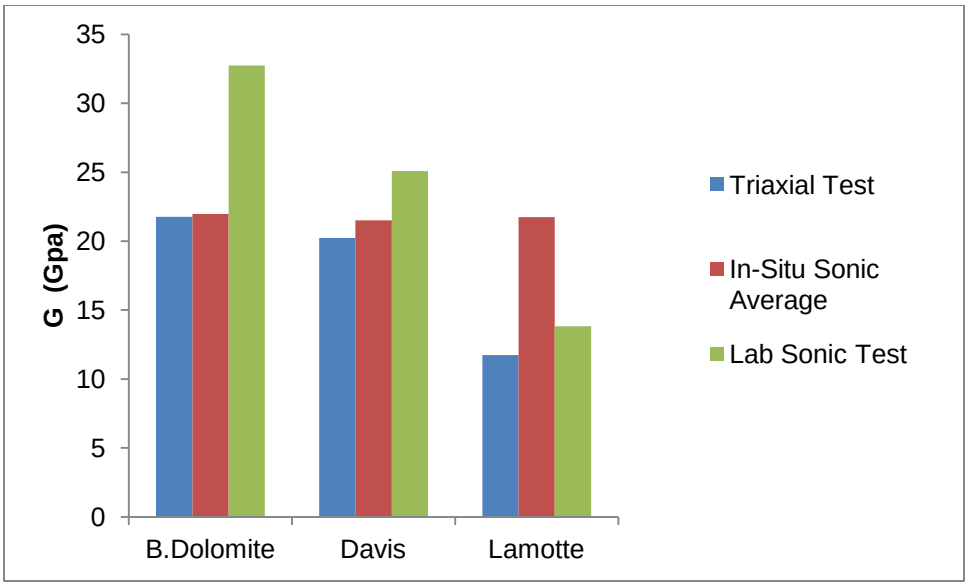

Figure 5.18 Comparison of averaged shear moduli values for different rocks obtained from the three methods – lab triaxial, in-situ sonic and lab sonic

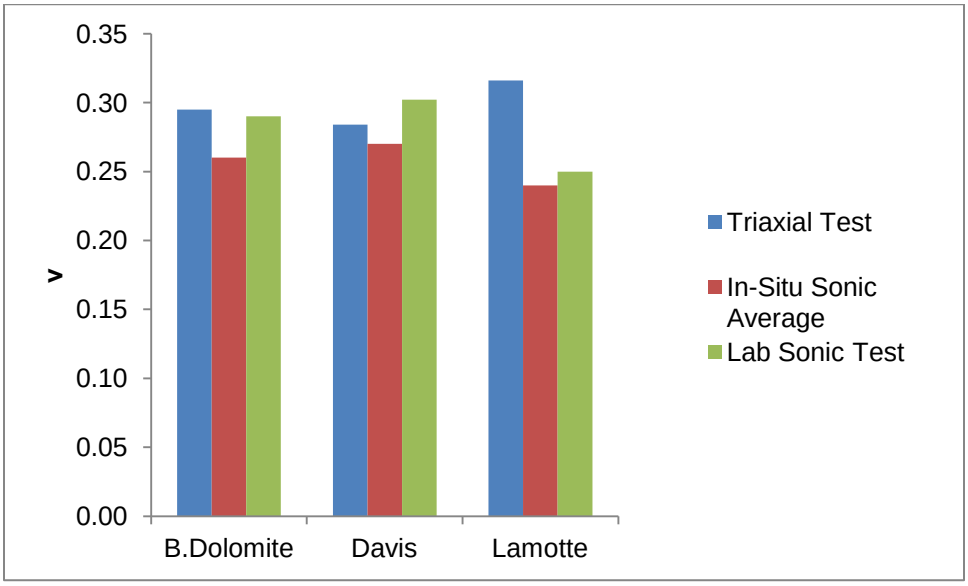

Figure 5.19 Comparison of averaged Poisson's ratio values for different rocks obtained from the three methods – lab triaxial, in-situ sonic and lab sonic

The deformation property values obtained from the triaxial test should ideally be lower than the laboratory sonic data. The instances of the triaxially obtained values being higher than the lab sonic value could be attributed to inherent instrument sensitivity and error as well as the fact that the laboratory sonic tests were carried out under unconfined compressive conditions whereas the triaxial tests were carried out under in-situ and 10 MPa confining pressure conditions.

5.3.2. Comparison Of Failure Envelopes. Two failure criteria were used to predict the failure envelope of the rocks i.e. the Mohr Coulomb and the Hoek Brown criteria. The slope and intercept from the σ_1-σ_3 plots shown from Figure 5.3 to Figure 5.5 serve as inputs for the generation of the Mohr Coulomb failure envelope. The parameters shown in Table 5-4 are inserted into Equation 25 to get the linear Mohr Coulomb failure envelope. Using the σ_1-σ_3 values Mohr circles are generated for the unconfined, in-situ and 10 MPa confining cases and plotted under the Mohr Coulomb failure envelope which was found to be a good fit, for all 3 rock types. The Mohr Coulomb in s-t space is obtained when the line passing through the points corresponding to maximum shear stresses on the Mohr circles is drawn. The Hoek Brown is a non linear failure envelope which diverges from the traditional linear Mohr Coulomb envelope but can be compared with the modified Mohr Coulomb in s-t space envelope. The Hoek Brown and the Mohr Coulomb in s-t space give a conservative estimate of the failure envelope when compared with the linear Mohr Coulomb which reflects actual failure points. Although this may increase the safety factor but it also reduces the injectable amount of CO_2 for fear of potential rock failure creating leakage paths. The Hoek Brown and Mohr Coulomb in s-t space both are revealed to be conservative estimates of rock failure as seen in Figure 5.6 to Figure 5.8. In the case of both Figure 5.6 and Figure 5.8 it can be seen that the Hoek Brown fits very well with the Mohr Coulomb in s-t space as well as with the Mohr circles assuming that a conservative estimate of rock failure is desirable. In the case of Figure 5.7 it is seen that the Hoek Brown fits the data but lies between the Mohr Coulomb in s-t space and the linear Mohr Coulomb thus revealing a gradation in the level of conservative estimation. The linear Mohr Coulomb can be taken to represent actual failure scenario, while the Hoek Brown provides a safety margin, whereas the Mohr

Coloumb in s-t space provides the maximum safety margin amongst the three criteria. It is seen from Table 5-4 that the U.C.S values obtained from the Mohr Coulomb and from the Hoek Brown methods match while the φ and S_o values tend to be close but do not match. This is an expected deviance as the φ and S_o values are obtained by fitting an average linear relationship to the non-linear Hoek Brown envelope over a range of minor principal stresses defined by $\sigma_t < \sigma_3 < \sigma_{3max}$. The value of σ_{3max} over which this relationship between the criteria is considered has to be determined for each individual case (Hoek et al., 2007).

5.3.3. Rock Strength And Sonic Properties Relations. The U.CS obtained from the triaxial lab tests were plotted against the sonic travel time of each rock type and also compared with the data summarized by Chang et al., (2006). The general trend of a decrease in the U.C.S with increase in travel time is observed (Figure 5.9). The data also falls within the range of values reported by various researchers (Chang et al., 2006) (Figure 5.20, Figure 5.21). Figure 5.10 and Figure 5.11 shows that U.C.S increases with increase in dynamic elastic modulus as well static elastic modulus. Figure 5.12 shows the relation between the dynamic and static elastic moduli for Bonne Terre dolomite and Lamotte sandstone. In both cases the static moduli are lower than the dynamic moduli. The dynamic moduli are 1.5 times the static value for the Bonne Terre while for the Lamotte it is 1.07 times the static value.

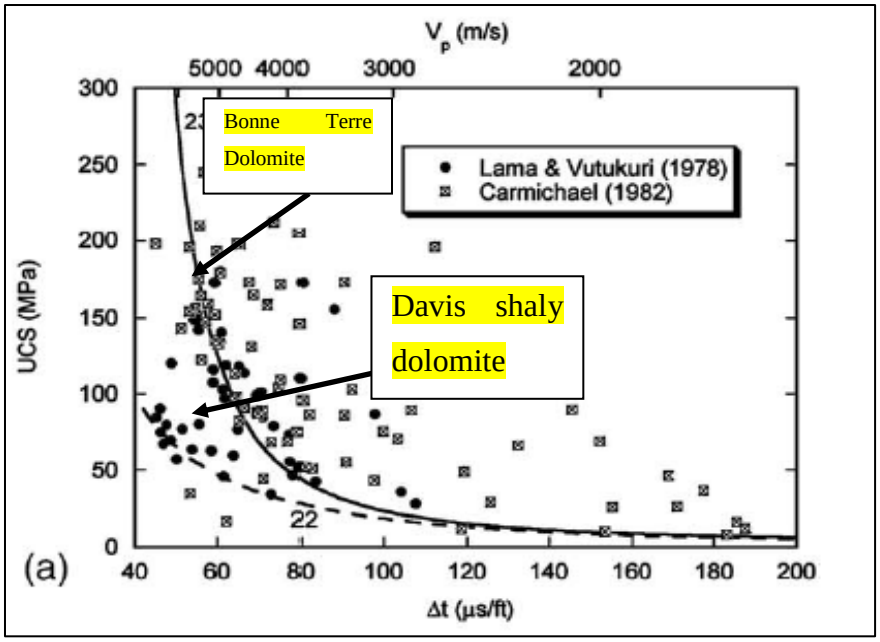

Figure 5.20 U.C.S v/s travel time and P-velocity for limestones and dolomites (Chang et al., 2006)

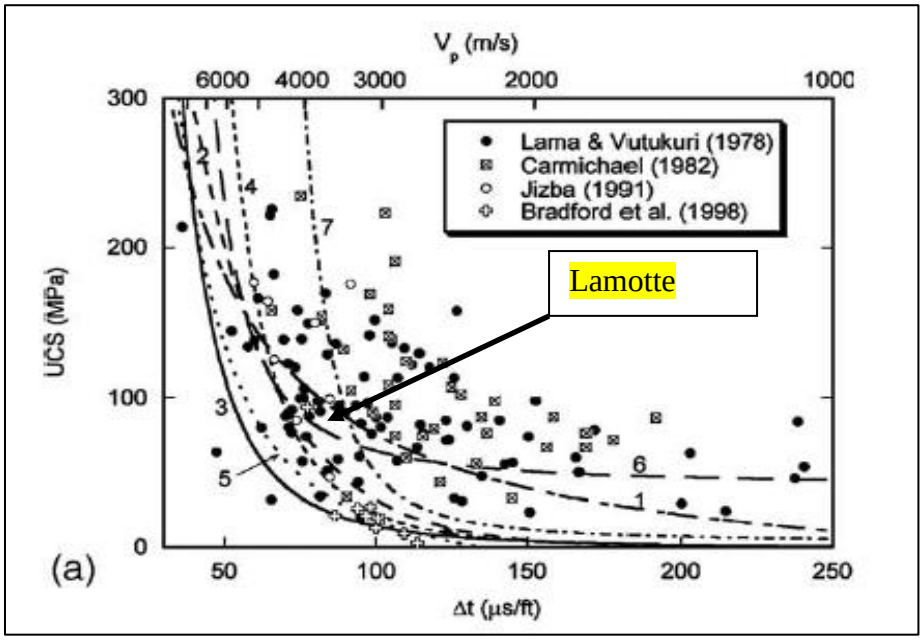

Figure 5.21 U.C.S v/s travel time and P-velocity for Sandstones (Chang et al., 2006)

5.3.4. Implications On CO_2 Sequestration. The in-situ stress plotted onto the failure envelopes from Figure 5.13 to Figure 5.15 help in deciding the maximum injection pressures. The results are not taking into consideration the changes in the properties of the rocks over long term storage duration and the effect that CO_2 has on the rock properties or any existing fractures in the reservoir and the cap rock. The formations overlay each other starting with Lamotte at the bottom, Bonne Terre in the middle and Davis on the top followed by other formations. The increase in depth is visible as the effective stress mohr circles are larger for each formation corresponding to the formations depth. Thus Lamotte has the maximum effective stresses acting on it. Injection of CO_2 will lead to eventual increase in pore pressure even if it is accompanied by brine removal. This increase in pore pressure at the shallow depths under consideration will lead to a reduction in stress leading to the Mohr circles moving closer to the failure envelopes. It is seen from Figure 5.13 to Figure 5.15 that the chances of tensile failure occurring are much higher than the chances of shear failure. The Lamotte sandstone is the reservoir rock and the Davis shaly dolomite is the cap rock. From the results of the uniaxial tests it is seen that both the capping Davis and the Bonne Terre which serves as a partial seal have higher strengths then the reservoir Lamotte, injection induced pore pressure increase is more likely to cause failure in the reservoir rock first and if the injection pressure is kept between the strengths of the Davis and the Lamotte then sealing could still be ensured. From the results of the initial laboratory Brazilian tensile tests the reservoir rock has the lowest tensile strength, it will be subject to fracturing before the sealing rock, and keeping within the 1 MPa difference in tensile strength of Lamotte and Davis will ensure seal integrity as the strength of the intermediate Bonne Terre is much higher. On comparison between the failure envelope charts it is seen that since the Lamotte formation is subject to higher stresses and since it has lower tensile strength than the other formations it is likely to undergo tensile failure before the others. This is desirable as it means ease and increase of access to the reservoir. From the Table 5-6 it can be seen that the safe pore pressure to aim at would be 10 MPa. Although tensile failure within the reservoir is desirable but the combination of insitu minimum horizontal stress and existing pore pressure have made the Davis formation weaker than the Lamotte, making it a necessity to keep the pore pressure a bit lower than that of the reservoir tensile failure

value. The Bonne Terre formation has a much higher value of sustainable pore pressure and hence could act as a good barrier and partial reservoir.

6. CONCLUSIONS

The Lamotte sandstone formation and the part of the Bonne Terre dolomite formation have porosity and permeability which makes them a potential CO_2 sequestration site. The Upper Bonne Terre and the Davis shale rich formation have low permeability which makes them suitable formations which function as a seal. To evaluate the sedimentary succession of Missouri for potential geological sequestration of CO_2 as a climate mitigation tool, rock mechanical testing has to be conducted for determining seal integrity. The evaluated rock properties could also serve as inputs for the simulation of geological sequestration of CO_2.

To perform these analyses, this study developed a testing apparatus for conducting rock mechanical tests including Brazilian, uniaxial and drained triaxial tests. The developed test set up can automatically collect data of rock properties like vertical and horizontal stress and strain data as also sonic p and s wave velocities to characterize 1.5 inch diameter rocks specimen.

Two kinds of failure criteria – Mohr Coulomb & Hoek Brown were applied to fit the experimental data and were found acceptable. The Hoek Brown was found to give a conservative envelope as compared to the linear Mohr Coulomb envelope. The U.C.S values from both the criteria were differing by 0.5% for Bonne Terre dolomite, by 5.7% for Lamotte and 14.2% for Davis. The Mohr Coulomb parameters evaluated from the Hoek Brown curve were differing from the values obtained from Mohr Coulomb calculations. This was deemed acceptable as the Hoek Brown is a non linear curve from which the linear parameters were interpolated. The deformation properties obtained from the triaxial test were compared with the lab sonic and in-situ values and were found to be in the same range. In the instances where the triaxial test values were greater than the sonic values there may have been measurement errors. These errors can be rectified by better shielding of the sensitive measurement apparatus and using better circuitry.

The U.C.S and sonic travel time co-relations generated from the tests were in agreement with the co-relations found in literature for the specific rock type. This validates the assumption that the correlations could be used for estimation of U.C.S when there is limited data or core availability.

The U.C.S for Bonterre Dolomite was found to range from 145 to 200 MPa, that of Davis from 65 to 77 MPa and of Lamotte from 50 to 60 MPa. Given the above ranges, all of the above rocks fall under the hard formation category rather than the classification of soft sedimentary formations. The tensile strength of Lamotte sandstone which is the potential reservoir is the lowest at 3 MPa while that of the partial seal Bonne Terre is highest at 5 MPa.

The rock formations under consideration for CO_2 sequestration were evaluated under intact conditions and found to be very stable under the current in-situ stress conditions. The formations could undergo tensile failure if the increase in pore pressure was higher than the critical value with the reservoir rock undergoing failure before the others.

APPENDIX A
SAMPLE DETAILS

Table A-1 Brazilian Test Sample Details

Sample No/Name	Diameter	Length	L/D	Mass	Volume	Density
	mm	mm		g	mm^3	g/cm3
BDS1	50.8	23.91	0.471	123.8	48475	2.55
BDS2	50.8	23.91	0.471	128	48475	2.64
BDS3	50.8	26.71	0.526	-	54147	0
BDS4	50.8	22.38	0.441	121.2	45380	2.67
BDS5	50.8	25.44	0.501	138.8	51569	2.69
BDS6	50.8	25.94	0.511	142.4	52600	2.70
DS1	50.8	27.47	0.541	134	55694	2.40
DS2	50.8	26.20	0.516	138	53116	2.59
DS3	50.8	24.67	0.486	128.8	50022	2.57
DS4	50.8	24.16	0.476	118.8	48990	2.42
DS5	50.8	24.93	0.491	128.4	50537	2.54
DS6	50.8	24.16	0.476	125	48990	2.55
SS1	50.8	26.03	0.512	111	52769	2.10
SS2	50.8	25.44	0.501	115.8	51569	2.24
SS3	50.8	24.42	0.481	110.6	49506	2.23
SS4	50.8	23.65	0.466	103.4	47959	2.15
SS5	50.8	26.20	0.516	116	53116	2.18
SS6	50.8	25.94	0.511	117.8	52600	2.23

Table A-2 Uniaxial Sample Details

Sample No/Name	Diameter	Length	L/D	Mass	Volume	Density
	in	in		g	mm^3	g/cm3
BD-A	1.5	3.06	2.04	238.6	88640	2.69
BD-B	1.5	3.07	2.04	242.8	88930	2.73
D-A	1.5	3.07	2.04	225.4	88930	2.53
D-B	1.5	3.05	2.03	224.6	88351	2.54
SS-A	1.49	3.11	2.08	194.4	88892	2.18
SS-B	1.5	3.07	2.04	194.4	88930	2.18

Table A-3 Triaxial Sample Details

Sample No/Name	Diameter	Length	L/D	Mass	Volume	Density
	mm	mm		g	mm^3	g/mm^3
D-A	38.1	81	2.13	243.8	92347.4	0.0026
D-B	38.1	78	2.05	233.1	88927.2	0.0026
BD-B	37.34	75.21	2.01	226.8	82359.6	0.0027
BD-A	37.34	79.16	2.12	229	86685.1	0.0026
L-A	38.1	77	2.02	193.9	87787.1	0.0022
L-B	37.34	76	2.03	191.2	83224.7	0.0023

APPENDIX B

TEST RESULTS SUMMARY

Table B-1 Brazilian Test Summary

Test no	Formation	Lithology	Sample No/Name	Loading Relative to Bedding	Failure Load (lb)	Brazilian Tensile Strength MPa
T-001-B	Bonne Terre	Dolomite	BDS1	Parallel	1411	3.28
T-002-B	Bonne Terre	Dolomite	BDS2	Parallel	2577	6.00
T-003-B	Bonne Terre	Dolomite	BDS3	Parallel	-	#######
T-004-B	Bonne Terre	Dolomite	BDS4	Parallel	2294	5.71
T-005-B	Bonne Terre	Dolomite	BDS5	Parallel	2764	6.05
T-006-B	Bonne Terre	Dolomite	BDS6	Parallel	2547	5.47
T-007-B	Davis	Shaly Dolomite	DS1	Parallel	3145	6.37
T-008-B	Davis	Shaly Dolomite	DS2	Parallel	1640	3.48
T-009-B	Davis	Shaly Dolomite	DS3	Parallel	1625	3.67
T-010-B	Davis	Shaly Dolomite	DS4	Parallel	1490	3.43
T-011-B	Davis	Shaly Dolomite	DS5	Parallel	2129	4.75
T-012-B	Davis	Shaly Dolomite	DS6	Parallel	2019	4.65
T-013-B	Lamotte	Sandstone	SS1	Parallel	701	1.50
T-014-B	Lamotte	Sandstone	SS2	Parallel	2174	4.76
T-015-B	Lamotte	Sandstone	SS3	Parallel	1181	2.69
T-016-B	Lamotte	Sandstone	SS4	Parallel	1555	3.66
T-017-B	Lamotte	Sandstone	SS5	Parallel	1589	3.37
T-018-B	Lamotte	Sandstone	SS6	Parallel	1955	4.19

Table B-2: Uniaxial Test Summary

Test no	Formation	Lithology	Sample No/Name	Loading Relative to Bedding	Load at Failure	UCS
					Lb	MPa
T-004-U	Bonne Terre	Dolomite	BD-A	Perpendicular	37597	146.69
T-005-U	Bonne Terre	Dolomite	BD-B	Perpendicular	48707	190.03
T-005-U	Davis	Shaly Dolomite	D-A	Perpendicular	19927	77.74
T-006-U	Davis	Shaly Dolomite	D-B	Perpendicular	16590	64.72
T-007-U	Lamotte	Sandstone	SS-A	Perpendicular	15383	60.82
T-008-U	Lamotte	Sandstone	SS-B	Perpendicular	14681	57.28

Table B-3 Triaxial Test Details

Test no	Formation	Lithology	Sample No/Name	Loading Relative to Bedding	Horizontal stress start shearing	Vertical stress start shearing	Horizontal stress at failure σ_3	Axial Stress at failure σ_1	E_{50}	v	Cohesion	Internal Angle of Friction	UCS
					MPa	MPa	MPa	MPa	MPa		MPa	°	MPa
T-001-T	Davis	Shaly Dolomite	A	Perpendicular	0.10	0.10	2.9	169.4	55.6	0.16	13.23	59.26	71.2
T-002-T	Davis	Shaly Dolomite	B	Perpendicular	0.10	0.10	10	218.2	46.4	0.41			
T-003-T	Bonne Terre	Dolomite	B	Perpendicular	0.14	0.14	3.1	139	60	0.40	33.17	46.98	168.364
T-004-T	Bonne Terre	Dolomite	A	Perpendicular	0.14	0.14	10	221.9	52.6	0.19			
T-005-T	Lamotte	Sandstone	A	Perpendicular	0.14	0.14	3.5	105.4	23.8	0.36	11.38	47.84	59.053
T-006-T	Lamotte	Sandstone	B	Perpendicular	0.14	0.14	10	130.4	37.6	0.28			

APPENDIX C

STRESS STRAIN CURVES

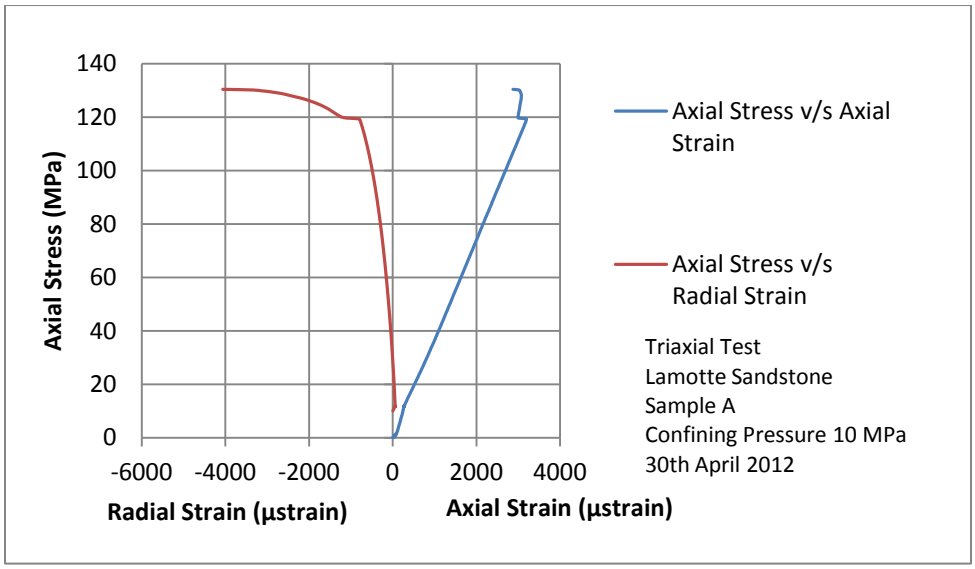
140
120
100
80
60
40
20
0
Axial Stress (MPa)
-6000 -4000 -2000 0 2000 4000
Radial Strain (µstrain)
Axial Strain (µstrain)
Axial Stress v/s Axial Strain
Axial Stress v/s Radial Strain
Triaxial Test
Lamotte Sandstone
Sample A
Confining Pressure 10 MPa
30th April 2012

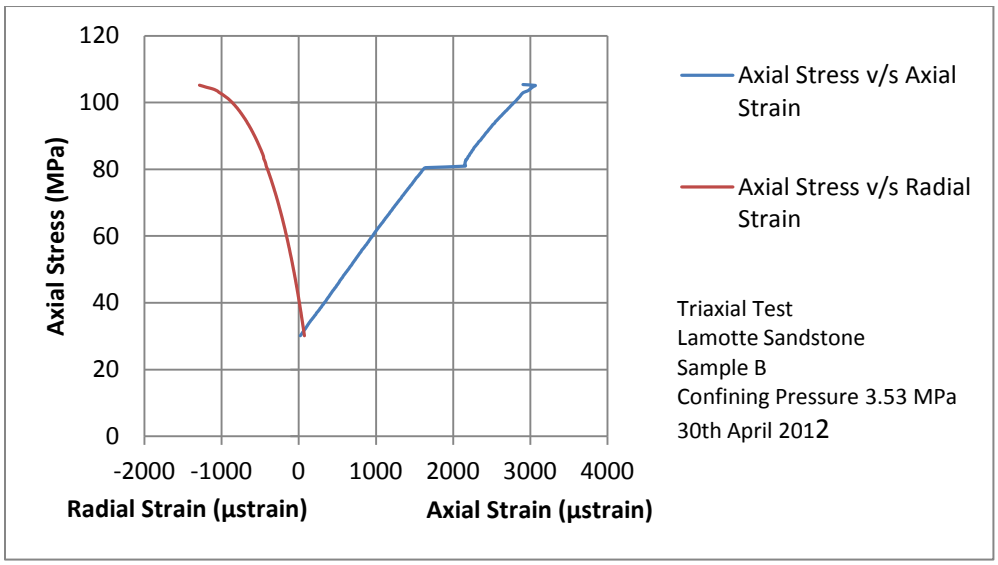
120
100
80
60
40
20
0
Axial Stress (MPa)
-2000 -1000 0 1000 2000 3000 4000
Radial Strain (µstrain)
Axial Strain (µstrain)
Axial Stress v/s Axial Strain
Axial Stress v/s Radial Strain
Triaxial Test
Lamotte Sandstone
Sample B
Confining Pressure 3.53 MPa
30th April 2012

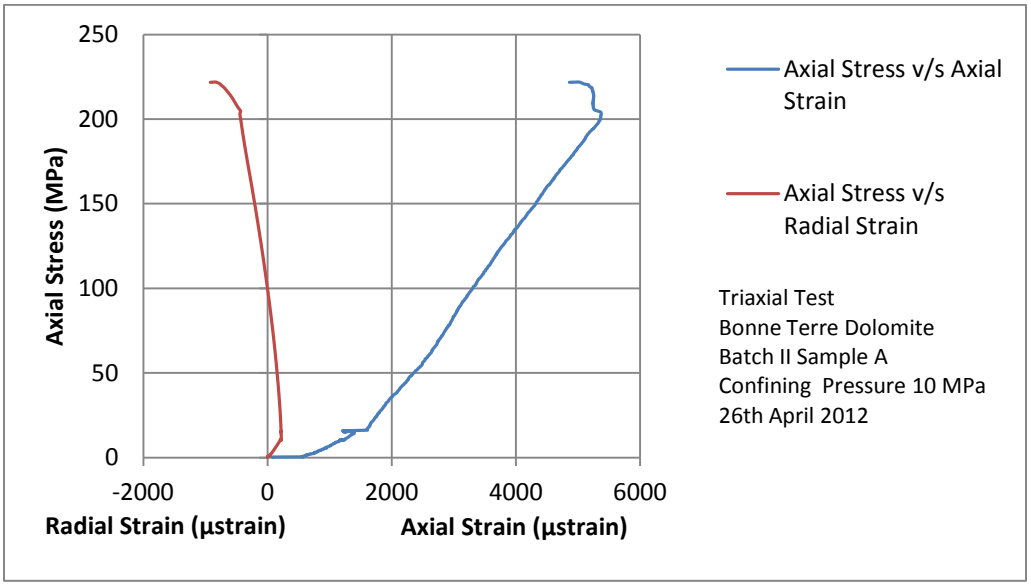
250
200
150
100
50
0
Axial Stress (MPa)
-2000
0
2000
4000
6000
Radial Strain (µstrain)
Axial Strain (µstrain)
Axial Stress v/s Axial Strain
Axial Stress v/s Radial Strain
Triaxial Test
Bonne Terre Dolomite
Batch II Sample A
Confining Pressure 10 MPa
26th April 2012

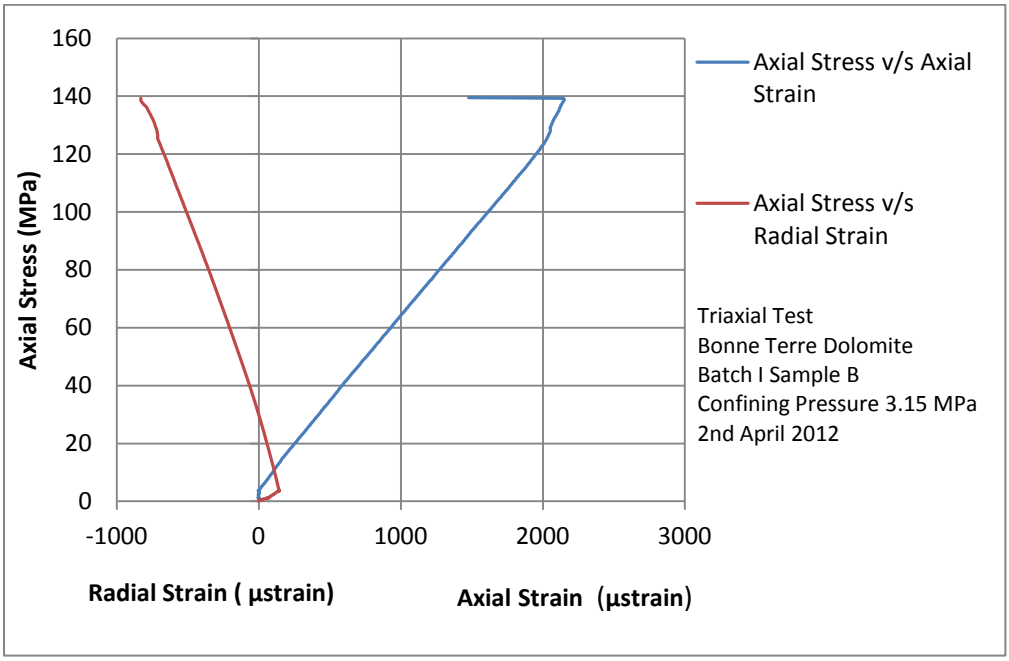
160
140
120
100
80
60
40
20
0
Axial Stress (MPa)
-1000
0
1000
2000
3000
Radial Strain (µstrain)
Axial Strain (µstrain)
Axial Stress v/s Axial Strain
Axial Stress v/s Radial Strain
Triaxial Test
Bonne Terre Dolomite
Batch I Sample B
Confining Pressure 3.15 MPa
2nd April 2012

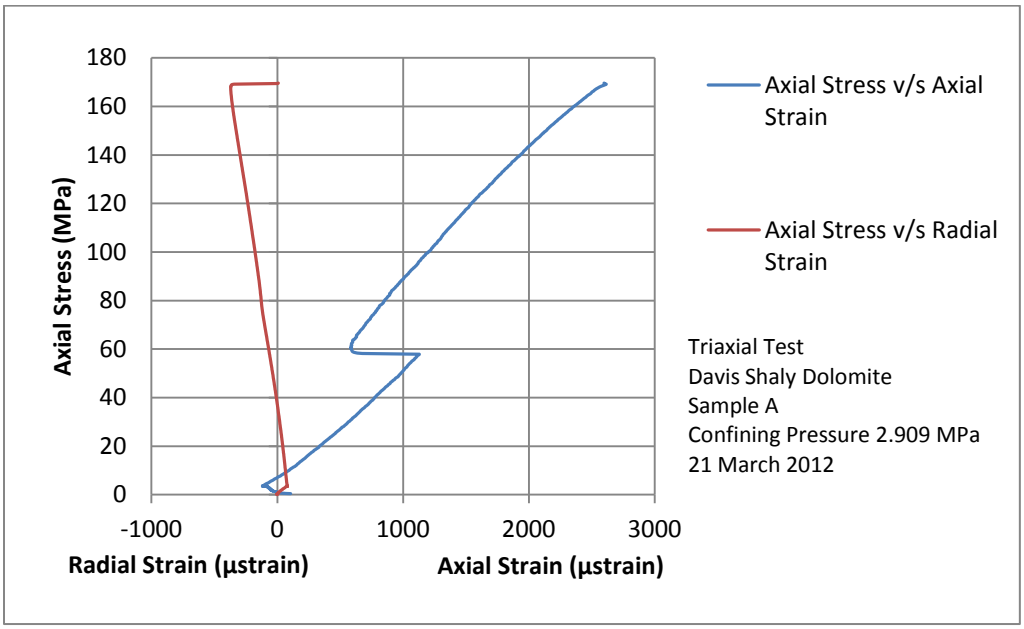
180
160
140
120
100
80
60
40
20
0
Axial Stress (MPa)
-1000
0
1000
2000
3000
Radial Strain (µstrain)
Axial Strain (µstrain)
Axial Stress v/s Axial Strain
Axial Stress v/s Radial Strain
Triaxial Test
Davis Shaly Dolomite
Sample A
Confining Pressure 2.909 MPa
21 March 2012

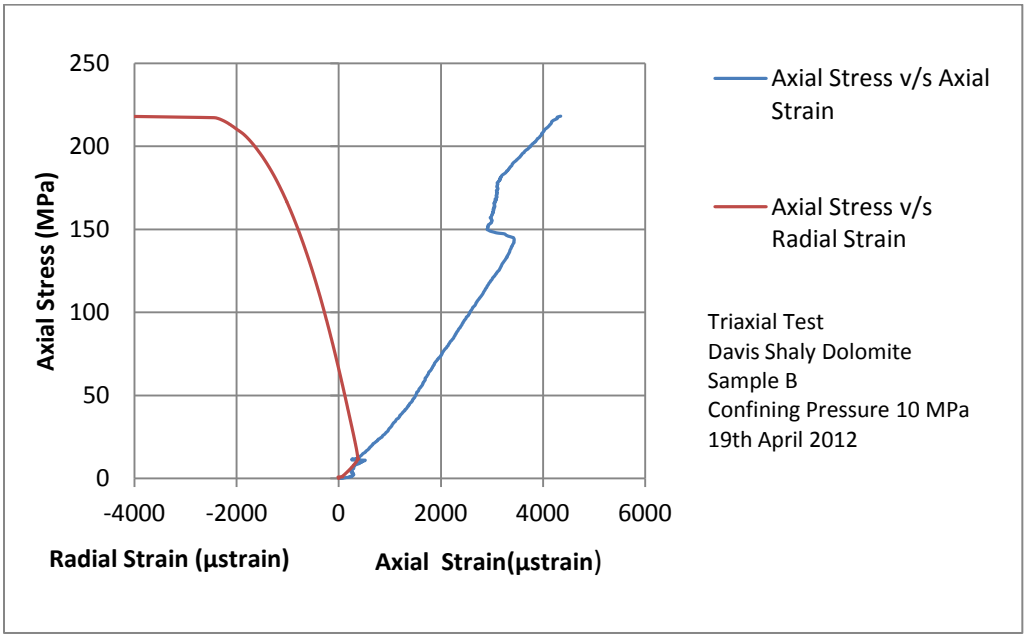
250
200
150
100
50
0
Axial Stress (MPa)
-4000
-2000
0
2000
4000
6000
Radial Strain (µstrain)
Axial Strain(µstrain)
Axial Stress v/s Axial Strain
Axial Stress v/s Radial Strain
Triaxial Test
Davis Shaly Dolomite
Sample B
Confining Pressure 10 MPa
19th April 2012

APPENDIX D

CALCULATION OF PORE PRESSURE CAUSING TENSILE FAILURE

According to Terzaaghi's effective stress principle:

Total Stress = Effective Stress + Pore Pressure

At tensile failure :

Effective stress = $S_h - P_p = \sigma_T$

Then

$$P_{p=} S_{h+} \sigma_T$$

Where *Pp* is pore pressure value causing tensile failure, S_h is minimum horizontal stress and σ_T is the tensile strength of the rock. Extending this to the case of the three rock formations, the minimum values of the minimum horizontal stresses in the formation are known. The maximum value of the pore pressure in the formation can be evaluated by statistical analysis. Combining these with the above Equation gives the desired values of pore pressures which cause tensile failures in the formation.

The complete expression for the calculation of minimum horizontal stress while neglecting tectonic stresses is given as:

$$\sigma_h = \left[\frac{\nu}{1-\nu}\right] \cdot \left(\sigma_V - \alpha \cdot P_P\right) + \alpha \cdot P_P$$

Where ν is the Poisson's ratio, σ_V is the vertical stress or overburden, P_P is the pore pressure, α is the Biot's parameter defined for a poroelastic regime as

$$\alpha = 1 - \left[\frac{K_{SK}}{K_S}\right]$$

Where K_{SK} is bulk modulus of dry skeletal frame of rock, K_S is rock matrix bulk modulus

In our case we assume α to be equal to 1 which implies the assumption that increasing external stress produces same volume change in the porous material as the reducion in pore pressure.

APPENDIX E
LABORATORY TESTING IMAGES

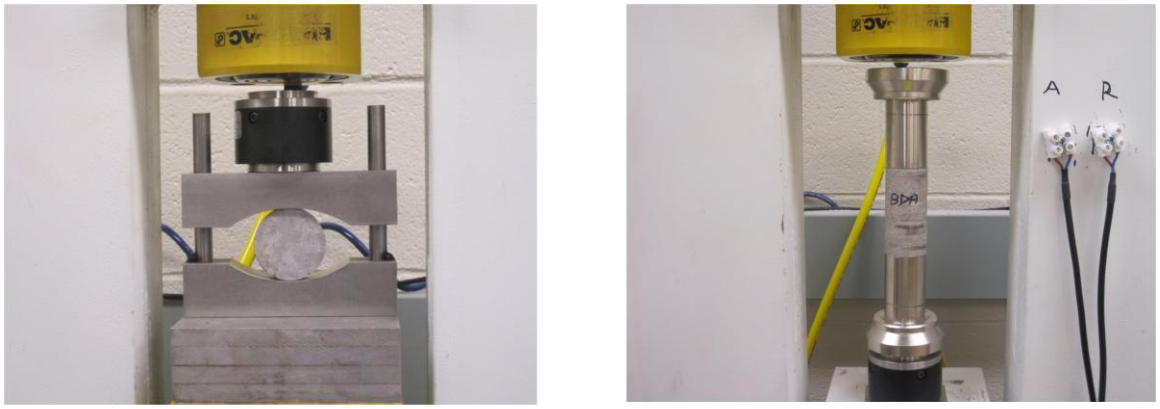

Figure E-1 Images of rock samples mounted onto the rigs for (a) Brazilian testing (b) uniaxial testing

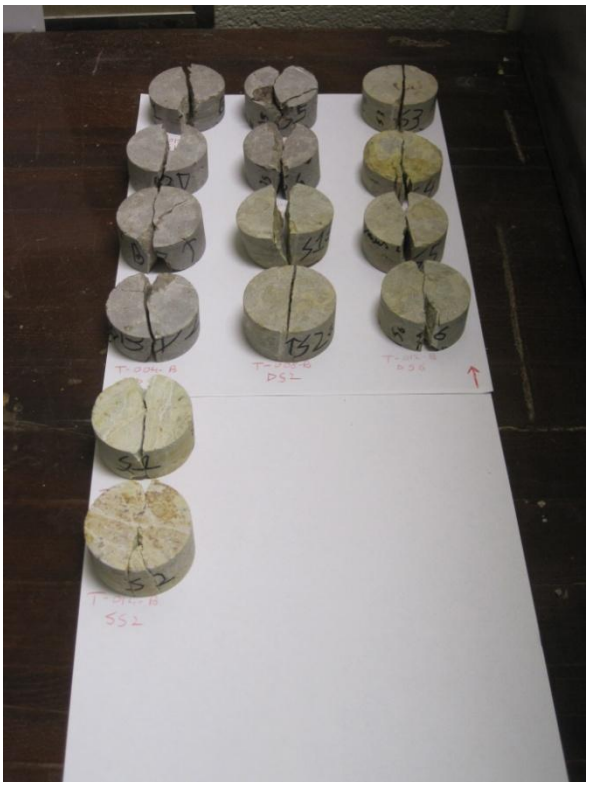

Figure E-2 Images of rock samples after undergoing Brazilian testing

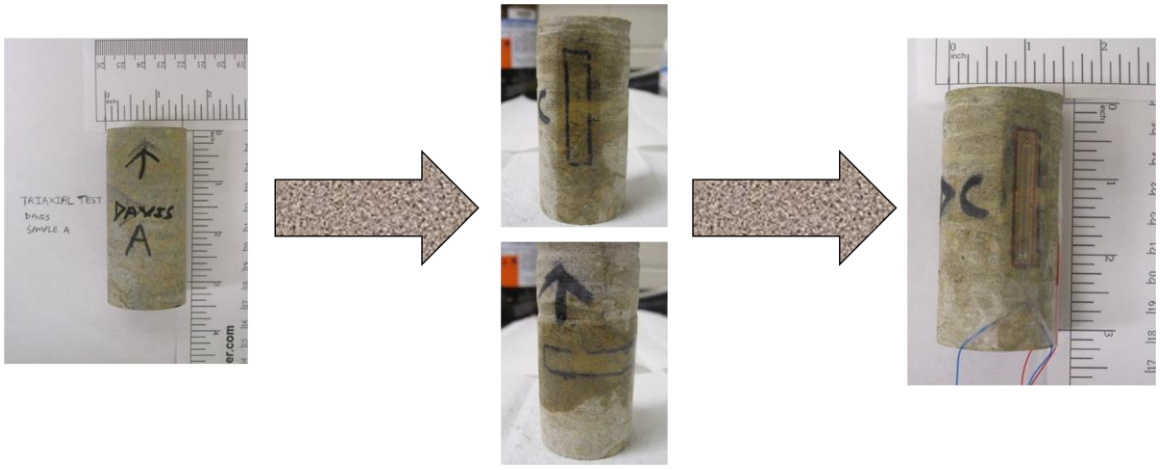

Figure E-3 Images showing strain gauge application procedure

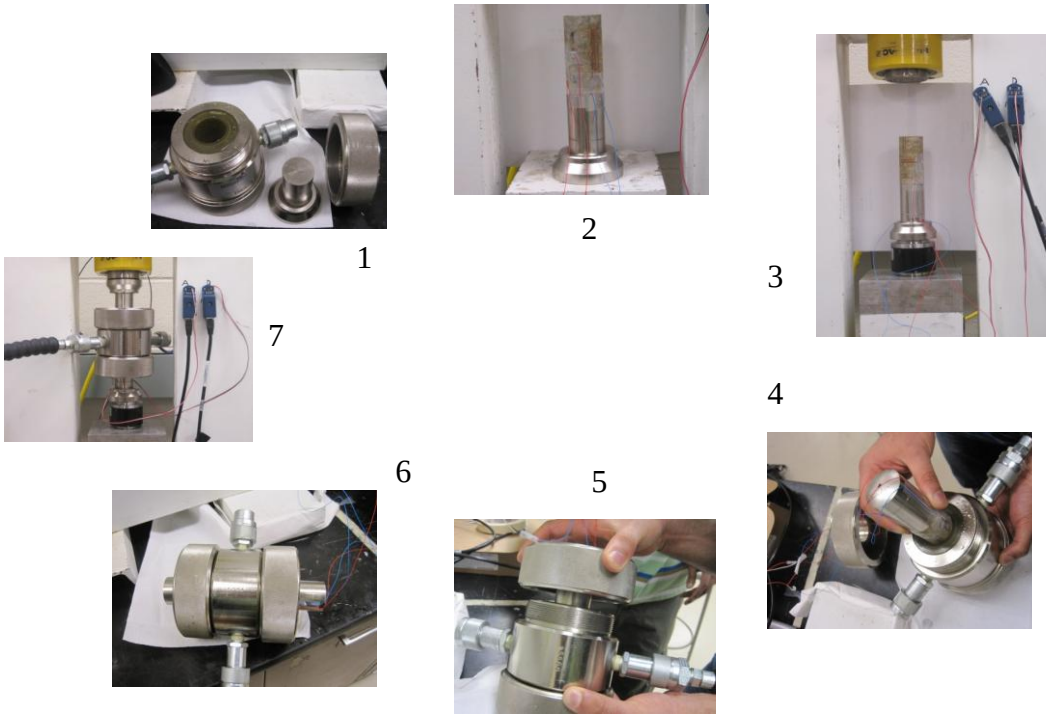

Figure E-4 Images showing the mounting of the sample for triaxial testing. The numbers indicate the steps to be followed.

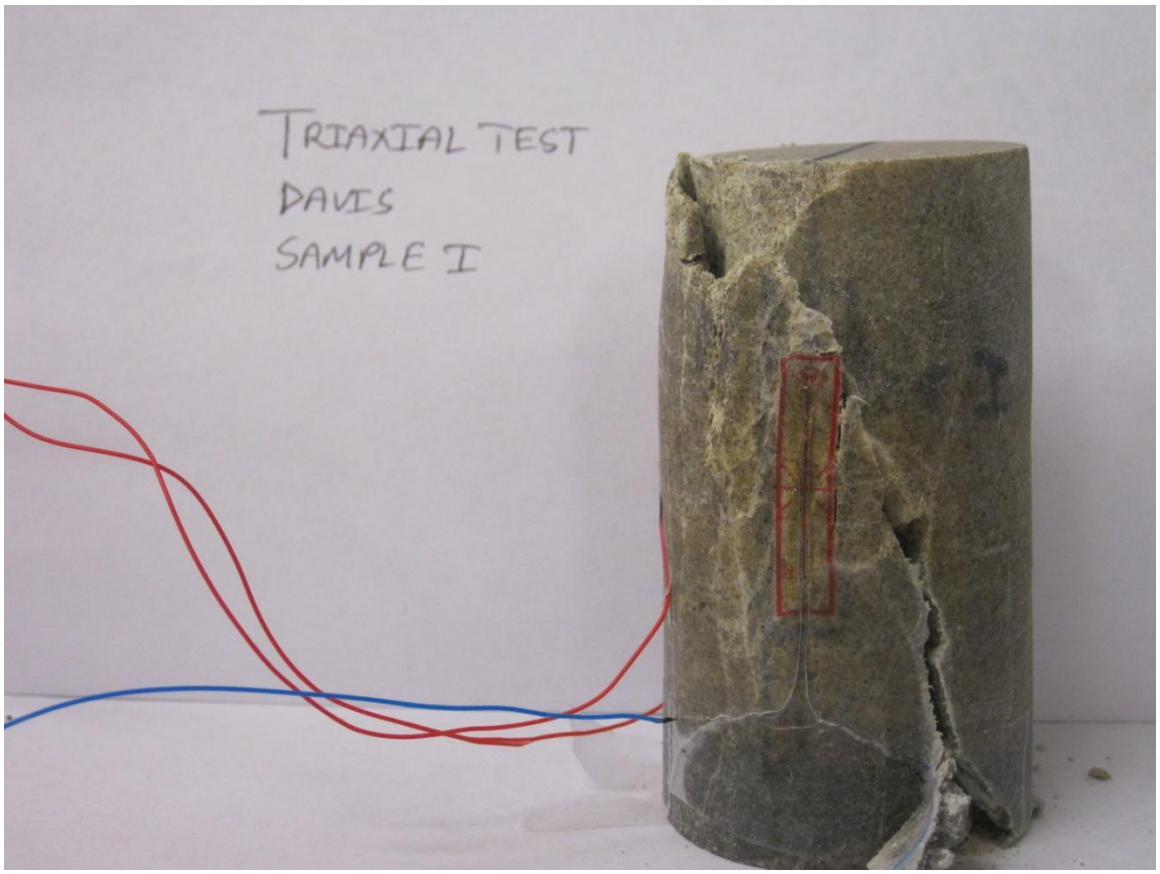

Figure E-5 Images of rock sample after triaxial testing

BIBLIOGRAPHY

ACCAT, 2009, " Accelerating The Deployment of Carbon Abatement Technologies with special focus on carbon capture and storage," Department of Energy and Climate Change, Government of the United Kingdoms.

Akpan I.C., 2012, "Development of a Shared Earth Model To Investigate Potential For Carbon Dioxide Sequsetration In The Springfield Area, MO," M.S. Thesis, Missouri University of Science & Technology, Rolla , Missouri.

Aspelund A., Molnvik M.J., Koeijer.DE.G., 2006, "Ship Transport of CO_2 Technical Solutions and Analysis of costs, energy utilization,energy efficiency and CO_2 Emissions," Trans IChemE Part A, Chemical Engineering Research and Design V84-A9, pg 847-855.

Bachu S., 2000. "Sequestration of CO2 in geological media: Criteria and approach for site selection in response to climate change," Energy Conversion and Management V41, No 9, pg 953-970.

Bardet J., 1997, "Experimental Soil Mechanics," Pretince Hall, Inc.

Berg R. R., 1975, "Capilllary Pressures in Stratigraphic Traps," The American Association of Petroleum geologists Bulletin V59, No 6, pg 939-956.

Boongird P., Dunn-Norman S., Al-Bazzaz W., and Wronkiewicz D., 2006, "Formation Characterization of the Lamotte Sandstone in Soutwestern Missouri.," Final report to City Utilities, Springfield, Missouri (Unpublished).

Bradshaw B.E., Allinson G., Nguyen V., Rigg A.J., Spencer L., Wilson P., 2003, "Australia's CO_2 geological storage potential and matching of emission sources to potential sinks," Proceedings of the 6^{th} international Conference on Greenhouse Gas control Technologies, Oxford, U.K, Elsvier pg 633-638.

Carroll J. J. and Mather A. E., 1992, "The System Carbon Dioxide-Water and the Krichevsky-Kasarnovsky Equation," Journal of Solution Chemistry, V 21, pg. 607-621.

Chang C., Zoback M.D., and Khaksar A., 2006, "Empirical relations between rock strength and physical properties in sedimentary rocks," Journal of Petroleum Science and Engineering V51, pg 223-237.

Derakhshanfar M., Nasehi M., Ahmadi F., Baimyrza Z., Sherk G., 2011, "Potential sinks for geological storage of CO_2 in Saskatchewan," SPE, Canadian Unconventional Resources Conference, Alberta, Canada, 15-17 November.

Eiken O., Ringrose P., Hermanrud C., Nazarian B., Torp A.T., Hoier L., 2011, "Lessons learnt from 14 years of CCS Operations: Sleipner, In Salah and Snohvit," Energy Procedia, V4, pg 5541-5548.

Ennis-King J. and Paterson L., 2002 "Engineering aspects of geological sequestration of CO_2," SPE, presented at SPE Asia Pacific Oil and Gas Conference and Exhibition, , Melbourne, Australia, 8-10 October.

Espie A.A., 2005, "CO_2 Capture and Storage: Contributing to Sustainable World Growth," International Petroleum Technology Conference, Doha, Qatar, 21-23 November.

Fjaer E, Holt R. M., Horsrud P., Raaen A. M., Risnes R., 2008, "Petroleum Related Rock Mechanics," Elsevier Publishing.

Flannery S.O., McCarty S.C., Steptoe & Johnson, 2008, "Recent Legal Developments in Carbon Sequestration," SPE, Eastern Regional/AAPG Eastern Section Joint Meeting, Pittsburgh, Pennsylvania, USA, 11-15 October.

Folger P., 2009, "Carbon Capture and Sequestration," Congressional Research Service, Pg 1-27.

Gale J., 2004, "Geological Storage of CO_2: What do we know, where are the gaps and what more needs to be done?," Energy 29,Elsevier Ltd, Pg 1329-1338.

Gunter W.D., Bachu S., Palombi D., Lakeman B., Sawchuck B., Bonner D., 2009, "Heartland Area Redwater reef saline aquifer CO_2 storage project," Energy Procedia 1, pg 3943-3950.

Hawkes C.D., Bachu S., McLellan P.J., Zimmer U., 2004, "Geomechanical Factors Affecting Geological Storage of CO_2 in Deleted Oil & Gas Reservoirs," Petroleum Society's 5^{th} Canadian International Petroleum Conference, Calgary, Canada, 8-10 June.

Hoek E., Carranza-Torres C., and Corkum B., 2002, "Hoek-Brown failure criterion-2002 edition," Proceedings of the fifth North American rock mechanics symposium, V1, pg 267-273.

Hoek E., Marinos P., 2007, "A brief history of the development of the Hoek Brown Failure Criterion," Soils & Rocks, Associacao Brasileira de Mecanica dos Solos, V30, No 2, pg 85-92.

Holt T., Jensen J.L., and Lindeberg, 1995, "Underground Storage of CO_2 in Aquifers and Reservoirs," Energy Conversion and Management,Elsevier Ltd, V36,pg 535-538.

International Energy Agency, 2008, "World Energy Outlook 2008," Pg 80, © *OECD/IEA.*

International Energy Agency, 2009, "IEA Scoreboard 2009 35 Key Energy Trends Over 35 Years," Pg 103, © OECD/IEA.

IPCC, 2007, "Climate Change 2007: Mitigation. Contribution of Working Group III to the Fourth Assessment Report of the Intergovernmental Panel on Climate Change," Cambridge University Press, Cambridge, United Kingdom and New York, NY, USA.

ISRM, 1972, "Suggested Methods for Determining Uniaxial Compressive Strength on Rock Materials and Point Load Strength Index," ISRM Commission on Standardization of Laboratory and Field Tests, Document no 1.

ISRM, 1977, "Suggested Methods for Determining Tensile Strength of Rock Materials," ISRM Commission on Standardization of Laboratory and Field Tests, Document no 8.

Jaeger J.C., Cook N.G.W., Zimmerman R.W., 2008, "Fundamentals of Rock Mechanics Fourth Edition," Blackwell Publishing.

Juanes R., Spiteri E.J., Orr F.M.Jr., and Blunt M.J., 2006, "Impact of relative permeability hysteresis on geological CO_2 storage," Water Resources Research V 42 ,W12418.

Kaldi J. G. and Gibson-Poole C. M., 2008, "Storage Capacity Estimation, Site Selection and Characterization for CO_2 Storage Projects". CO2CRC Report No RPT08-100.

Khan S., Han H., Ansari S., Khosravi N., 2010, "An integrated Geomechanics Workflow for Cap rock-Integrity Analysis of a Potential Carbon Storage" SPE, International Conference New Orleans, Louisiana, USA, 10-12 November.

Lide D. R., 1990-1991, CRC Handbook of Chemistry and Physics, 71 ed. Boca Raton, Ann Arbor, Boston, CRC Press.

Litynski J., Plasynski S., Spangler L., Finley R., Steadman E., Ball D., Nemeth K.J., McPherson B., Myer L., 2009, "U.S. Department of Energy's Regional Carbon Sequestration Partnership Program: Overview" Energy Procedia I, Elsevier ltd, pg 3959-3967.

Lyle J.R., 1977, "Petrography and Carbonate Diagenesis of the Bonneterre Formation in the Viburnum Trend Area," Economic Geology, V72, pg420-434.

Mathieson A., Midgely J., Wright I., Saoula N., Ringrose P., 2011, " In Salah CO_2 storage JIP: CO_2 Sequestration Monitoring and verification technologies applied at Krechba, Algiers," Energy Procedia, V4, pg 3596-3603.

Michael K., Allison G., Golab A., Sharma S., Shulakova V., 2010, "Geological Storage of CO_2 in saline aquifers – A review of the experience from existing storage operations," International Journal of Greenhouse Gas Control V4, pg 659-667.

Mockovciakova A., Pandula B., 2003, "Study of the Relation between the static and dynamic modulii of rocks," Metalurgjia 42, V1, pg 37-39.

Mohammed S.A., Smart G.D.B., Somerville .J.Mc., Hammilton .S., Nassir. A.N., 2009, " Predicting rock mechanical properties of carbonates from wireline logs (A case study: Arab-D reservoir, Ghawar field, Saudi Arabia)," Marine and Petroleum Geology 26, Elsevier Publications, pg 430-444.

Nott A.J., 2009, "Tensile strength and failure criterion of analog lithophysal rock," UNLVTheses/Dissertations/ProfessionalPapers/Capstones.Paper 116,http://digitalcommons.library.unlv.edu/thesesdissertations/116

Nygaard R., 2010, "Geomechanical Analysis," Energy & Enviornmental Systems Group, Institute for Sustainable Energy, Environment AND Economy (ISEEE) report.

Petrusak R., Riestenberg D., Goad P., Schepers K., Pashin J., Esposito R., Trautz R., 2009, "World Class CO_2 Sequestration Potential in Saline Formations, Oil and

Gas Fields, Coal and Shale: The US Southeast Regional Carbon Sequestration Partnership Has It All," SPE, International Conference on CO_2 capture, Storage and Utilization, California, USA, 2-4 November.

Prtc, 2011, "Response to a soil gas study performed by Petro-Find Geochem ltd," IEAGHG Weyburn-Midale CO_2 monitoring & storage project.

Ripepi S.N., 2009 " Carbon Dioxide Storage in Coal Seams with Enhanced Coal bed Methane Recovery: Geologic Evaluation, Capacity Assessment and Field Validation of the Central Appalachian Basin," Phd. Thesis, Virginia Polytechnic Institute & State University, Blacksburg, Virginia.

Seevam P.N., Race J.M., Downie M.J., Hopkins P., 2008, "Transporting the next generation of CO_2 for carbon capture and storage: The impact of impurities on supercritical properties," 7th International Pipeline Conference, Calgary, Alberta ,Canada, 29 September-3 October.

Solomon S., Plattner G-K., Knutti R., Friedlingstein P., 2009, "Irreversible climate change due to carbon dioxide emissions," PNAS, V106, No 6, pg 1704-1709.

Steeneveldt R., Berger B., Torp T.A., 2006, "CO_2 Capture & Storage Closing the Knowing-Doing Gap," Trans IChemE, Part A, Chemical Engineering Research and Design, V84 - A9, pg 739 -763.

Szwedzicki T., 2007, "A hypothesis on Modes of Failure of Rock Samples Tested in Uniaxial Compression," Rock Mechanics and Rock Engineering, Springer Wien ,NY,USA, V40, pp 97-104.

Terzaghi.K, 1943, "Theoretical Soil Mechanics," 2nd Ed, John Wiley & Sons Inc, New York.

Tiamiyu O.M., Nygaard R., Bai.B, 2010, "Effect of Aquifer Anisotropy, Brine Withdrawal, and Well Completion Strategy on CO_2 Injectivity in Shallow Saline Aquifer," SPE, International Conference on CO_2 Capture, Storage and Utilization, New Orleans 10-12 November.

USDOE , 2010, Energy Information Administration, "International Energy Outlook,"United States Department of Energy. Website:http://fossil.energy.gov/sequestration/partnerships/index.html

United Nations Framework Convention on Climate Change
http://unfccc.int/kyoto_protocol/items/2830.php

USDOE, 2012, http://www.netl.doe.gov/technologies/carbon_seq/overview.html

Van der Pluijm & Marshak 2011, "Earth Structure: An introduction to structural geology and tectonics," W.W. Norton & Company.Inc, NY, USA.

Vorholz J., Harismiadis V.I., Rumpf B., Panagiotopoulos, 2000 "Vapor Liquid Equilibria of water carbon dioxide and binary system of water and carbon dioxide from molecular simulation" Fluid Phase Equilibria, Elsevier Ltd.

Wiprut D., Zoback M.D., 2000, "Fault Reactivation, leakage potential and hydrocarbon column heights in the Northern North Sea," Norwegian Petroleum Society Conference on hydrocarbon seals quantification, Oslo, 16-18 October.

DECC, www.decc.gov.uk, Department of Energy and Climate Change, Government of the United Kingdoms, 2012.

Zoback M.D., 2007, "Reservoir Geomechanics," Cambridge University Press.

VITA

Sudarshan Govindarajan earned his Bachelor's degree in Chemical Engineering from Mumbai University, India in the spring of 2009 and enrolled in the Master's program in Petroleum Engineering at Missouri University of Science & Technology in the fall of 2009. He earned his Master's Degree in Petroleum Engineering in August 2012.